A study of B^0–$\bar{B}^0$ mixing using the ARGUS detector

Ekaterini Tzamariudaki

A Thesis submitted to the Faculty
of Graduate Studies and Research
in partial fulfillment of the requirements
for the Degree of Doctor of Philosophy

Physics Department
McGill University, Montreal

ISBN 0-612-05805-0

Abstract

Using the ARGUS detector at the e^+e^- storage ring DORIS II at DESY, a study of the decay $\bar{B}^0 \rightarrow D^{*+}\ell^-\bar{\nu}$ has been performed by exploiting a partial D^{*+} reconstruction technique. The branching ratio was determined to be $(4.4 \pm 0.3 \pm 0.3)\%$ for this mode, and for the higher excited $D^*_{(J)}$ states $Br(\bar{B}^0 \rightarrow D^{*+}_{(J)}\ \ell^-\bar{\nu}) = (2.5 \pm 0.6 \pm 0.5)\%$. Furthermore, the inclusive D^{*+} branching ratio in B decays was measured by fully reconstructing D^{*+} candidates.

Using a tagged subset of this sample of B^0 meson decays in the mode $\bar{B}^0 \rightarrow D^{*+}\ell^-\bar{\nu}$, $B^0_d \longleftrightarrow \bar{B}^0_d$ oscillations have been studied. For this purpose two tagging techiques have been applied: the standard method of using fast leptons, and a new technique which makes use of kaons to tag the b flavour content. Combining the values obtained by these two methods, the $B^0\bar{B}^0$ mixing parameter χ_d, used to denote the strength of the oscillations, was determined to be $\chi_d = 0.165 \pm 0.057$.

In addition, using fully reconstructed D^{*+} candidates, a third study of the $B^0\bar{B}^0$ mixing parameter was carried out by investigating $D^{*+}K^{\pm}$ correlations. The mixing measurements obtained using kaons to tag the B meson flavour employ this technique for the first time. Future CP violation measurements at B Factories will place critical reliance on this method.

Finally, using the extracted value for the mixing parameter χ_d, the CKM matrix element V_{td} was determined and the $B^0_s\bar{B}^0_s$ mixing parameter χ_s was obtained.

Résumé

En utilisant le détecteur ARGUS, installé sur l' anneau de collisions DORIS II à DESY, on a étudié la désintégration $\bar{B}^0 \to D^{*+}\ell^-\bar{\nu}$ en exploitant une technique de reconstruction partielle du D^{*+} . On a mesuré le rapport de branchement de ce mode de désintégration,$(4.4 \pm 0.3 \pm 0.3)\%$, et de l' état excité $D^*_{(J)}$, $Br(\bar{B}^0 \to D^{*+}_{(J)}\ \ell^-\bar{\nu}) = (2.5 \pm 0.6 \pm 0.5)\%$. De plus, le rapport de branchement inclusif du D^{*+} en B a été mesuré en reconstruisant intégralement les candidats D^{*+} .

En utilisant un sous-ensemble identifié de l' échantillon de désintégrations du B^0 dans le mode $\bar{B}^0 \to D^{*+}\ell^-\bar{\nu}$ une étude des oscillations $B^0_d \longleftrightarrow \bar{B}^0_d$ a été menée. Pour ceci, deux techniques d' indentifications ont été appliquées, la méthode standard utilisant les leptons rapides et une nouvelle technique qui utilise les kaons pour identifier le quark b. En combinant les valeurs obtenues par les deux méthodes, le paramètre de mélange, χ_d, du système $B^0\bar{B}^0$ qui mesure l' amplitude des oscillations a été déterminé à $\chi_d = 0.165 \pm 0.057$.

De plus, en utilisant les candidats D^{*+} entièrement reconstruits, une troisième étude du paramètre de mélange du système $B^0\bar{B}^0$ a été menée en étudiant les corrélations $D^{*+}K^{\pm}$. Les mesures de mélange obtenues en identifiant le méson B, utilisent cette technique avec des kaons pour la première fois. Les mesures futures de violation de CP aux usines à B seront essentiellement basées sur cette méthode.

Finallement, en utilisant la valeur mesurée pour le paramètre de mélange χ_d, l' élément V_{td} de la matrice CKM a été déterminé ainsi que le paramètre de mélange χ_s du système $B^0_s\bar{B}^0_s$.

Acknowledgments

I would like to thank all the past and present members of the ARGUS Collaboration. Through their combined efforts and cooperation they have made the ARGUS experiment a successful one.

It has been a pleasure to work with my fellow graduate students Richard, Pat, Roland, Klaus, Thomas, Thorsten, Andreas, as well as with the ITEP colleagues. Special thanks to Klaus Reim for many useful discussions, to Roland Hofmann for various tips at the UNIX and to Pat Saull for attempting to correct my English.

My supervisor during this work was Prof. D.B.Macfarlane, who I thank for his support and encouragement.
I am particularly grateful to Dr. H.Schöder for his invaluable input and for numerous fruitful discussions. I also owe a great deal to Y.Tsipolitis who has encouraged and advised me. Thanks also go to H.Kapitza for his advice when I was working on the μVDC software. Many thanks are also due to Prof. P.M.Patel. I would also like to express my gratitude to the Department for providing me with fee waivers and the Carl Reinhardt Fellowships.

I also owe thanks to Nora van Looveran, the ARGUS secretary, for her valuable assistance on several occasions.

Finally, I say a very special thank you to my parents and my sister who, together with Yorgos, have been an inexhaustable source of support over the years and who along with my friends have made life so very enjoyable.

Contents

List of Figures

List of Tables

Chapter 1

Theoretical Background

1.1 Brief description of the Standard Model

The goal of particle physics research is the formulation of a fundamental theory which is able to describe all phenomena in nature. An important model which has so far been spectacularly successful is the so called Standard Model, which is a gauge theory that describes strong, weak and electromagnetic interactions. The model is based on a SU(3) group of colour, a SU(2) group of weak isospin and a U(1) group of weak hypercharge. Its two sub-theories are the *Theory of Electroweak Interactions* which provides a consistent description of weak and electromagnetic interactions and the *Theory of Quantum Chromodynamics* (often referred to as QCD) which describes the strong interactions. It is a common belief, however, that the Standard Model cannot be the "ultimate" theory of nature since the model has too many free parameters and leaves questions like the equality of the proton and electron electromagnetic charge, the quark and lepton families etc., unanswered. The following description of electroweak interactions aims to serve as a theoretical introduction and to provide a necessary basis for further description of the theory related to the work presented here.

1.1.1 Electroweak interactions

The theory of electroweak interactions [1] is based on a SU(2) group of weak isospin (T) and a U(1) group of weak hypercharge (Y). Quarks and leptons can be combined into SU(2) multiplets as shown in Table 1.1. Left handed fermions form SU(2) doublets ($T = 1/2$), while right handed fermions form SU(2) singlets ($T = 0$). The subscript "L" indicates that the weak isospin current couples only to left handed fermions. Also, only left handed neutrinos are required.

The electric charge Q (in units of e, where e is the charge of the electron) of the T^3 member of a weak isomultiplet (where T^3 is the third component of the weak isospin) is given by a generalization of the Gell-Mann - Nishijima relation

$$Q = T^3 + \frac{Y}{2}.$$

Quarks and leptons interact with each other by "exchanging" particles called gauge bosons. Quarks cannot be found free in nature but only in bound states which are called hadrons. Indeed, the known hadrons are confined to either $q\bar{q}$ (mesons) or qqq states (baryons). Quarks exist in three "colours" and interact with each others by exchanging gauge bosons which are called *gluons*. These interactions are described by QCD. In the standard model the quark and lepton masses are generated via the Higgs mechanism by introducing a complex doublet of scalar fields. This mechanism produces a massive scalar particle called the Higgs boson. The basic electroweak interaction

$$-ig(J^i)^\mu W^i_\mu - i\frac{g'}{2}(j^Y)^\mu B_\mu$$

consists of an isotriplet of vector fields W^i_μ coupled with strength g to the weak isospin current J^i_μ, together with a single vector field B_μ coupled with strength $g'/2$ to the weak hypercharge current j^Y_μ. Linear combinations of these fields W^i_μ and B_μ constitute the physical bosons mediating the weak interactions. Hence, the massive charged bosons which are usually called W^+ and W^-, are identified as:

$$W^\pm_\mu = \sqrt{\frac{1}{2}}\ (W^1_\mu \mp W^2_\mu) \tag{1.1}$$

	T	T^3	Y	Q
Leptons				
$\begin{pmatrix} \nu_e \\ e \end{pmatrix}_L$ $\begin{pmatrix} \nu_\mu \\ \mu \end{pmatrix}_L$ $\begin{pmatrix} \nu_\tau \\ \tau \end{pmatrix}_L$	1/2 1/2	+1/2 −1/2	−1 −1	0 −1
e_R μ_R τ_R	0	[illegible]	−2	−1
Quarks				
$\begin{pmatrix} u \\ d \end{pmatrix}_L$ $\begin{pmatrix} c \\ s \end{pmatrix}_L$ $\begin{pmatrix} t \\ b \end{pmatrix}_L$	1/2 1/2	+1/2 −1/2	1/3 1/3	2/3 −1/3
u_R c_R t_R	0	0	4/3	2/3
d_R s_R b_R	0	0	−2/3	−1/3

Table 1.1: The three generations of fundamental fermions.

and their exchange results in the change of the charge of the leptons or the flavour of the quarks taking part (where the flavour quantum number refers to the different types of quarks). The process is thus called a "charged (or flavour-changing) current" weak interaction. The weak charge current couples left-handed rotated quark states. The neutral bosons, usually referred to as γ (photon) and Z^0 boson, are identified as:

$$A_\mu = B_\mu \cos\theta_W + W_\mu^3 \sin\theta_W \qquad \text{(massless photon)} \tag{1.2}$$

$$Z_\mu = -B_\mu \sin\theta_W + W_\mu^3 \cos\theta_W \qquad \text{(massive)} \tag{1.3}$$

and give rise to the electromagnetic and the neutral current weak interactions, respectively. The parameter θ_W is the weak mixing angle, the value of which must be deduced from experimental measurements. No transitions (at least to lowest order) via flavour-changing neutral currents exist. This is ensured by the so called GIM mechanism [74] according to which weak interactions operate on doublets of left-handed quarks $\begin{pmatrix} u \\ d' \end{pmatrix} \begin{pmatrix} c \\ s' \end{pmatrix}$, where

$$\begin{pmatrix} d' \\ s' \end{pmatrix} = U \begin{pmatrix} d \\ s \end{pmatrix}.$$

In this relation, the weak eigenstates (primed quarks) are related to the quark mass eigenstates (unprimed quarks) by the unitary rotation matrix:

$$U = \begin{pmatrix} \cos\theta_C & \sin\theta_C \\ -\sin\theta_C & \cos\theta_C \end{pmatrix}$$

with the quark or flavour mixing described by the Cabibbo angle θ_C. The "*up*" quarks are, by convention, unmixed. To incorporate additional quark flavours, the GIM mechanism is extended and for three quark doublets the 3×3 mixing matrix

U, known as the Cabibbo-Kobayashi-Maskawa (CKM) matrix, contains three real parameters and a non-trivial phase.

$$\begin{pmatrix} d' \\ s' \\ b' \end{pmatrix} = V_{CKM} \begin{pmatrix} d \\ s \\ b \end{pmatrix} = \begin{pmatrix} V_{ud} & V_{us} & V_{ub} \\ V_{cd} & V_{cs} & V_{cb} \\ V_{td} & V_{ts} & V_{tb} \end{pmatrix} \begin{pmatrix} d \\ s \\ b \end{pmatrix}. \tag{1.4}$$

This complex phase introduces the possibility of a CP violating amplitude (C is the Charge conjugation symmetry and P is the Parity). The values of the amplitudes of the CKM matrix elements need to be extracted from experiment and they are presently constrained to lie in the range [2]:

$$V_{CKM} = \begin{pmatrix} 0.9747-0.9759 & 0.218-0.224 & 0.002-0.005 \\ 0.218-0.224 & 0.9738-0.9752 & 0.032-0.048 \\ 0.004-0.015 & 0.03-0.048 & 0.9988-0.9995 \end{pmatrix}. \tag{1.5}$$

The V_{ij} values are measured using various techniques. V_{ud} is determined from β-decay, V_{us} from the decay $K \rightarrow \pi e \nu$ and from semileptonic hyperon decays; V_{cd} is obtained from charmed particle production by neutrinos i.e. $\nu_\mu d \rightarrow \mu^- c$; V_{cs} follows from the decays $\nu_\mu s \rightarrow \mu^- c$ and $D^+ \rightarrow \bar{K}^0 e^+ \nu_e$. Finally, V_{cb} is extracted by measurements of the B meson lifetime and the width of the semileptonic $b \rightarrow c$ transition $\Gamma(b \rightarrow c\ell\nu)$ and the value for V_{ub} comes from the determination of the width of the semileptonic $b \rightarrow u$ transition $\Gamma(b \rightarrow u\ell\nu)$. The values for V_{tq} are inferred by imposing 3 generation unitarity; only indirect measurements are available, since hadrons containing the t-quark have not been studied. Information on V_{td} for example, can be extracted by studying the $B_d^0 \longleftrightarrow \bar{B}_d^0$ mixing as it is mentioned in later sections of this chapter and similarly on V_{ts} by studying the $B_s^0 \longleftrightarrow \bar{B}_s^0$ mixing.

The study of B meson decay properties provides a rich source of information on the CKM matrix elements involving the b quark. The analyses described in this thesis are directed towards a measurement of the strength of flavour oscillations in the $B^0 - \bar{B}^0$ system, precision measurements of which may be used to extract information on V_{td} as well as the top quark mass.

Many parametrizations of the CKM matrix exist. The particle data group quotes the following parametrization [2]

$$V_{CKM} = \begin{pmatrix} c_{12}c_{13} & s_{12}c_{13} & s_{13}e^{-i\delta_{13}} \\ -s_{12}c_{23} - c_{12}s_{23}s_{13}e^{i\delta_{13}} & c_{12}c_{23} - s_{12}s_{23}s_{13}e^{i\delta_{13}} & s_{23}c_{13} \\ s_{12}s_{23} - c_{12}c_{23}s_{13}e^{i\delta_{13}} & -c_{12}s_{23}s_{13}e^{i\delta_{13}} & c_{23}c_{13} \end{pmatrix} \tag{1.6}$$

where $c_{ij} \equiv cos\theta_{ij}$ and $s_{ij} \equiv sin\theta_{ij}$ with $i, j = 1$ to 3 for three generations are the three rotation angles and δ is the complex phase.

The so called Wolfenstein [3] parametrization arises from the empirical observation that the mixing angles have a hierarchical structure. Expanding in powers of $\lambda = sin\theta_C = 0.22$, this formulation of the CKM matrix is of the form:

$$V_{CKM} = \begin{pmatrix} 1-\frac{1}{2}\lambda^2 & \lambda & A\lambda^3(\rho - i\eta) \\ -\lambda & 1-\frac{1}{2}\lambda^2 & A\lambda^2 \\ A\lambda^3(1-\rho-i\eta) & -A\lambda^2 & 1 \end{pmatrix} \tag{1.7}$$

plus corrections of order λ^4. From experiment, the values extracted for A, ρ, η are [4, 70]

$$A = 0.9 \pm 0.1 \qquad (\rho^2 + \eta^2)^{1/2} = 0.36 \pm 0.14$$

The CKM matrix contains 4 of the Standard Model parameters which must be determined experimentally. In its present form, assuming that neutrinos are massless, there are a total of 19 free parameters not predicted by theory. These are:

- The six quark and the three lepton masses

- The strengths of the coupling constants α, α_s and G_F for the interactions between quarks or/and leptons.
- The three real and one complex parameters of the CKM matrix
- The weak mixing angle $\sin^2\theta_W$ and θ_{QCD}
- The mass of the Higgs boson.

1.2 The Υ System

Since the measurements presented in this thesis are performed at the energy of the $\Upsilon(4S)$ resonance, the Υ system is here described in more detail. The existence of the b quark was experimentally established by the discovery of the Υ resonances in 1977 at Fermilab [5] as an enhancement near 9.5 GeV/c^2 in the invariant mass spectrum of $\mu^+\mu^-$ pairs produced in 400 GeV proton-nucleus collisions. A structure consisting of two peaks was observed, one at 9.4 GeV/c^2 and one at 10.0 GeV/c^2, which were identified as the Υ and Υ' mesons. The measured widths of the peaks were consistent with experimental resolution, possibly indicating very narrow natural widths. This fact, together with the observed spacing between the two resonances which was found in the charmonium system, led to the interpretation of the Υ states as bound $q\bar{q}$ states of a new heavy quark: the b quark. One year later, the DASP II and PLUTO experiments, both carried out at the DORIS II storage ring at DESY, observed two narrow resonances at 9.46 and 10.023 GeV/c^2 (Fig. 1.1) [6] in e^+e^- collisions.

Since the Υ mesons couple to the virtual photon created in e^+e^- annihilation, they must have the quantum numbers of the photon, $J^{PC} = 1^{--}$. The Υ and Υ' were identified as the lowest lying $b\bar{b}\ {}^3S_1$ states $\Upsilon(1S)$ and its first radial excitation $\Upsilon(2S)$. Later the $\Upsilon(3S)$ was observed [8]. The narrow widths for the 1S, 2S, and 3S states are due to the dominant decay of the Υ via annihilation of the $b\bar{b}$ into three gluons as shown in Figure 1.2. Such a diagram is the only possible strong decay for Υ states below the mass threshold for the creation of two B mesons, which are the a)

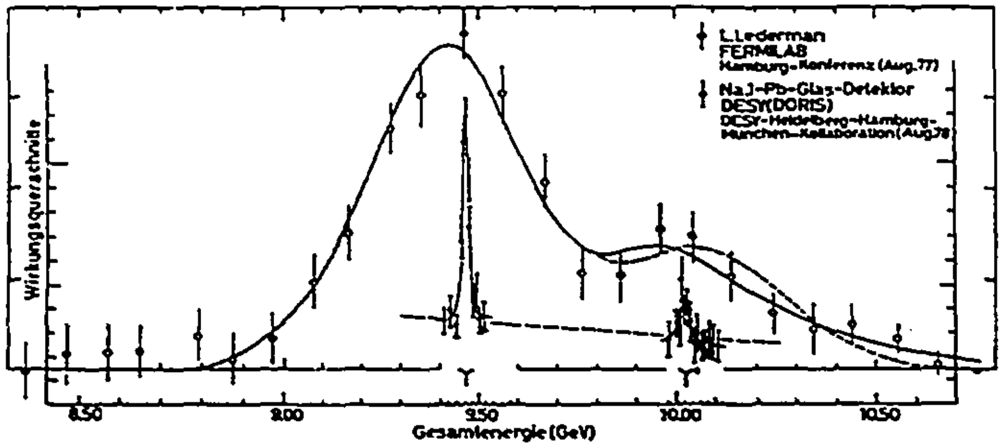

b)

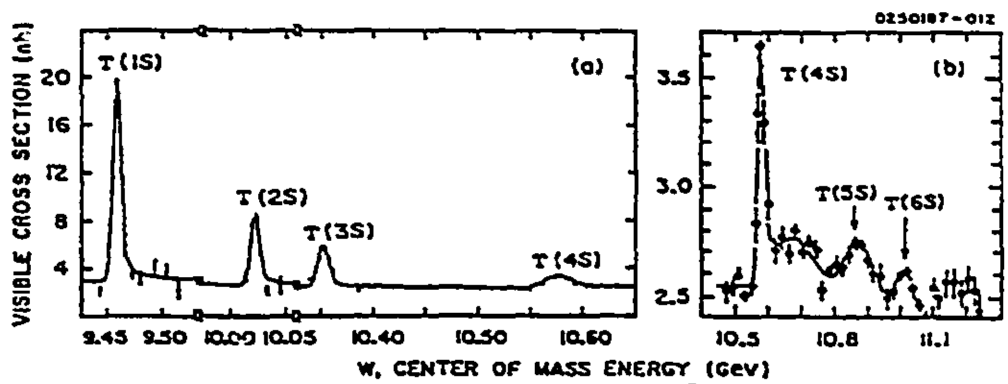

Figure 1.1: a) The Υ and Υ′ resonances from the Lederman experiment (open circles) [5] and from DORIS II experiments (full circles) [6]. b) Cross section of $e^+e^- \to$ hadrons [7].

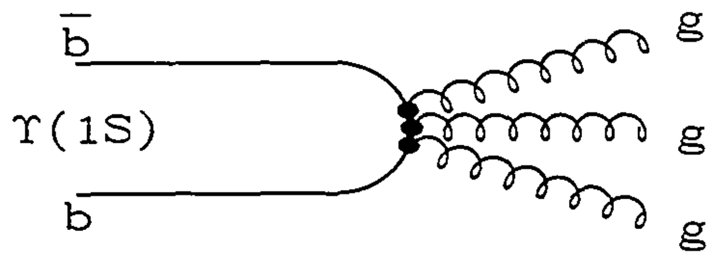

Figure 1.2: $\Upsilon(1S)$ decay to three gluons.

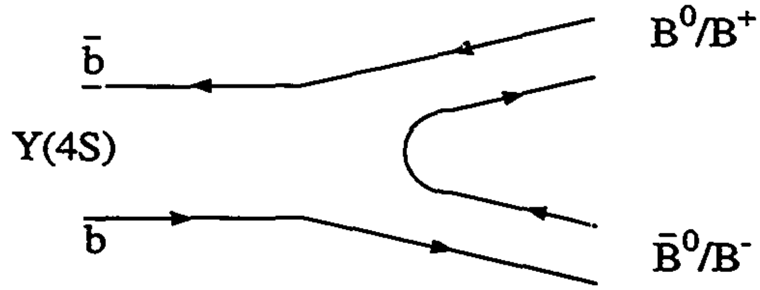

Figure 1.3: $\Upsilon(4S)$ decay to a pair of B mesons.

lightest hadrons containing a b quark. The widths of the Υ resonances above the $\Upsilon(3S)$ are several orders of magnitude larger, implying that these states lie above this threshold and therefore decay predominantly into pairs of B mesons by the OZI-favored channel as shown in Figure 1.3.

1.3 B Mesons

B mesons are bound states of the heavy $\bar{b}$ quark and a lighter u, d, s or c quark. The $\Upsilon(4S)$ is an excellent source of the b-flavoured B_d^0 and B_u^+ mesons and their antiparticles:

$$\Upsilon(4S) \longrightarrow B^0\bar{B}^0$$
$$\Upsilon(4S) \longrightarrow B^+B^-.$$

The B^0 and B^+ are the lightest mesons carrying the *bottom* or *beauty* quantum number. A study of the momentum spectrum of charged particles from $\Upsilon(4S)$ supports the assumption that the $\Upsilon(4S)$ meson decays practically 100% into B meson pairs [9]. Recently, observations of J/Ψ mesons arising from $\Upsilon(4S)$ decays have been reported with momentum beyond that allowed for a B decay product [10], [11]. This claim has given rise to extensive searches for non-$B\bar{B}$ decay mechanisms on the $\Upsilon(4S)$. In the subsequent studies, an upper limit of 0.14 (95% confidence level) on the overall fraction of non-$B\bar{B}$ decays of the $\Upsilon(4S)$ was set [12] by comparing lepton and dilepton production in $\Upsilon(4S)$ decays. Moreover, following an analysis of the large accumulated CLEO continuum data sample it was concluded that continuum production can adequately explain the high momentum J/Ψ's observed on the $\Upsilon(4S)$ [13]. Therefore, direct $\Upsilon(4S)$ decays into non $B\bar{B}$ states, if they exist, should constitute only a small fraction of $\Upsilon(4S)$ decays. Measurements of the B meson mass from fully reconstructed B mesons show that the $\Upsilon(4S)$ mass lies just above the threshold for $B\bar{B}$ pair production, which implies that B mesons are produced nearly at rest. The production ratio of B^+B^- and $B^0\bar{B}^0$ pairs in $\Upsilon(4S)$ decays $f = \frac{f_{+-}}{f_{00}} = \frac{N(B^+B^-)}{N(B^0\bar{B}^0)}$ strongly depends on the mass difference of the two types of B mesons [1] $\Delta m = m_{B^0} - m_{B^-}$. If the masses were equal, isospin symmetry implies that the production rates would also be equal. The mass difference is obtained by reconstructing the B mesons and has been found to be [14], [15]:

$$\Delta m = m_{B^0} - m_{B^-} = \begin{cases} -1.3 \pm 1.2\ MeV/c^2 & \text{ARGUS} \\ +0.4 \pm 0.6\ MeV/c^2 & \text{CLEO} \end{cases} \tag{1.8}$$

In the forthcoming analysis, the production ratio f is assumed to be 1, since the

[1]Throughout this work whenever reference to a specific charge state is made, the charge conjugate state is also implied, unless mentioned otherwise.

mass difference Δm is small enough not to cause any significant deviations from unity.

The b quark decays through the flavour-changing weak interaction. The dominant features of $B(\bar{b}q)$ meson decay are expected to be described by the spectator model, where the heavy $\bar{b}$ quark decays into a lighter $\bar{c}$ or $\bar{u}$ quark, while the lighter quark q acts as a spectator not influencing the decay rate (Fig. 1.4 a,b).

In the spectator model, the semileptonic decay of the B meson proceeds through the decay of the $\bar{b}$ quark to a $\bar{c}$ or a $\bar{u}$ quark with the emission of a virtual W^+ boson which then couples to the $\bar{l}\nu_l$ system. The semileptonic width Γ_{sl} can be written as

$$\Gamma_{sl} = \frac{G_F^2 m_b^5}{192\pi^3} \cdot \sum_{q=u,c} f_{sl}(b \to q) \cdot |V_{qb}|^2 \cdot I(\frac{m_q}{m_b}, \frac{m_l}{m_b}, 0) \tag{1.9}$$

and the hadronic width Γ_{hadr}

$$\Gamma_{hadr} = \frac{G_F^2 m_b^5}{192\pi^3} \cdot f_{hadr} \cdot \sum_{\substack{q_1, q_2 = u,c \\ q_3 = d,s}} |V_{q_1 b}|^2 |V_{q_2 q_3}|^2 \cdot I(\frac{m_{q_1}^2}{m_b^2}, \frac{m_{q_2}^2}{m_b^2}, \frac{m_{q_3}^2}{m_b^2}), \tag{1.10}$$

where the function $I(x, y, z)$ describes the phase space corrections due to finite quark and lepton masses. The factor $f_{sl}(b \to q)$ is equal to 1 and f_{hadr} is equal to the colour factor 3, if the presence of gluons is ignored. Taking corrections for radiative and hard-gluon effects into account, these factors deviate slightly from the values mentioned above, enhancing the hadronic mode [16].

If the spectator diagrams were the only possible decay diagrams, the lifetimes of the charged and neutral B mesons would be the same. It is clear, however, that the spectator model is a simplified picture: non-spectator effects can also take place. The widths for W-exchange (Fig. 1.4 c) and flavour annihilation (Fig. 1.4 d) are expected to be small, however, and theory predicts the contribution from "penguin" decays (Fig. 1.4 e, f) to be in the range $(1-15) \times 10^{-5}$. The experimentally observed branching ratio for $(B \to K^*(892)\ \gamma)$ [17] supports this prediction. As mentioned before, further decay channels via flavour-changing neutral current interactions are excluded by the GIM mechanism.

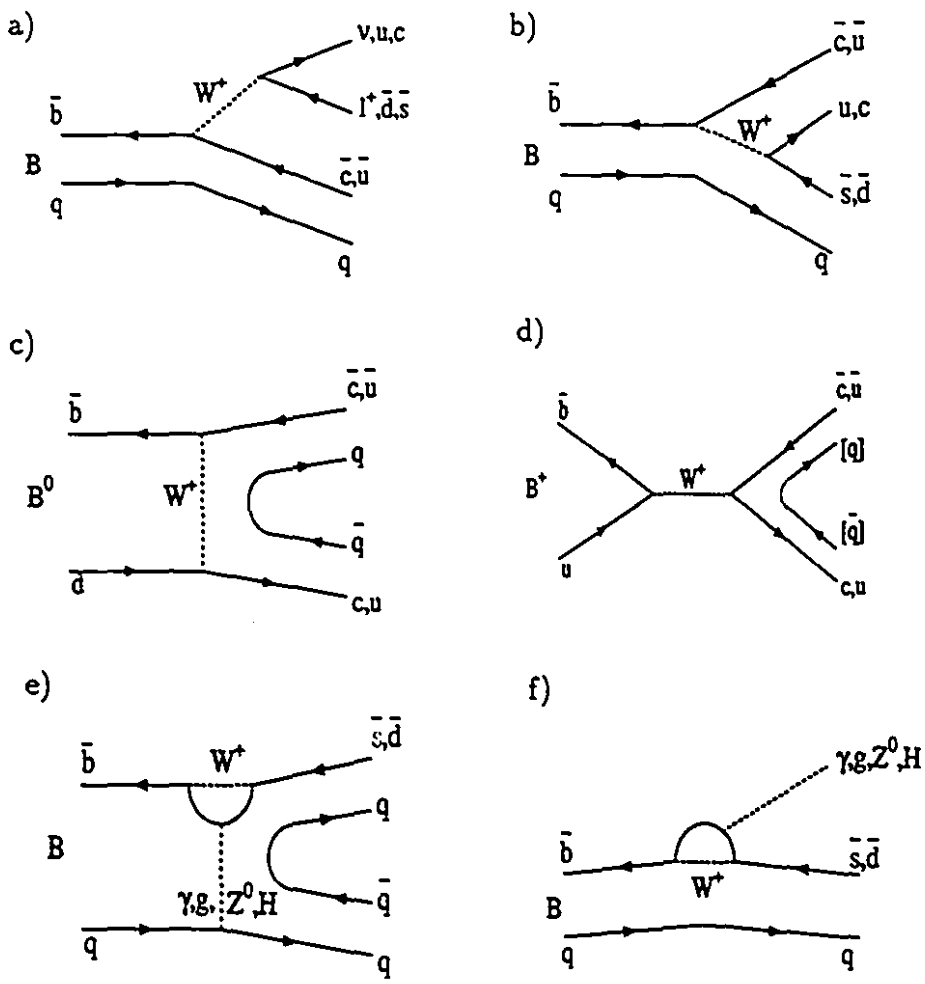

Figure 1.4: Feynman graphs of B decay mechanisms.

1.4 Semileptonic B decays

In B decays, leptons can arise from two sources. The primary source is from the virtual W in semileptonic B decays which are expected to proceed via the spectator diagram of Figure 1.4 a. The secondary source is from the decay of charmed particles ($X_c \to Y\ell^+\nu$) which are produced in the $b \to cW^-$ decay. Leptons originating from the virtual W produced in the $b \to c, uW^-$ decay can be used to *tag* the flavour content of the parent B meson. Primary leptons have positive charge when they come from B^+, B^0 mesons and negative charge when they are daughters of B^-, $\bar{B}^0$ mesons. An important source of background for lepton tagging arises from the cascade leptons which have charge of opposite sign to the charge of primary leptons. The standard approach to calculate the amplitude for the semileptonic transition is to use factorization, so that it consists of a purely hadronic and a purely leptonic part. The amplitude for the semileptonic decay of the B meson is thus given by [20]:

$$\begin{aligned} A(\bar{B} \to X_q \ + \ell\nu) &= < X_q \ell \nu_l | \bar{l}\gamma^\mu(1-\gamma_5)\nu_l \frac{G_F}{2} V_{qb}\bar{q}\gamma_\mu(1-\gamma_5)b|\bar{B} > \\ &= \frac{G_F}{2} V_{qb}\bar{u}_l\gamma^\mu(1-\gamma_5)u_\nu < X_q|\bar{q}\gamma_\mu(1-\gamma_5)b|\bar{B} > \end{aligned}$$

with the leptonic part $\bar{u}_l\gamma^\mu(1-\gamma_5)u_\nu$ being derived by exact calculations. However, this is not the case for the hadronic matrix element $< X_q|\bar{q}\gamma_\mu(1-\gamma_5)b|\bar{B} >$ which includes QCD effects. Hence, to calculate the hadronic matrix element use of a model needs to be made. There are in general two categories of models. One treats the b quark in the $b\bar{q}$ meson as quasi-free, decaying via $b \to q'\ell\nu$ with the light $\bar{q}$ quark remaining a spectator, while the other category considers only the final-state hadrons produced. The simplest model of heavy meson decay is therefore the free quark model, belonging to the first category; a modified version of this approach has been proposed by Altarelli *et* al. [18]. For models which consider only final state hadrons, the description of the hadronic part of the amplitude is made possible using all Lorentz invariant variables. Form factors are then defined as q^2-dependent functions, each multiplying one of the Lorentz invariant variables. In semileptonic B

decays of the type $P \rightarrow P\ell\bar{\nu}$ there are two Lorentz invariants; while in B decays of the type $P \rightarrow V\ell\bar{\nu}$ there are four Lorentz invariants (P and V stand for pseudoscalar and vector respectively).

1.4.1 Free-Quark model

As noted earlier, when a B-meson decays semileptonically, the decay proceeds through the spectator diagram shown in Figure 1.4 a. In analogy with muon decay, the decay width is

$$\Gamma(b \rightarrow q\ell\bar{\nu}) = \frac{G_F^2 m_b^5}{192\pi^3} \; |V_{qb}|^2 \; F(\frac{m_q^2}{m_b^2}), \tag{1.11}$$

where V_{qb} is the CKM matrix element and $F(x)$ is the three-body phase-space factor

$$F(x) = 1 - 8x + 8x^3 - x^4 - 12x^2 lnx.$$

There is a strong dependence of the decay width on the b quark mass which is only poorly known. Altarelli et al [18] proposed an improved spectator model including corrections arising from QCD effects and dealing with the bound-state effects of the b quark in the B meson, both of which affect the lepton spectrum particularly near the high momentum endpoint. In the ACCMM model [18], the B meson is represented by a pair of quarks $b\bar{q}$ with a Fermi motion attributed to the quarks in B rest frame. Then $\bar{q}$ remains a spectator and the b quark decays as a free quark $b \rightarrow q'\ell\bar{\nu}$ (where $q' = c, u$). The spectator antiquark is treated as a particle of definite mass m_{sp}, and momentum $\vec{p}$, while the heavy quark is viewed as a virtual particle of invariant mass $\mathcal{W}$

$$\mathcal{W}^2 = M_B^2 + m_{sp}^2 - 2M_B\sqrt{\vec{p}^2 + m_{sp}^2},$$

where M_B is the B meson mass. A Gaussian distribution is assumed for the spectator momentum

$$\phi(|\vec{p}|) = \frac{4}{\sqrt{\pi}p_F^3} \cdot exp(-\frac{|\vec{p}|^2}{p_F^2})$$

where the parameter for the momentum spread p_F is adjustable. The lepton spectrum is obtained in this model after folding $\phi(|\vec{p}|)$ with the decay spectrum of the heavy quark of effective mass $\mathcal{W}$.

1.4.2 Form factor models

The Wirbel-Bauer-Stech model (WBS)

The decay amplitudes are given by the product of a leptonic ($<\nu|J_\mu|\ell>$) and a hadronic $V-A$ current ($<X^{(*)}|J_\mu|B>$); where $X(J^P=0^-)$, $X^*(J^P=1^-)$ is the meson produced in an exclusive semileptonic B decay $\bar{B}\to X^{(*)}\ell^-\bar{\nu}$. In the WBS model [19], nearest pole dominance is assumed for the dependence of the form factors on q^2

$$F(q^2)=\frac{h}{1-q^2/M^2_{\rm pole}}.$$

The form factors h ($F(q^2=0)=h$) are called overlap factors since they can be expressed as the overlap of the initial and final state meson wave functions. In the case $\bar{B}\to X^*\ell^-\bar{\nu}$, there are 5 form factors, $V(q^2)$, $A_0(q^2)$, $A_i(q^2)$ with $i=1,2,3$, of which 4 are independent. The authors claim that the overlap factors h_1, h_{A_2} can be reliably calculated, while to estimate h_V and h_{A_1} an additional free parameter J_M needs to be introduced. This parameter can be fixed using experimental information. The choice of J_M has a strong influence on the $\Gamma_{SL}(\bar{B}\to X^*)$. To fix the form factors at $q^2=0$, the initial and final mesons are described as relativistic bound states of quark-antiquark pairs in the infinite momentum frame. The meson wave functions are solved in a relativistic harmonic oscillator potential using an infinite momentum frame.

The Isgur-Scora-Grinstein-Wise model (ISGW)

In the ISGW model [20] the hadronic tensor

$$h_{\mu\nu}\equiv\sum_{s_x}<\bar{B}(p_x)|j^+_\nu|X(p_x,s_x)><X(p_x,s_x)|j_\mu|\bar{B}(p_B)>$$

for the decay $\bar{B} \to Xe\bar{\nu}$ is expressed in terms of a set of Lorentz invariants multiplied with form factors. ISGW use exponential form factors. For the total lepton spectrum, these form factors are calculated for each channel X with quantum numbers 1S, 1P and 2S using a non-relativistic quark model and all contributing final states are summed: $< B|j^{\mu}(0)|X >= \sum_i f_i(q^2 - q^2_{max})X_i^{\mu}$ where X_i^{μ} are vectors constructed from the available kinematic variables, and f_i are the Lorentz-invariant form factors. In the non-relativistic limit the Lorentz-invariant form factors f_i and those appearing in the quark model calculation (called $\tilde{f}_i$) are in one-to-one correspondence. The form factors are calculated in the limit of zero recoil ($p_x^2 = 0$, where the momentum transfer is maximum). ISGW have chosen to use Schrödinger wave functions in a Coulomb plus linear potential. The formulas derived are only valid for wave functions with $\frac{<p_i^2>}{m_i^2} << 1$ (p_i and m_i are the momentum and mass of the quark i). At large p_x^2, a constant factor, κ, is introduced so that the form factors computed as functions of $(q^2 - q^2_{max})$ are replaced by the same functions of $(q^2 - q^2_{max})/\kappa^2$. Comparing to the experimentally determined $F_{\pi}(Q^2)$, the authors find $\kappa = 0.7$. For $\bar{B} \to X_c e^- \bar{\nu}$ the model predicts

$$\Gamma(\bar{B}^0 \to X_c e^- \bar{\nu}) = \Gamma(B^- \to X_c e^- \bar{\nu}) = 0.41 \times 10^{14}\ |V_{cb}|^2\ sec^{-1}.$$

1.5 Kaon production in B meson decays

The most common production mechanism for kaons in B meson decays is via the production of s quarks in the $b \to c \to s$ decay chain. The charge of the kaons which are produced in this way may be used to tag the flavour content of the parent B meson. There exist, however, secondary processes which lead to the production of kaons, namely through the virtual $W^{\pm}$ decay or through vacuum excitation of an $s\bar{s}$. An additional complication arises from non-spectator decays of the B meson.

A diagram illustrating a spectator decay of the B is shown in Fig. 1.5. The number of kaons expected per B meson is shown in Table 1.2. The numbers presented in Table 1.2 include QCD and phase space effects for the $b \to c, u$ part [21], while

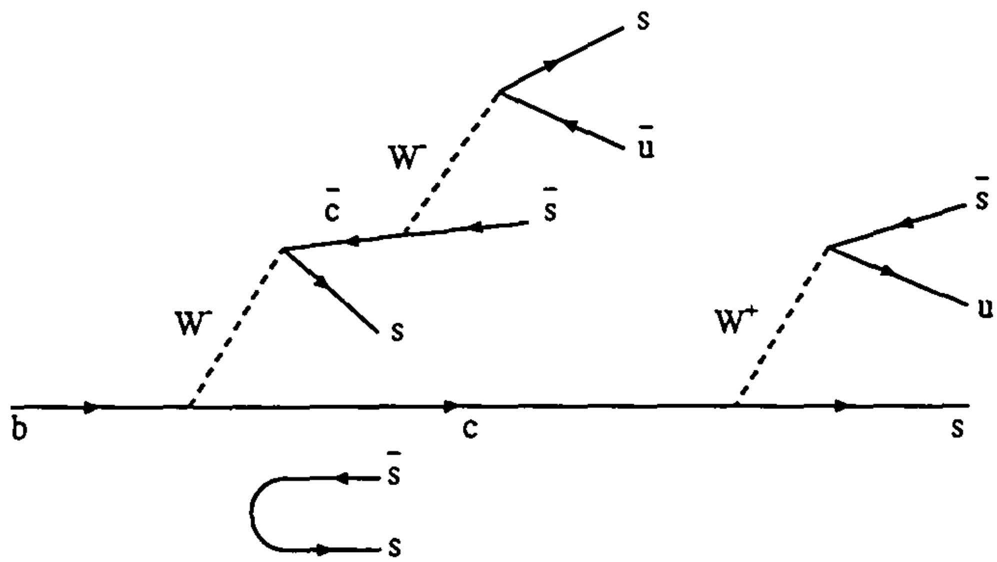

Figure 1.5: Feynman diagram showing s quark production in B decays which may lead to $K^{\pm}$ production.

the $c \to s, d$ part consists of estimates based on simple arguments. These numbers account only for spectator decays.
From Figure 1.5 one therefore obtains the $b \to s, \bar{s}$ rates shown in Table 1.3. Production of $s\bar{s}$ pairs from the vacuum, which is expected to have only a minor contribution and for which there exist large theoretical uncertainties, is not taken into account.

From experiment there exist only limits for processes that involve vacuum excitation of an $s\bar{s}$ pair. The 90% confidence level limits

$$Br(B \to D_s^+ \ell^- K^- X) < 0.8\% \tag{1.12}$$

$$Br(B \to D_s^+ \ell^- \bar{K}^0 X) < 1.2\% \tag{1.13}$$

quoted in [22] for the process shown in Fig. 1.6 b, should be compared with the $Br(B \to (D, D^*, D^*_{(J)})\ell^- \bar{\nu})$, (Fig. 1.6 c), which is $\approx (10.4 \pm 0.4)\%$ [2]. The above quoted limit allows at most $\approx 10\%$ $s\bar{s}$ production from the vacuum. The corresponding number from the Monte Carlo simulation is 12%. The resulting change

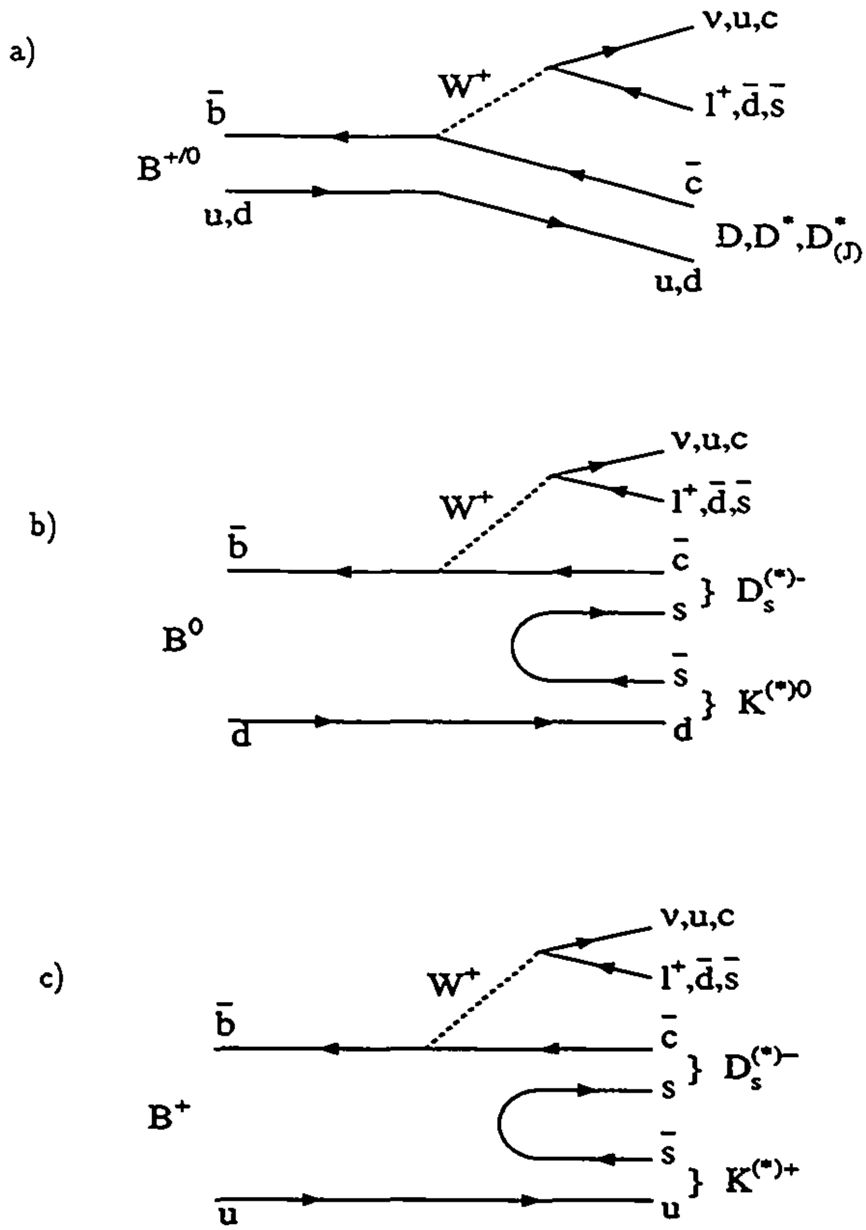

Figure 1.6: Feynman graphs for the decays a) $Br(B^{+/0} \rightarrow D, D^{*}, D^{*}_{J}\ \ell^{+}\ \nu)$, b) $Br(B \rightarrow D_s^{+}\ell^{-}K^{-}X)$ and c) $Br(B \rightarrow D_s^{+}\ell^{-}\bar{K}^{0}X)$.

Decay process	expected rate
$b \to cX$	98.0%
$b \to c(\bar{u}s)$	2.3%
$b \to c(\bar{c}s)$	20.3%
$b \to u(\bar{c}s)$	0.4%
$c \to sX$	95%
$c \to s(\bar{s}u)$	3%
$c \to s(\bar{d}u)$	53%
$c \to d(\bar{s}u)$	$< 1\%$

Table 1.2: Expected rates for various b and c quark decays leading to s quark production which in turn may lead to kaons.

Decay process	expected rate
$b \to sX$	117%
$b \to \bar{s}X$	23%

Table 1.3: Expected rates for s, $\bar{s}$ production from b decays.

in the expected rate for $b \to s, \bar{s}$ does not influence the calculation of the expected number of kaons per B meson very much and will be considered when using these numbers for later computations.

1.6 Phenomenology of the $B^0\bar{B}^0$ mixing

The two neutral bottom meson states $B^0_d(\bar{b}d)$ and $\bar{B}^0_d(b\bar{d})$ have, in the absence of weak interactions, the same mass and carry the same quantum numbers apart from the b flavour. The weak interaction gives rise to $B^0 - \bar{B}^0$ oscillations, that is transitions for which the flavour quantum number changes by two units, $\Delta B = 2$. This phenomenon of particle-antiparticle mixing can be described in the Hamiltonian framework.

The total Hamiltonian consists of two pieces: $H = \mathcal{H}_S + \mathcal{H}_{EW}$. The strong interaction Hamiltonian $\mathcal{H}_S$ is flavour conserving, while the electroweak Hamiltonian $\mathcal{H}_{EW}$ is flavour changing. Once a state is produced, say $|B^0\rangle$, under the influence of $\mathcal{H}_{EW}$ there will be transitions, (oscillations), between this state and the state with opposite beauty quantum number, thus resulting in non-exponential decay of the state $|B^0\rangle$.

The evolution of the system $B^0 - \bar{B}^0$ is dictated by the non-Hermitian Hamiltonian H.

$$H \begin{pmatrix} B^0 \\ \bar{B}^0 \end{pmatrix} = \begin{pmatrix} \mathcal{H}_{11} & \mathcal{H}_{12} \\ \mathcal{H}_{21} & \mathcal{H}_{22} \end{pmatrix} \begin{pmatrix} B^0 \\ \bar{B}^0 \end{pmatrix} \tag{1.14}$$

The existence of non-diagonal elements in the Hamiltonian is responsible for mixing. From 1.14 it follows that

$$\langle B^0|H|\bar{B}^0\rangle = \mathcal{H}_{12} \quad \text{and} \quad \langle \bar{B}^0|H|B^0\rangle = \mathcal{H}_{21}. \tag{1.15}$$

Assuming CPT invariance $\mathcal{H}_{11} = \mathcal{H}_{22} = \mathcal{H}$, which is then written as

$$\mathcal{H} = M - \frac{i}{2}\Gamma$$

with M, Γ real. Writing $\mathcal{H}_{12}$ as

$$\mathcal{H}_{12} = M_{12} - \frac{i}{2}\Gamma_{12}$$

where in general M_{12} and Γ_{12} can be complex, and requiring CPT invariance, one obtains for $\mathcal{H}_{21}$,

$$\mathcal{H}_{21} = M_{12}^* - \frac{i}{2}\Gamma_{12}^*.$$

Equation 1.14 therefore becomes

$$H \begin{pmatrix} B^0 \\ \bar{B}^0 \end{pmatrix} = \begin{pmatrix} M - \frac{i}{2}\Gamma & M_{12} - \frac{i}{2}\Gamma_{12} \\ M_{12}^* - \frac{i}{2}\Gamma_{12}^* & M - \frac{i}{2}\Gamma \end{pmatrix} \begin{pmatrix} B^0 \\ \bar{B}^0 \end{pmatrix} \tag{1.16}$$

Using certain linear combinations of the flavour eigenstates $|B^0\rangle$ and $|\bar{B}^0\rangle$ to diagonalize the matrix in 1.16, one obtains the normalized physical eigenstates for H:

$$|B^0_{1,2}\rangle = \frac{1}{\sqrt{1+|\eta|^2}} \cdot [|B^0\rangle \pm \eta|\bar{B}^0\rangle] \tag{1.17}$$

where

$$\eta \equiv \frac{1-\epsilon}{1+\epsilon} = \left(\frac{M^*_{12} - \frac{i}{2}\Gamma^*_{12}}{M_{12} - \frac{i}{2}\Gamma_{12}}\right)^{1/2} \tag{1.18}$$

In the case of CP conservation, M_{12} and Γ_{12} will also be real, giving $|\eta| = 1$ and $|B^0_{1,2}\rangle$ will have CP eigenvalues ∓ 1. The time evolution of these states is simply:

$$|B^0_{1,2}, t\rangle = e^{-\Gamma_{1,2}t/2} e^{-im_{1,2}t} |B^0_{1,2}\rangle \tag{1.19}$$

with

$$m_{1,2} = M \pm Re[\mathcal{H}_{12}\mathcal{H}_{21}]^{1/2} \quad \text{and} \quad \Gamma_{1,2} = \Gamma \mp 2Im[\mathcal{H}_{12}\mathcal{H}_{21}]^{1/2}. \tag{1.20}$$

The states $|B^0\rangle$ and $|\bar{B}^0\rangle$ produced in a strong interaction at $t = 0$ have at some later time t become:

$$\begin{aligned} |\Psi(t)\rangle_{B^0} &= f_+(t)|B^0\rangle + \eta f_-(t)|\bar{B}^0\rangle \\ |\Psi(t)\rangle_{\bar{B}^0} &= f_+(t)|\bar{B}^0\rangle + \frac{1}{\eta} f_-(t)|B^0\rangle \end{aligned} \tag{1.21}$$

respectively, with

$$f_\pm(t) = \frac{1}{2}[e^{-im_1 t} e^{-\Gamma_1 t/2} \pm e^{-im_2 t} e^{-\Gamma_2 t/2}]. \tag{1.22}$$

From 1.22 one infers that a state which at $t = 0$ was a pure $|B^0\rangle$ (or $|\bar{B}^0\rangle$), is at a later time a mixture of $|B^0\rangle$ and $|\bar{B}^0\rangle$. Hence, the probabilities of finding the various states at time t starting with $|B^0\rangle$ (or $|\bar{B}^0\rangle$) are:

$$\begin{aligned} \mathcal{P}(B^0 \to B^0; t) &= |f_+(t)|^2 & \mathcal{P}(\bar{B}^0 \to \bar{B}^0; t) &= |f_+(t)|^2 \\ \mathcal{P}(B^0 \to \bar{B}^0; t) &= |\eta|^2 |f_-(t)|^2 & \mathcal{P}(\bar{B}^0 \to B^0; t) &= \frac{1}{|\eta|^2} |f_-(t)|^2 \end{aligned} \tag{1.23}$$

with

$$|f_+(t)|^2 = \frac{1}{4}\left[e^{-\Gamma_1 t} + e^{-\Gamma_2 t} + 2e^{-\Gamma t}\cos\Delta M t\right]$$
$$|f_-(t)|^2 = \frac{1}{4}\left[e^{-\Gamma_1 t} + e^{-\Gamma_2 t} - 2e^{-\Gamma t}\cos\Delta M t\right].$$

The quantity

$$\Gamma = \frac{1}{2}(\Gamma_1 + \Gamma_2)$$

is the average width of the long and short-lived state and the oscillation frequency

$$\Delta M = m_1 - m_2$$

is the mass difference of the states. From the above equations it is clear that only if CP is conserved do the rates for $B^0 \to \bar{B}^0$ and $\bar{B}^0 \to B^0$ become equal. For this "single particle initial state" the mixing rate is expressed as the total number of $\bar{B}^0$ mesons found per B^0 produced and vice versa.

$$r \equiv \frac{\int_0^\infty \mathcal{P}(B^0 \to \bar{B}^0; t)dt}{\int_0^\infty \mathcal{P}(B^0 \to B^0; t)dt} = \frac{|\eta|^2 \frac{1}{4}\left[\frac{1}{\Gamma_1} + \frac{1}{\Gamma_2} - \frac{2\Gamma}{\Gamma^2+\Delta M^2}\right]}{\frac{1}{4}\left[\frac{1}{\Gamma_1} + \frac{1}{\Gamma_2} + \frac{2\Gamma}{\Gamma^2+\Delta M^2}\right]}$$
$$= |\eta|^2 \frac{x^2 + y^2}{2 + x^2 - y^2} \tag{1.24}$$

$$\bar{r} \equiv \frac{\int_0^\infty \mathcal{P}(\bar{B}^0 \to B^0; t)dt}{\int_0^\infty \mathcal{P}(\bar{B}^0 \to \bar{B}^0; t)dt} = \frac{1}{|\eta|^2}\,\frac{x^2 + y^2}{2 + x^2 - y^2} \tag{1.25}$$

where the definitions

$$x = \frac{\Delta M}{\Gamma} \quad \text{and} \quad y = \frac{\Delta\Gamma}{2\Gamma}$$

have been used. In the case in which CP is conserved,

$$r = \bar{r} = \frac{x^2 + y^2}{2 + x^2 - y^2} \tag{1.26}$$

If CP is not conserved, the asymmetry

$$a = \frac{r - \bar{r}}{r + \bar{r}} \approx -4Re(\epsilon)$$

can be used to measure the strength of the CP violation. For B mesons,

$$\eta_{B_d} \approx \frac{V_{td}}{V_{td}^*} = e^{2i\phi_{td}}$$

[23], where ϕ_{td} is the phase of the CKM matrix element V_{td}. Hence, also in the case of CP non-conservation, $|\eta_{B_d}| \approx 1$. From 1.20, it follows that

$$\begin{aligned} \Delta M &= 2Re\sqrt{(M_{12} - i\frac{\Gamma_{12}}{2})(M_{12}^* - i\frac{\Gamma_{12}^*}{2})} \\ \Delta\Gamma &= -4Im\sqrt{(M_{12} - i\frac{\Gamma_{12}}{2})(M_{12}^* - i\frac{\Gamma_{12}^*}{2})}. \end{aligned} \tag{1.27}$$

M_{12} and Γ_{12} can be determined from theory by evaluating a second-order weak transition matrix element known as a box-diagram (Fig. 1.7). M_{12} corresponds to virtual $B^0\bar{B}^0$ transitions, while Γ_{12} describes real transitions due to the decay modes which are common to the B^0 and the $\bar{B}^0$, such as $B^0, \bar{B}^0 \rightarrow u\bar{d}d\bar{u}, u\bar{d}d\bar{c}$ or $c\bar{d}d\bar{c}$. Of these common modes, the first two are Cabibbo suppressed, while the last is suppressed by the small phase space of the decay; they therefore represent only a very small fraction of the total B decay rate. Neglecting Γ_{12} in the $B^0\bar{B}^0$ system, the above equations for ΔM and $\Delta\Gamma$ simplify to

$$\Delta M \approx 2|M_{12}| \quad \text{and} \quad \Delta\Gamma \approx 0. \tag{1.28}$$

Hence, it is expected that $\frac{\Delta\Gamma}{\Gamma} << 1$, and one can therefore neglect y^2 in the expression for r, which then reduces to

$$r = \frac{x^2}{2 + x^2}. \tag{1.29}$$

$B^0 - \bar{B}^0$ transitions proceed via the "box diagrams" shown in Fig. 1.7.

Theoretical calculations performed by [24], [25], give the explicit formula for M_{12} for any pseudoscalar meson P composed of one heavy(h) and one light quark(l), ($P = h\bar{l}$), neglecting the internal momenta of the two quarks as well as the mass of the light quark. They find

$$\langle P^0|\mathcal{H}_{eff,V-A}^{\Delta p=2}|\bar{P}^0\rangle = M_{12} - i\frac{\Gamma_{12}}{2} =$$

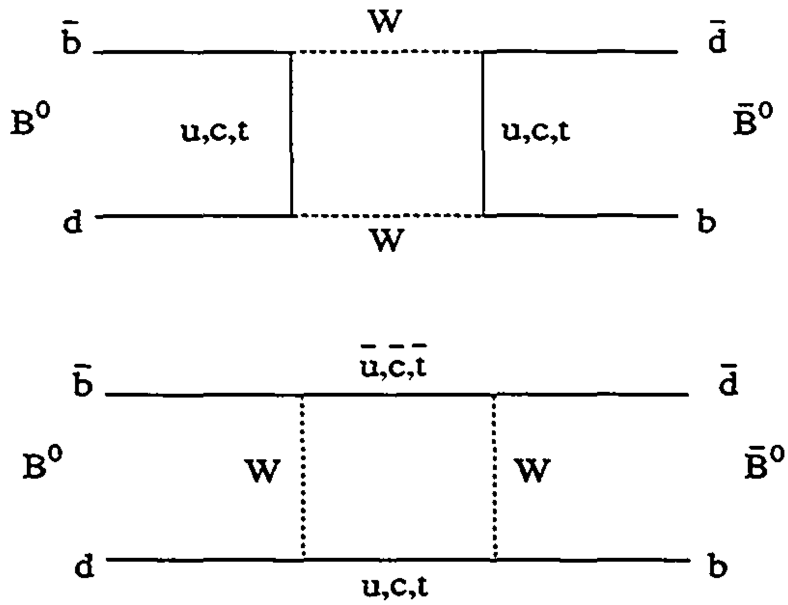

Figure 1.7: Box diagrams for $B^0\bar{B}^0$ transitions.

$$\frac{G_F^2 M_W^2}{16\pi^2}\{\langle P^0|(\bar{h}\gamma_\mu(1-\gamma_5)l)^2|\bar{P}^0\rangle \sum_{i,j}\lambda_i\lambda_j B_{ij}\}, \tag{1.30}$$

where the sum extends over i,j=u,c,t(d,s,b) for the heavy quark h of down(up) type and $\lambda_i = V_{ih}^* V_{il}$ where V_{ik} are the corresponding CKM matrix elements, and the coefficients B_{ij} are functions of the masses of the quarks involved (m_i, m_j) and the $W^\pm$ mass M_W.

From the previous equation it follows that in the case of the B_d system

$$M_{12} \;=\; \frac{G_F^2 M_W^2}{16\pi^2}\sum_{i,j}\lambda_i\,\lambda_j\,\mathcal{M}_{V-A}\,B_{ij} \tag{1.31}$$

where

$$\mathcal{M}_{V-A} = \langle B^0|(\bar{b}\gamma_\mu(1-\gamma_5)d)^2|\bar{B}^0\rangle = \frac{8}{6} f_B^2 m_b B_d. \tag{1.32}$$

For the "bag" parameter B_d, which arises from the vacuum insertion approximation, and for the B decay constant f_B, from the parametrization of the hadronic matrix element, the values $B_d = 1.0 \pm 0.2$ and $f_{B_d} = 180 \pm 50\ MeV$ will be used respectively [70]. Equation 1.31 is then written as:

$$M_{12} = \frac{G_F^2 B_d f_B^2 m_b M_W^2}{12\pi^2}[\lambda_c^2 U_1 \eta_1 + \lambda_t^2 U_2 \eta_2 + 2\lambda_t \lambda_c U_3 \eta_3] \tag{1.33}$$

where η_i are QCD corrections and U_i are functions of m_u, m_c, m_t, m_b and M_W. This expression can be simplified knowing that for a wide range of values for the top quark mass $U_2 \gg U_1, U_3$. Also, λ_t^2, λ_c^2 and $\lambda_t \lambda_c$ for the B_d meson system are comparable in magnitude (in contrast to the Kaon system). U_2 is found to be [26]

$$U_2 = \frac{m_t^2}{M_W^2} F(\frac{m_t^2}{M_W^2}). \tag{1.34}$$

Since the U_2 term is by the far the dominant contribution to eq. 1.34, $\Delta M \approx 2|M_{12}|$ can be approximated as

$$\Delta M \approx \frac{G_F^2 B_d f_B^2 m_b M_W^2}{6\pi^2} |V_{tb}^* V_{td}|^2 \frac{m_t^2}{M_W^2} F(\frac{m_t^2}{M_W^2}) \eta_{QCD} \tag{1.35}$$

where

$$F(x) = \frac{1}{4} + \frac{9}{4(1-x)} - \frac{3}{2(1-x)^2} - \frac{3x^2 ln x}{2(1-x)^3}. \tag{1.36}$$

From 1.35 it follows that for the mixing parameter x_d one obtains:

$$x_d = \frac{\Delta M}{\Gamma} \approx \frac{G_F^2}{6\pi^2}\ m_b\ \tau_B\ (B_d f_{B_d}^2)|V_{tb}^* V_{td}|^2\ m_t^2 F(\frac{m_t^2}{M_W^2})\ \eta_{QCD} \tag{1.37}$$

with τ_B being the B hadron lifetime.

Experimentally, pairs of B hadrons which are produced in e^+e^- (or $p\bar{p}$) annihilation are used to perform measurements of the mixing parameter r (or x). The flavour content of both B hadrons needs to be tagged, so that the ratio of B mesons with the same and different b quark content (*mixed* over *unmixed* B mesons) is formed. This ratio,

$$\rho = \frac{N_{BB} + N_{BB}}{N_{BB}} \tag{1.38}$$

will be used for the determination of the mixing parameter r. In the absence of mixing $\rho = 0$. In the case of the $\Upsilon(4S)$ resonance, the two b quarks hadronize into a $B_d^0\bar{B}_d^0$ pair, so one has to deal with a "correlated two-particle initial-state wave function". In general, for a $B^0\bar{B}^0$ system produced with relative angular momentum L, the quantities relevant to mixing which can be related to experimental data are [27]:

$$R_L = \frac{P(B^0B^0)_L}{P(B^0\bar{B}^0)_L} \quad \text{and} \quad \bar{R}_L = \frac{P(\bar{B}^0\bar{B}^0)_L}{P(B^0\bar{B}^0)_L} \tag{1.39}$$

In the framework of the S.M. these are given by:

$$\begin{aligned} R_L &= \frac{1}{|\eta|^2}\cdot\frac{(1+x^2)^2(1\pm y^2)-(1-y^2)^2(1\mp x^2)}{(1+x^2)^2(1\pm y^2)+(1-y^2)^2(1\mp x^2)} \\ \bar{R}_L &= |\eta|^2\cdot\frac{(1+x^2)^2(1\pm y^2)-(1-y^2)^2(1\mp x^2)}{(1+x^2)^2(1\pm y^2)+(1-y^2)^2(1\mp x^2)} \end{aligned} \tag{1.40}$$

where the upper(lower) sign should be taken for L =even(odd). The two B meson system coming from the decay of the $\Upsilon(4S)$ is in a P-wave state and its wave function should be antisymmetric. Since the $\Upsilon(4S)$ has $J = 1$ and the B mesons have spin equal to 0, the two B mesons should have a relative angular momentum $L = 1$. For $L = 1$ the expressions 1.40 become:

$$\begin{aligned} R_{L=1} &= \frac{1}{|\eta|^2}\cdot\frac{x^2+y^2}{2+x^2-y^2} = \bar{r} \\ \bar{R}_{L=1} &= |\eta|^2\cdot\frac{x^2+y^2}{2+x^2-y^2} = r \end{aligned} \tag{1.41}$$

The relation between $R_{odd}(\bar{R}_{odd})$ and $\bar{r}(r)$ arises from the fact that since the two particle wave function is antisymmetric under the exchange of the two particles, the appearance of either B^0B^0 or $\bar{B}^0\bar{B}^0$ is forbidden by Bose statistics. This implies that if one of the two particles decays at time $t = t_1$ as a B^0, then at that very moment the other particle is a pure $\bar{B}^0$. This particle for $t > t_1$ oscillates just as the one particle system and will decay at time $t = t_2(t_2 > t_1)$. Hence the probability to observe a B^0B^0 event is the probability that the $\bar{B}^0$ oscillates into B^0, which is the quantity already defined in 1.26 as $\bar{r}$. According to 1.39, 1.41, after tagging the b quark content of the two B mesons, the relation 1.38 for ρ becomes:

$$\rho = \frac{N_{B^0 B^0} + N_{\bar{B}^0 \bar{B}^0}}{N_{B^0 \bar{B}^0}}, \tag{1.42}$$

which assuming CP invariance reduces to

$$\rho = r.$$

When the B mesons are produced incoherently, e.g. via Z^0 decay or in $p\bar{p}$ annihilation, the ratio of "mixed" to "unmixed" events is given by [27]

$$R_{incoh} = \frac{2r}{1+r^2}$$

Experimentally, the way to proceed is to measure the quantity ρ given in equation 1.42, or equivalently the quantity ρ', defined as:

$$\rho' = \frac{N_{B^0 B^0} + N_{\bar{B}^0 \bar{B}^0}}{N_{B^0 \bar{B}^0} + N_{B^0 B^0} + N_{\bar{B}^0 \bar{B}^0}}, \tag{1.43}$$

which leads to the determination of the mixing parameter χ

$$\chi = \frac{1}{2}\,\frac{x^2}{1+x^2}. \tag{1.44}$$

To accomplish this, the flavour of both B^0 and $\bar{B}^0$ mesons has to be identified. For this purpose, several tagging techniques have been developed. Usually, the leptons originating from the semileptonic decays of the B mesons are employed as B flavour tags as shown in Figure 1.8.

To extract the value of ρ (or ρ'), the contribution of charged B mesons to the lepton tags has to be determined; for which a certain value of $\lambda = b_+^2 f_+ / b_0^2 f_0$ has to be used. Here, f^+ (f^0) is the branching ratio for $\Upsilon(4S)$ decaying into charged (neutral) B mesons and b_+ (b_0) the semileptonic branching ratio of charged (neutral) B mesons. Therefore, the measurement performed using dileptons depends on the value of λ used. To obtain a measurement of ρ or ρ' which is independent of λ, techniques which involve reconstruction of one of the neutral B mesons in an exclusive decay channel

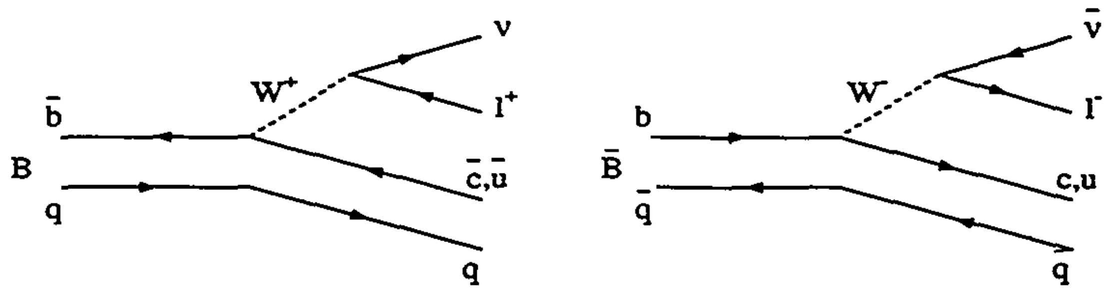

Figure 1.8: Leptons coming from the semileptonic B^0 and $\bar{B}^0$ decays used as B flavour tags.

(mostly the $\bar{B}^0 \to D^{*+}\ell^-\bar{\nu}$ decay, using the "missing mass" technique described in Section 3.1) are employed. For the other B meson the charge of a daughter particle is used as a *tag*. Other particles used as *tags* are the D^{*+} mesons coming from the hadronization of the $c\bar{q}$ pair in the $b\bar{q} \to c\bar{q}W^-$ decay. In this work, in addition to these particles, kaons originating from the $b \to c \to s$ decay will be used as B flavour tags. While exclusive reconstruction of a certain decay mode provides low statistics samples, the background is usually larger when both B mesons are tagged using the charge of the particle-tags. To achieve both low background and high statistics, partial reconstruction techniques, are invented. These involve tagging in a specific decay channel of the B meson. A detailed description of the partial reconstruction technique applied in this work, is illustrated in Section 3.1.

Chapter 2

The ARGUS Detector

2.1 DORIS II e^+e^- Storage Ring

DORIS is an acronym for "Doppel Ring Speicher" reflecting that, in its original incarnation, the storage ring actually had two separate magnetic guide fields for positrons and electrons. This facility was upgraded in energy and turned into a more conventional single ring collider starting in 1978 with the discovery of the Υ resonances. DORIS II provides counter-rotating electron and positron beams that collide at two interaction regions, one of which is the site of the ARGUS detector. The layout of the accelerator complex is shown in Figure 2.1

Electrons are supplied by a small linear accelerator, LINAC I, which accelerates them to an energy of 55 MeV. The electron beam is then injected into the DESY synchrotron. Positrons are produced by bombarding a tungsten target with electrons from a second linac, and are accumulated in a small storage ring called PIA (Positron Intensity Accumulator). When enough positrons have been accumulated, they are also transferred into the DESY synchrotron. Here, electron and positron bunches are accelerated to the requested energy, between 4.5 and 5.5 GeV, before being injected into the DORIS storage ring. In DORIS, the beams circulate in single bunches with currents of about 30 mA per beam and a crossing period at each interaction point of 1 μs. Typical run periods of the order of one hour are achieved before the beams

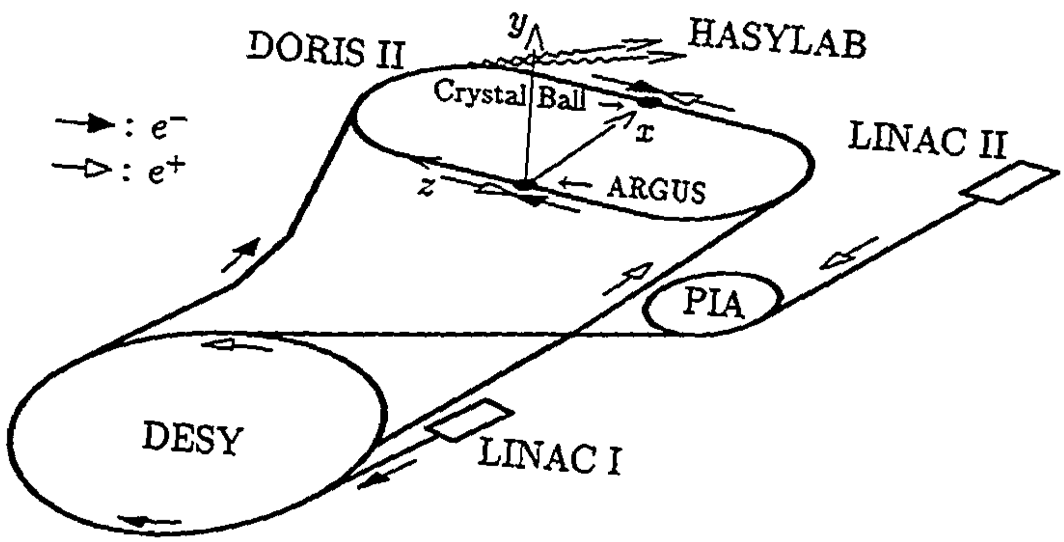

Figure 2.1: The DORIS II storage ring

are replenished, corresponding to beam lifetimes of 2-3 hours. Beams are focused at the interaction points to about 80 μm in y, 500 μm in x and 2.5 cm in z,(the coordinate system is defined with z along the beam axis and x in the plane of the storage ring), if they are assumed to have Gaussian distributions.

An important quantity of a storage ring is the luminosity, L, which is defined as:

$$\mathcal{L} = \frac{I^+ I^-}{4\pi e^2 f \sigma_x \sigma_y} \tag{2.1}$$

where I^+ I^- are the currents of the positron and the electron beams in Amperes respectively, e is the electron charge, f is the revolution frequency and σ_x, σ_y are the beam sizes in the x-y plane in cm. The luminosity during typical running conditions at DORIS is about $1 \times 10^{31} cm^{-2} s^{-1}$ and the typical integrated luminosity collected by the detector per day is about 800 nb^{-1}. Data has been accumulated on the resonances $\Upsilon(1S)$, $\Upsilon(2S)$, $\Upsilon(4S)$ and in the continuum, that is at energies which lie away from resonances. Here, the continuum data are taken at energies just below each of the resonances mentioned, and they mainly comprise events of the type $e^+e^- \to c\bar{c}$. The Υ system is described in Section 1.2. At DORIS II the $\Upsilon(4S)$ resonance has a visible cross section of 0.95$\pm$0.05 nb and "sits" on top of a continuum background of 2.5 $\pm$ 0.2 nb. For the work described in this thesis, the $\Upsilon(4S)$ data are used as a source of B mesons. The continuum data below the $\Upsilon(4S)$ resonance are also considered since they provide a description of the continuum background underneath the resonance.

2.2 The ARGUS detector

The ARGUS detector [28] is a magnetic solenoidal spectrometer which was designed as a universal tool to analyze final states from electron-positron interactions in the energy range of the Υ resonances. In this region of centre-of-mass energies of approximately 10 GeV, a large variety of physics topics can be studied including:

- weak decays of B mesons produced in the decay of the $\Upsilon(4S)$ resonance,
- direct Υ decays and transitions between the various Υ states,
- decays of charmed hadrons produced in non-resonant e^+e^- annihilation,
- weak decays of τ leptons, which are produced in the QED process $e^+e^- \rightarrow \tau^+\tau^-$
- two-photon interactions, i.e. interactions in which the electron and positron do not annihilate, but instead interact via two emitted virtual photons.

The study of these processes leads to a number of design requirements for the ARGUS detector. Since B meson decays have high multiplicities and are almost isotropic, a very large solid angle coverage is necessary in order to achieve a high acceptance for the particles produced in B decays. Good momentum resolution for charged particles over a wide momentum range is needed since the momenta of the decay products of B mesons are low in the laboratory frame, while those from continuum production of charmed mesons may extend to several GeV/c. Similarly, for neutral particles, good energy and space resolution are important. Furthermore, the detector must provide excellent particle identification, again over a large momentum range, in order to suppress the large combinatorial background encountered in high multiplicity events.

To meet these requirements the ARGUS detector, shown in Figure 2.2, was constructed in fine segments from components with the best possible resolution and the lowest possible multiple scattering. Proceeding from the interaction point outwards, ARGUS consists of a Vertex Drift Chamber (VDC) replaced in 1990 by a Micro-Vertex Drift Chamber (μ-VDC), the Main Drift Chamber (DC), the Time of Flight counters (TOF), the Shower counters (SC) and finally a set of Muon Chambers (μC) outside the magnet coil and the return yoke.

Charge particle identification is realized both through measurement of the specific energy loss, dE/dx, in the main drift chamber and through measurement of the velocity using the Time-of-Flight system. The vertex drift chamber adds 8 more

ARGUS

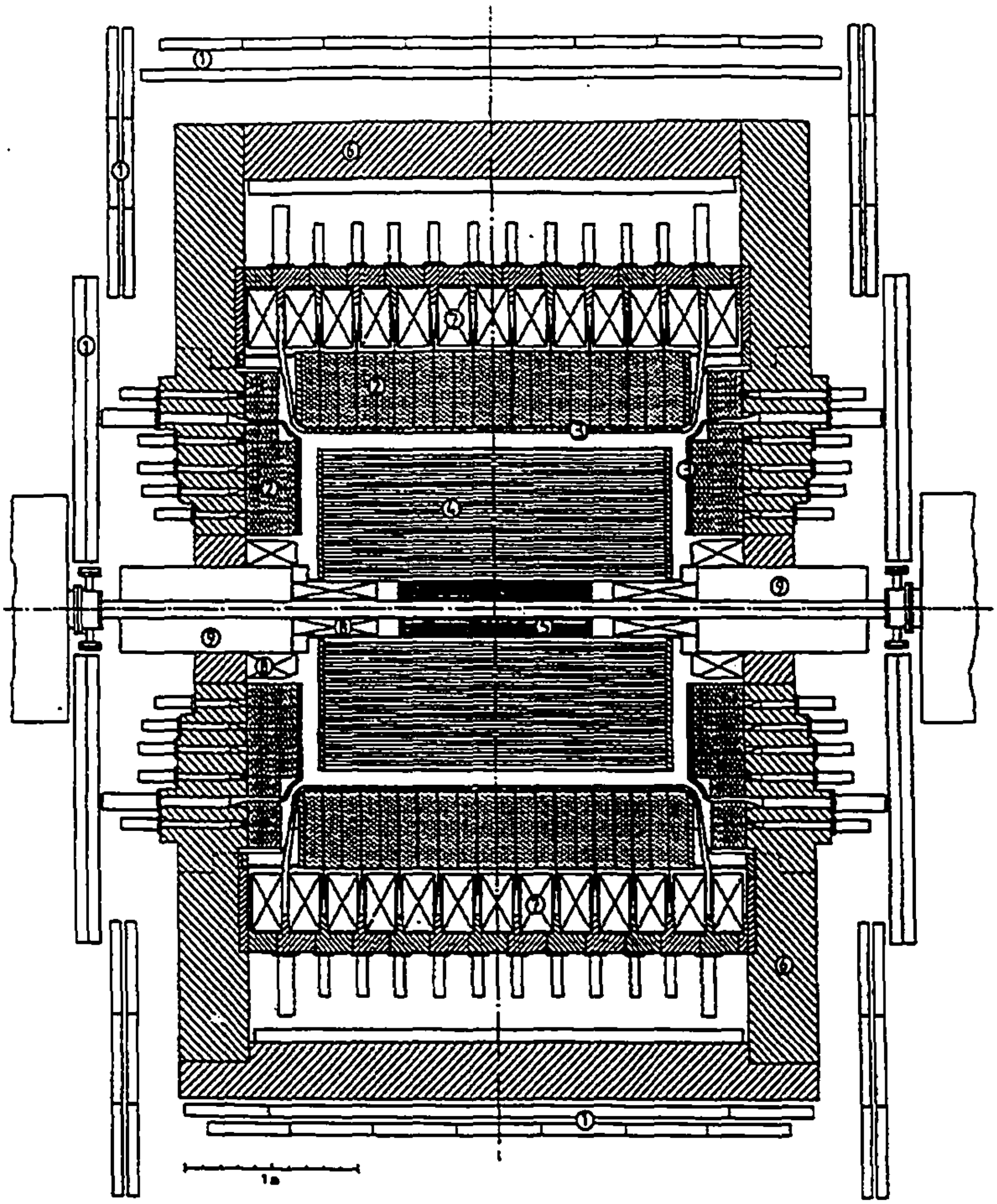

1. Muon chambers
2. Shower counters
3. Time of flight counters
4. Drift chamber
5. Vertex chamber
6. Iron yoke
7. Solenoid coils
8. Compensation coils
9. Mini beta quadrupole

Figure 2.2: The ARGUS detector

layers of information to that of the drift chamber, thus providing a considerable improvement in the accuracy of the measurement of the track parameters and vertices. Discrimination between electrons and hadrons and measurement of the energy of photons are performed by the electromagnetic calorimeter. Identification of muons is achieved by the three layers of muon chambers.

The components of the ARGUS detector are discussed in more detail in the following pages.

2.3 The ARGUS magnet

The ARGUS magnet system consists of the main solenoid which is constructed of 13 separate coils and provides a 0.8 Tesla field, the mini-beta quadrupoles and the inner and outer compensation coils. The field is known to a precision of better than 0.1% within the volume occupied by the main drift chamber allowing the good spatial resolution of the drift chamber to be converted to a good momentum resolution. The mini-beta quadrupoles are introduced to provide strong focusing of the beam in the vertical plane, thereby increasing the luminosity. A set of compensation coils were placed around the mini-beta quadrupoles to protect their field from leakage from the main solenoid field. A second set compensates for the influence of $\int B\,dl$ from the ARGUS magnet on the beam orbit.

2.4 The main Drift Chamber

The drift chamber is the most important component of the ARGUS detector [29] and as in all HEP experiments is considered the heart of the experiment. It provides information on the position, the momentum and the size of the energy deposition for charged particles.

The chamber has a cylindrical geometry with inner and outer diameters of 30 and 172 cm respectively and a length of 2 m. The inner wall consists of 3.3 mm thick carbon fiber epoxy composite to minimize multiple scattering and the outer wall is composed of 6mm aluminum.

5940 sense and 24588 potential wires are arranged in 36 concentric layers, forming 5940 drift cells, each 18 mm by 18.8 mm in size. In order to allow measurements of the z-coordinate of tracks, half the layers are arranged so that the sense and field wires lie at an angle to the axis of the chamber i.e. in the order $+\alpha, 0°, -\alpha, 0°$. The stereo angle α increases with the radius r as $\sqrt{r}$ from 40 mrad in the inner most layer to 80 mrad in the outermost layer. The values are chosen to limit the maximum displacement of a sense wire from the center of the cell to 1mm.
The layout of the wires is shown in Figure 2.3. The chamber is operated with a gas mixture of 97% propane (C_3H_8), 3% methylal ($CH_2(OCH_3)_2$) and 0.2% water vapour. The water was added after discharges occured in one of the chamber's sectors [30]. Propane was chosen due to its narrow Landau distribution i.e. the energy loss along the length of the particle track fluctuates less with propane than with other gases typically used.

Charged particles passing through the drift chamber ionize the gas along their path. The electrons and ions from this initial ionization then cause further ionization of the gas. The electrons resulting from this process drift toward the positively charged sense wires which then produce pulses which are recorded by the chamber electronics. The field wires shape the electric field around each sense wire, so that the time needed by the electrons to drift to the wire is used to determine the distance of the charged track from the wire. The magnitude of the recorded pulse is used to infer the specific ionization deposited along the track length, (dE/dx), which is further used for particle identification.

In order to maintain the data quality, the drift chamber is monitored and calibrated on a regular basis. Pulser runs, during which a pulse of known amplitude is provided to each ADC, are performed daily to supply the calibration constants for the dE/dx measurements. In addition, daily trim runs are performed on the TDC's to maintain their time resolution and hence the spatial accuracy of the chamber

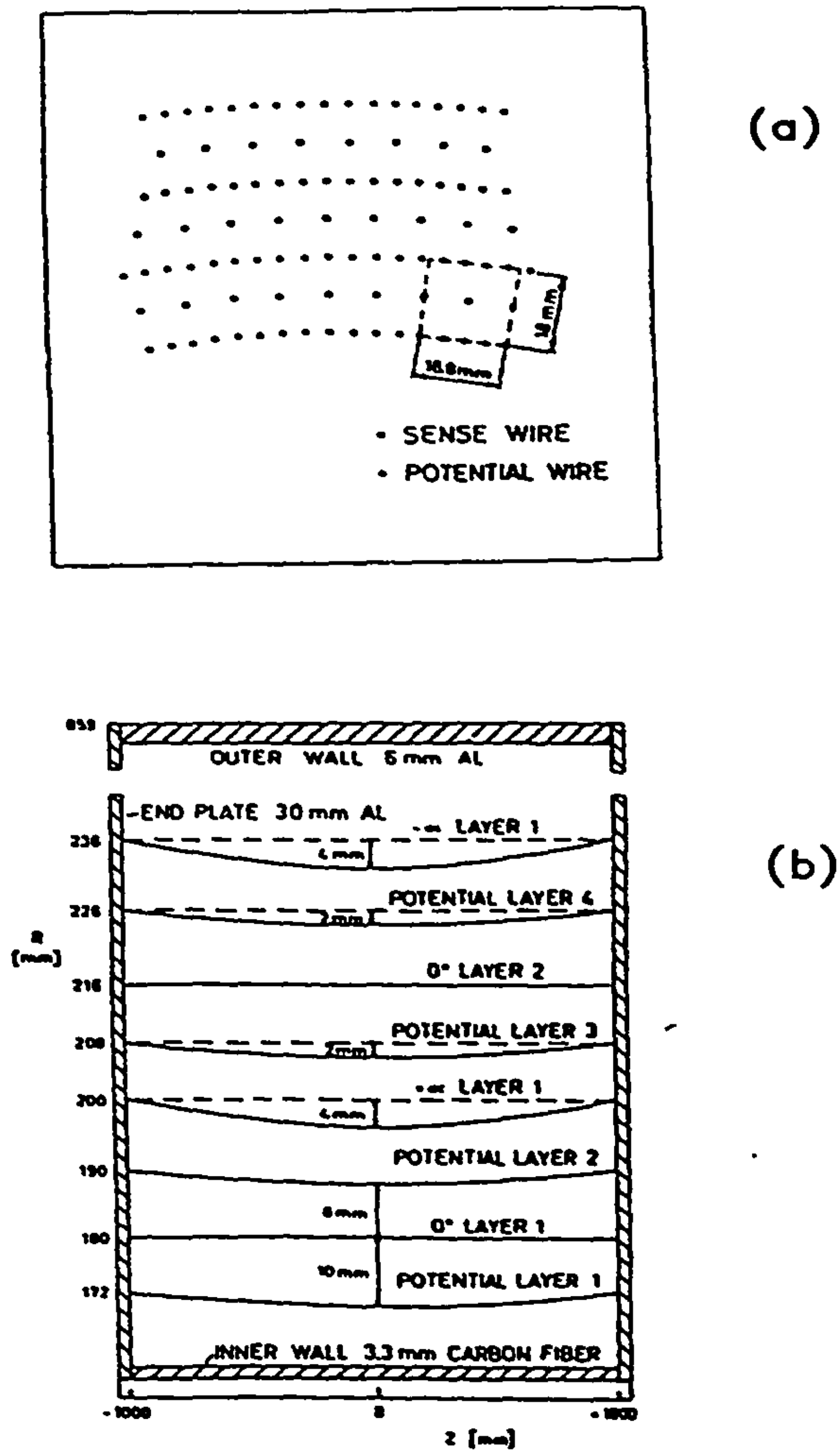

Figure 2.3: Cross sections of the Drift Chamber. a) perpendicular b) parallel to the beam axis.

measurements.

For fast particles ($p > 1\ GeV/c$), the momentum resolution is dominated by the errors on the track position measurement and is given by the expression :

$$\frac{\sigma(P_T)}{P_T} = 0.009 \cdot P_T\ [GeV/c] \tag{2.2}$$

where P_T is the transverse momentum of the particle. For momenta below 1 GeV/c, the momentum resolution can be expressed as

$$\frac{\sigma(P_T)}{P_T} = \sqrt{0.01^2 + (0.009 \cdot P_T\ [GeV/c])^2} \tag{2.3}$$

The constant term represents the contribution of multiple scattering which dominates the resolution in this momentum region.

The non-zero angle of the stereo wires with respect to the longitudinal chamber axis allows the determination of the track coordinates along the beam direction, and therefore measurement of the polar angle θ of the tracks. This in turn makes it possible to convert the measurement of P_T to a measurement of P. Figure 2.4 shows a distribution of the specific energy loss, dE/dx, versus momentum.

2.5 The Vertex Drift Chamber

The ARGUS Vertex Drift Chamber (VDC) [31] allows precise measurement of a track's position very close to the interaction point thus enhancing the spatial resolution of the primary vertex position and improving the accuracy in reconstructing secondary vertices from short lived particles.

The chamber is a small cylindrical high-resolution drift chamber with inner and outer diameters 10 cm and 28 cm respectively, and a length of 1 m. It was designed to fit into the space available between the drift chamber and the beam pipe and between the two compensation coils thereby providing 95% solid angle coverage for

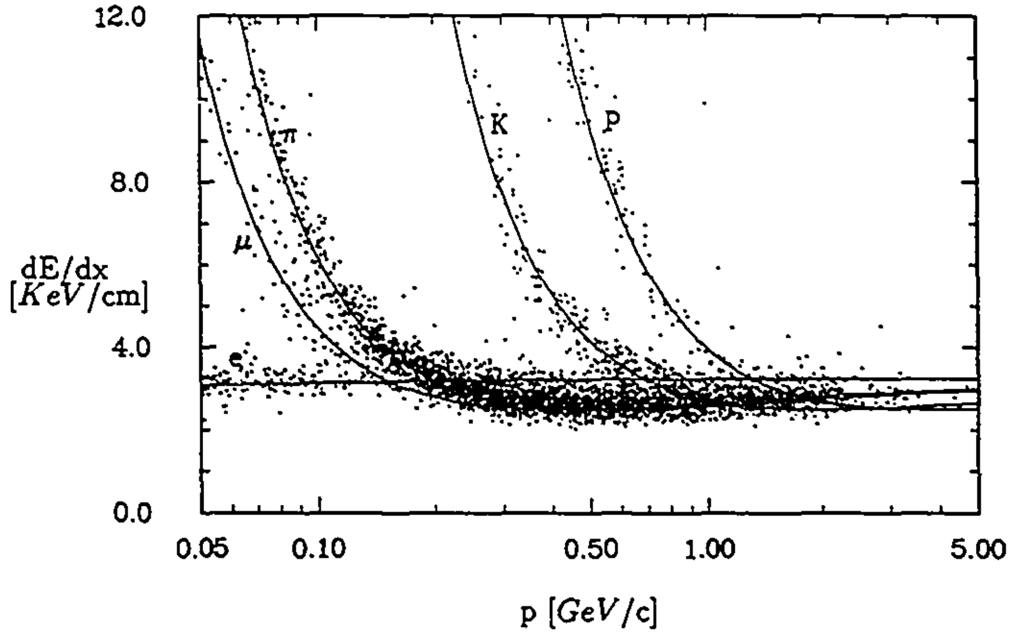

Figure 2.4: Specific energy loss versus the momentum of the particle.

tracks hitting all layers. In order to reduce multiple scattering, the inner and outer cylindrical walls of the VDC are made of a carbon fiber epoxy composite. There are 594 sense wires and 1412 field wires arranged in a closed-packed hexagonal cell pattern to maximize the number of hits per track. (Fig. 2.5)

The small size of the drift cells (inscribed radius 4.5mm) is necessary in order to be able to maintain good efficiencies at high track densities using single hit electronics. All wires are parallel to the chamber axis, and therefore no information is obtained concerning the track coordinate along the beam direction.

The chamber is operated with pure CO_2 gas at a pressure of 1.5 bar and a high voltage of 3500V. In order to slow down the degradation of the chamber caused by deposits on the wires, 0.3% water vapour was added to the VDC gas, as it was done in the case of the main DC.

The spatial resolution as determined from Bhabha scattering events is better than $100\mu m$ for about half the cell (Fig 2.6).

For multihadron events the effective resolution is worse by a factor of about 1.4

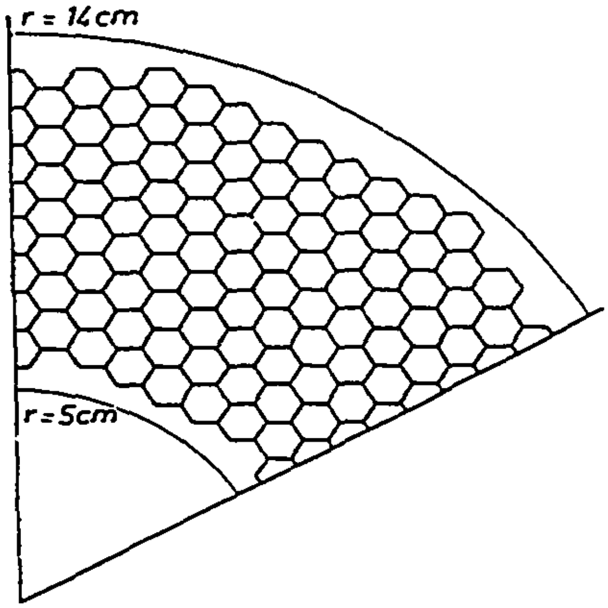

Figure 2.5: The hexagonal cell pattern of the vertex drift chamber. The sense wires are located in the center of the hexagon and the field wires on the corners.

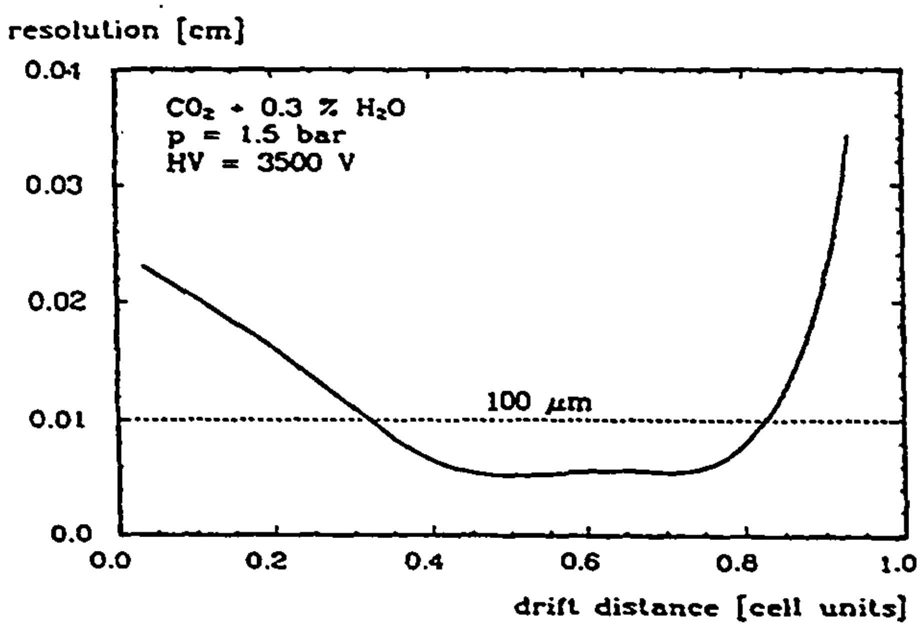

Figure 2.6: VDC resolution versus drift distance.

mainly due to different ionization effects, and multiple scattering of low momentum tracks. A great improvement on the precision of the measured track parameters for charged tracks was achieved using the additional information from the VDC in the track fit. The momentum resolution for 5 GeV/c muons improved from $\frac{\sigma(P_T)}{P_T} = 0.9\% \cdot P_T$ to $0.6\% \cdot P_T$. Single high momentum electron tracks can be extrapolated to the vertex with a precision better than $100\mu m$ as found by studying the distance of closest approach between the two tracks in Bhabha events. The improved track and vertex parameters lead to considerably higher reconstruction efficiency for secondary vertices from K_s^0 and Λ decays.

2.6 The micro-Vertex Drift Chamber

In March 1990 the VDC was replaced by a micro-vertex drift chamber (μVDC) [32]. The μVDC was designed to resolve secondary vertices from the decays of short lived particles like charmed mesons or τ leptons. This requires high resolution in both the $r - \phi$ and $r - z$ projections, and ability to measure the track coordinate close to the beam line. A schematic drawing of the μVDC is shown in Figure 2.7.

It is a cylindrical drift chamber with 1070 sense wires arranged in 16 layers, of which four are axial. The other 12 layers have stereo wires with angles of alternately $+45°$ and $-45°$ with respect to the beam axis. The stereo wires are guided around the chamber axis using a mechanical support structure of 5 longitudinal plates ("vanes"), extending between the two endcones. The vanes are made of 0.94mm thick beryllium sheet. This material was chosen because it combines great mechanical stiffness with low multiple scattering. Due to the small drift cells (5.320 $\times$ 5.178mm^2), the μVDC was designed to run at high pressure (up to 4 bar) in order to compensate for the resolution deterioration due to ionization statistics towards the sense wire. The small diameter beryllium beam pipe forms also the inner wall of the μVDC. At first pure CO_2 with 0.3% admixture of water was used as the chamber gas and the pressure was set to 2.45 bar. Later a mixture of 80% CO_2 and

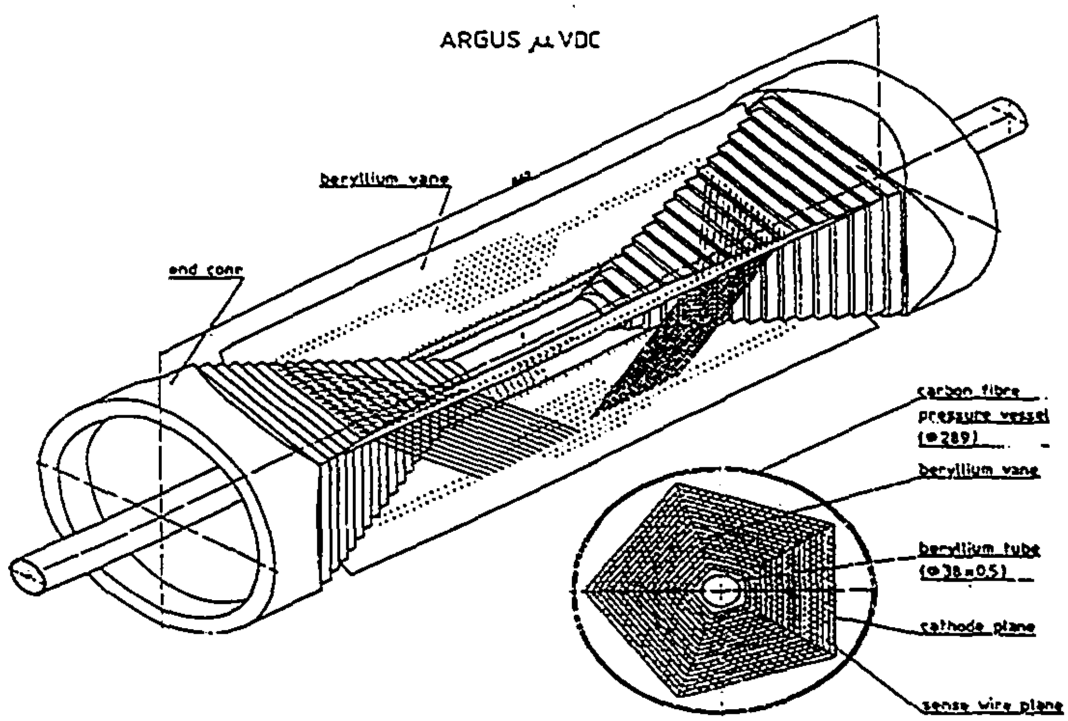

Figure 2.7: Schematic view of the μVDC.

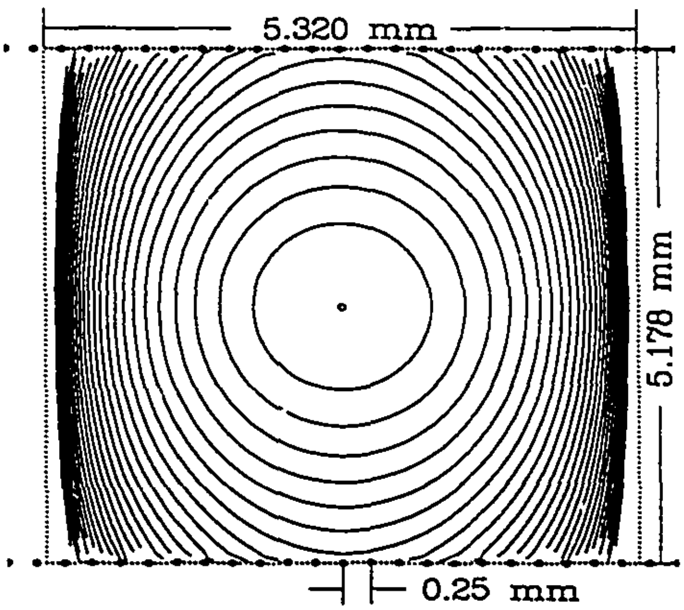

Figure 2.8: Design of the μVDC drift cell. Sense wire (open circle) and cathode wires (full circles) are not parallel in the stereo layers. The isochrones for CO_2 at 2.45 GeV/c and HV=23350 V, for drift times 20-520ns in steps of 20ns are also shown.

20% propane with admixture of methylal (3%) and water (0.3%) was used and the chamber was operated at a pressure of 3.1 bar.

For the μVDC calibration bhabha events in the barrel region were used. To measure the spatial resolution, the standard deviation of the distribution of residuals was taken; the residual being the difference of the measured and the fitted distance between the track and the sense wire. When drift distances are calculated from the measured drift times, an angular correction needs to be taken into account. This correction is due to the fact that the shape of the isochrones (shown in Fig. 2.8) is increasingly non-circular for distances further from the sense wire.
Figure 2.9 demonstrates the effect of this angular correction. After this correction is applied, the spatial resolution obtained is shown in Figure 2.10.

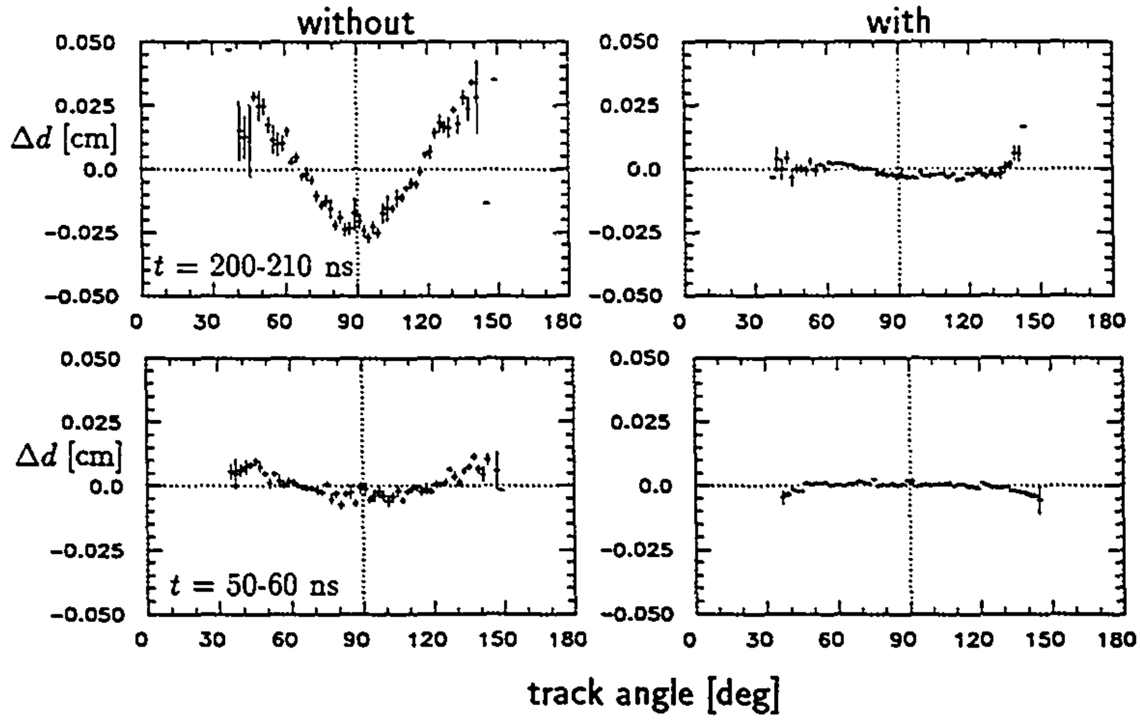

Figure 2.9: Residuals vs. track angle in the drift cell for two drift time intervals with and without application of the angular correction of the measured drift time.

2.7 The Time of Flight System

The ARGUS Time of Flight system (TOF) [33] consists of 160 scintillation counters, 64 of which are located in the barrel region and 48 in each endcap. The barrel covers 75% and the endcaps ($0.78 < |\cos\theta| < 0.95$) cover 17% of the full solid angle.

The main purpose of the TOF system is to determine the velocities of charged particles by measuring their flight time. Combining this with the momentum measured in the drift chamber, an estimate of the rest mass, and thus the identification of a charged particle, can be made.

$$\frac{1}{\beta} = \frac{c \cdot TOF}{l} = \sqrt{1 + \left(\frac{mc^2}{pc}\right)^2} \Rightarrow m^2 = p^2 \cdot \left(\frac{1}{v^2} - \frac{1}{c^2}\right) \tag{2.4}$$

The TOF system is also a part of the ARGUS trigger.

Scintillation light generated by a charged particle passing through a TOF counter

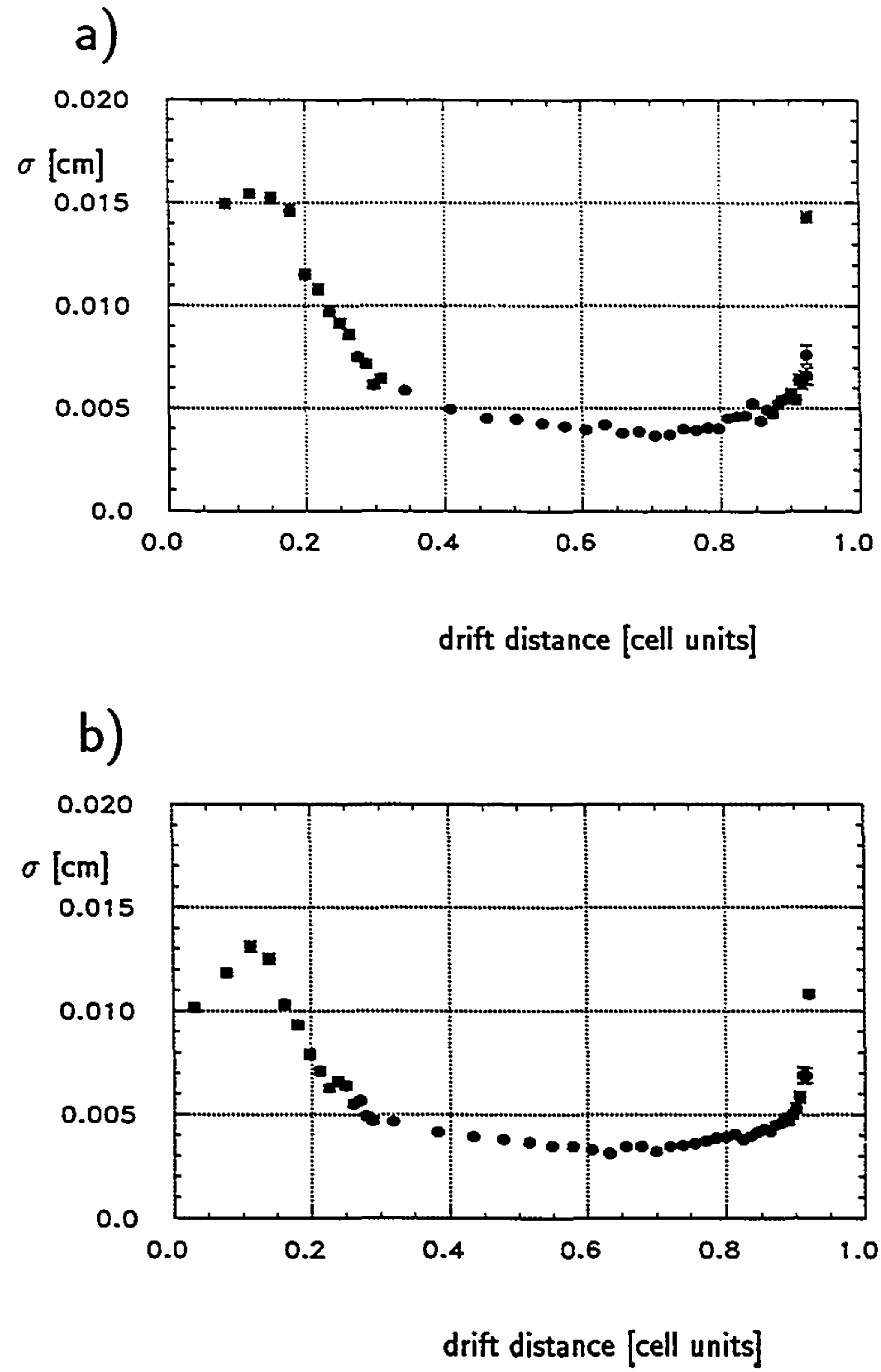

Figure 2.10: Spatial resolution for a) CO_2 at 2.45 bar and b) CO_2/propane at 3.1 bar.

travels the length of the counter before entering a light guide which transports the light to photomultipliers operating outside the main magnetic field of the detector. Signals from the photomultiplier tubes are sent to a splitting unit which provides signals to a discriminator, whose logical signal, after a cable delay of 200 ns, stops the TDC, and a charge-sensitive ADC. The ADC information is used off-line to correct the time measured by the TDC. An rms TOF resolution of 220ps is achieved for hadrons. For constant time resolution, the mass resolution varies with the square of the momentum

$$\sigma(m^2) = 2 \cdot \left(\frac{p}{l}\right)^2 \cdot TOF \cdot \sigma(TOF) \tag{2.5}$$

For a time resolution of 200 ps, this measurement leads to three standard deviation π/K separation up to 700 MeV/c, and K/p separation up to 1200 MeV/c. The particle identification power of the ARGUS TOF system is shown in a scatter plot of mass squared versus momentum in Figure 2.11.

2.8 The Electromagnetic Shower Counters

Another important component of the ARGUS detector is the electromagnetic calorimeter [34]. The ARGUS shower counter system serves to:

- measure the energy of electrons as well as the energy and direction of photons;
- separate electrons from muons and hadrons using the shape of the shower and the amount of energy deposited in the counters;
- perform an on- and off-line measurement of the luminosity;
- construct a total energy trigger that selects events with an energy deposition in the calorimeter exceeding a preset threshold.

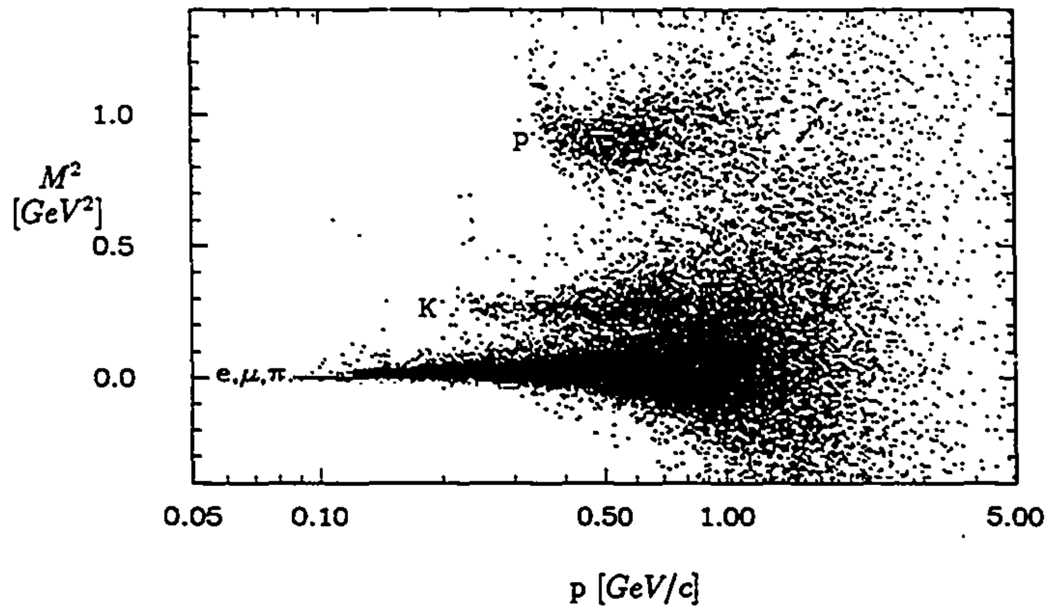

Figure 2.11: Mass squared from TOF measurements versus the momentum of the particle for hadron tracks.

The calorimeter is composed of 1760 lead-scintillator sandwich type shower counters which cover 96 % of the total solid angle. It consists of two parts: the barrel calorimeter ($|cos\theta| < 0.75$) which detects particles in the central region, and the endcap calorimeter ($0.75 < |cos\theta| < 0.96$) which detects particles travelling in the forward and backward regions.

Electrons interact with the calorimeter material primarily through radiation and to a lesser extend through ionization. The bremsstrahlung photons then scatter off the heavy lead nuclei producing e^+e^- pairs which further cascade. Hadrons also interact with the heavy lead nuclei but through a different process. An energetic hadron's collision might result in the break up of the nucleus, thus leading to a hadronic interaction cascade, which normally has a much wider lateral spread than the electromagnetic shower. Finally, muons are too heavy to generate electromagnetic showers and cannot produce hadronic showers since they do not interact hadronically. For muons, the only significant contribution to the energy loss is the ionization process, and they therefore provide a *minimum ionizing* signal in the shower counters.

The shower counter modules are placed inside the magnet coil. The counters are read out by wavelength shifters which are coupled via light guides to photomultiplier tubes. The total amount of material in front of the counter is 0.16 radiation lengths in the barrel region and 0.52 radiation lengths in the endcaps. This arrangement allows the detection of photons with energies as low as $E\gamma \approx 0.05\ GeV$ with high efficiency and good energy resolution. The energy resolution at high energies was determined from the energy distribution of electrons from Bhabha scattering and of photons from the process $e^+e^- \rightarrow \gamma\gamma$. For low energy photons, the energy resolution is determined from the mass spectrum of π^0 and η mesons. The energy resolution achieved can be parametrized by the expression

$$\frac{\sigma(E)}{E} = \sqrt{0.072^2 + \frac{(0.065)^2}{E[GeV]}} \tag{2.6}$$

for the barrel region and by

$$\frac{\sigma(E)}{E} = \sqrt{0.075^2 + \frac{(0.076)^2}{E[GeV]}} \tag{2.7}$$

for the endcaps. The constant term is known to be due mainly to losses in the support region.

2.9 The Muon chambers

The ARGUS muon chambers [35] form the outermost part of the detector. These assist in muon identification because muons, as minimum ionizing particles, do not loose energy through showering processes and therefore have a good chance of passing through to the chamber layers. Most of the hadrons on the other hand are absorbed through nuclear interactions within the magnet coil and yoke, while electrons and photons shower long before they reach the muon chambers.

The chambers are installed in three layers, one between the magnet coil and yoke, and the other two outside the yoke. The inner layer covers 43% of the full solid angle and is separated by 3.3 absorption lengths of material from the interaction point. The outer two layers cover 87% of the full solid angle and are separated from the innermost layer by an additional 1.8 absorption lengths of material. The two outer layers have a 93% overlap. The presence of the absorbing material imposes a momentum cutoff for muons. This is 700 MeV/c for the inner and 1100 MeV/c for the outer layer of muon chambers. In total there are 218 chambers, each consisting of 8 proportional tubes of $56mm \times 56mm$ cross-section, and lengths of 1 to 4 m depending on their location in the detector. The efficiency of the muon chambers was determined from an off-line analysis of cosmic data where the tracks were traced from the central drift chamber to the muon detection system. In this way, an efficiency per layer, averaged over all chambers of $\epsilon = 0.98 \pm 0.01$ was determined.

2.10 The ARGUS Trigger system

The bunch crossing frequency of DORIS II is 1 MHz, leaving the experiment with 1 μs time to decide whether to accept the event or not. The ARGUS trigger system performs this decision in two separate steps. First, a fast pretrigger discriminates between background and "good" event candidates within 300ns. If a candidate for a "good" event is found, a slower second level trigger, called the *Little Track Finder*, (LTF), is activated, and this makes the final decision to accept an event or not.

2.10.1 The Fast Pretrigger

The fast pretrigger processes information from only the Time-of-Flight and the shower counters. The similar spatial segmentation and solid angle coverage of TOF and shower counters enables the combination of a basic trigger unit made up of a few TOF counters with a basic trigger unit made up of a few shower counters. The flexibility of the trigger is enhanced by the use of different subtriggers. ARGUS has four different fast pretriggers and two test triggers.

- The *Total Energy Trigger* (ETOT) is designed to detect events with balanced energy deposition in the shower counters. The shower energies of both detector hemispheres are summed separately and in each hemisphere must exceed a threshold corresponding to 700 MeV deposited energy.

- The purpose of the *High Energy SHower trigger* (HESH) is to detect events where single particles carry a large portion of the total energy. This trigger uses only the barrel shower counters. There are 16 HESH trigger groups in total. If the signal from one HESH group exceeds a preset threshold corresponding to roughly 1 GeV, a trigger signal is generated.

- The *Charged Particle Pre-Trigger* (CPPT) is designed to detect events with charged particles. At least one track in each hemisphere is required; a track being defined by the coincidence of a TOF counter group and a shower counter group which cover each other. A TOF CPPT group is formed by four neighboring TOF counters, while a shower CPPT group consists of 6 adjacent rows of shower counters. In total, there are 16 CPPT groups in each hemisphere. The threshold corresponds to an energy deposit of 50 MeV. The energy deposited by a minimum ionizing particle is approximately 160-200 MeV, ensuring an efficiency of more than 95% for those particles. The coincidence of signals from the TOF and shower counters of all CPPT groups are transferred to the central CPPT unit. This forms an .OR. of all signals in one hemisphere, and makes an .AND. between both hemispheres.

- The *Coincidence MATRIX Trigger* (CMAT) was designed for events with tracks opposite in the azimuthal angle ϕ, but not necessarily in z, that is both tracks can be in the same hemisphere. Here, tracks are defined as in the CPPT, and the signals from CPPT groups at the same ϕ are .OR.-ed. This leads to a set of 16 channels, which are fed into a 16×16 coincidence matrix unit whose elements can be programmed in hardware to select events fulfilling the conditions desired.

- The *Cosmic Ray Trigger* is the first test trigger. It triggers on cosmic muons travelling close to the beam line, and requires a coincidence between two opposite groups of four barrel TOF counters. This trigger is switched off during normal data taking. It is only used in order to test and calibrate the various detector components.

- The *Random Trigger* is another test trigger. It gives a random signal to all electronics at a rate of 0.1 Hz. It has been installed to estimate the random noise contribution to ARGUS events.

All pretrigger signals, except the one from the cosmic trigger, must be in coincidence with the bunch crossing signal delivered by the storage ring. As soon as a pretrigger is accepted, the pretrigger logic is inhibited in order to prevent further pretriggers during event processing. The logic is reset either by the second level trigger if the minimal trigger requirements are not fulfilled, or by the online computer after all processors have been read out and reset.

2.10.2 The Second Level Trigger (LTF)

The *Little Track Finder* (LTF) forms the second level of the ARGUS trigger [36]. This is a programmable electronic device which is activated when a pretrigger signal is received. It is capable of finding and counting circular tracks passing through the interaction point in the $r - \phi$ plane of the detector.

A track is characterized by a well-defined sequence of hits in the drift chamber and the TOF counters. The loaded memories of the LTF contain a complete list of these possible sequences, termed masks. The LTF then scans this list, compares its entries to the actual hit patterns of the event, and counts matches as found tracks. If the required number of tracks is found, the event is accepted. The operation time of the LTF depends on the hits in the drift chamber. During normal detector running, it is approximately 20 μs. The track finding efficiency of the LTF has been measured to be 97%, and is mainly determined by the drift chamber efficiency.

In order for an event to be accepted, at least two LTF masks are required for the CPPT and the CMATRIX triggers, one mask is required for the HESH trigger, while no mask is required for the ETOT trigger.

2.10.3 On-line DATA Acquisition

The hardware for the on-line data acquisition system consists of four major components. A CAMAC module system, a CAMAC booster, an online computer (DEC PDP 11/45) and a VAX 11/780 which was later replaced by a μVAX 3200. Data from the various detector components are digitized by a CAMAC system, and then read out by a fast microprocessor, the CAMAC booster. This constructs the complete event records, and passes them to the on-line computer. The PDP receives the data on an event-by-event basis and transfers them to the VAX which in turn sends them to the IBM main computer. The VAX disc is capable of short-term data storage in case the link to the IBM fails.

The PDP controls the calibration processes for the hardware components of the detector, monitors the most important operating parameters, and through a set of menus allows the operator to control the on-line process. The VAX is used to perform an on-line monitoring in order to maintain the quality of the data collected. For this reason, histograms describing the detector performance are accumulated, and continuously updated information on trigger rates, numbers of events transferred and integrated luminosity is provided.

Upon transfer to the IBM the data are written first to disk, and later to tapes to be used for off-line analysis.

2.11 Luminosity Monitoring

Luminosity determination in electron positron colliding beam experiments is usually performed by counting events from Bhabha scattering $e^+e^- \rightarrow e^+e^-$, since the cross section for this QED process is well known. The luminosity, $\mathcal{L}$, is given by the expression:

$$\frac{dN_{Bhabha}}{dt} = \mathcal{L} \cdot \sigma_{Bhabha} \tag{2.8}$$

where $\frac{dN_{Bhabha}}{dt}$ is the observed Bhabha rate and σ_{Bhabha} the visible Bhabha cross section. In ARGUS, an online luminosity monitor allows an estimation of the quality of the data, while the off-line luminosity determination is essential for calculating cross sections. The online luminosity monitor uses information from the endcap time of flight and shower counters. For a Bhabha count to be recorded, the signal from a shower counter group must be in coincidence with the signal from the TOF group in front of it. These signals must in turn be in coincidence with their "diagonal" counterpart in the opposite endcap. A further requirement is that the energy deposited in each endcap must exceed 1 GeV. The off-line luminosity determination is based on fully reconstructed Bhabha scattering events recorded in the barrel region of the detector. A track is accepted if its momentum is greater than 1 GeV and if the energy deposited in the calorimeter exceeds 0.6 GeV. Events are required to have exactly two charged tracks with an opening angle larger than 165°. The systematic error on the luminosity is 1.8 %, except in the $\Upsilon(1S)$ resonance region where it is $^{+1.8}_{-2.5}\%$.

2.12 Event Reconstruction

The ARGUS raw data, i.e. ADC, TDC, and hit information from the various detector components, are processed by the ARGUS main reconstruction program to find particle tracks, calculate their momenta and determine their identity. The ARGUS program is designed as a set of modules most of which are independent of the others, and are responsible for the analysis of individual detector components. This modularity facilitates reanalysis of parts of the data. The ARGUS program also has a built-in feature which allows the interactive display of reconstructed events.

2.12.1 Drift chamber reconstruction and pattern recognition

A charged particle travelling with constant velocity in a homogeneous magnetic field parallel to the z-axis follows a helix which is described by specifying five parameters at a uniquely defined reference point. The reference point is usually chosen to be the track point which, projected into the x-y plane, is closest to the origin. The track parameters used are:

- κ : the curvature of the helix (the inverse of its bending radius R) multiplied by the charge of the particle in units of e ($Q = \pm 1.$)
- d_0 : the signed distance between the origin and the reference point measured in the x-y plane, also multiplied by the charge Q
- ϕ_0 : the azimuthal angle of the tangent to the track at the reference point
- z_0 : the z-coordinate of the reference point
- $cot\theta$: the cotangent of the polar angle θ, with respect to the z-axis.

The first three parameters describe the projection of the helix onto the x-y plane, and the information about them is deduced from paraxial as well as stereo wires; whereas information regarding z_0 and $cot\theta$ can be obtained from stereo wires only.

The reconstruction of tracks proceeds through two steps. Firstly, pattern recognition is performed in the x-y plane using only the paraxial wires. Then, the reconstruction is completed by adding the $cos\theta$ and z information. The search for tracks is performed starting from the outermost layer, where the conditions are expected to be the cleanest. Since three drift chamber hits are needed to define a circle in the x-y plane, the algorithm starts by making triplets of hits which are possible segments of a track. For each triplet, the curvature κ is determined. A fourth hit is added to a track by comparing the curvature κ calculated for a triplet made of the hit considered and two hits of the original triplet. In a similar way, a fifth and any following hit can be added. The decision about whether or not a new hit will be assigned to a track candidate is made on the basis of the χ^2-like quantity

$$\frac{(\kappa_{new} - \kappa_{old})^2}{\sigma^2_{new} + \sigma^2_{old}} \tag{2.9}$$

which is required to be less than 25. Once a new hit has been added, the average of the two curvatures (κ_{new} and κ_{old}) is calculated and stored. This procedure is repeated until all possible hits have been tested. Also, the procedure takes into account the drift time circles of the hits and attempts to resolve left-right ambiguities. In most cases the algorithm succeeds, but if ambiguities cannot be resolved multiple possible tracks are stored. After a track is completely reconstructed, the parameters ϕ_0 and d_0 are determined. For an event to be accepted, there must be at least two tracks with $d_0 < 1.5cm$.

When all possible track candidates are found in the x-y plane, the pattern recognition moves to three dimensions and includes the information from the stereo wires. This is done in a method similar to the one described above. The remaining parameters, z_0 and $cot\theta$ are then calculated. After the pattern recognition is completed, all wires are uniquely assigned to tracks, and approximate values for the five track parameters are determined.

The next phase is the track fit. This uses as input the track parameters determined by the pattern recognition and performs an iterative simultaneous least-squares fit to improve the track parameters. For a low momentum particle, the energy loss inside the drift chamber volume causes substantial deviations from the predicted trajectory. Hence the theoretical prediction for the ionization loss for the mass hypothesis from the dE/dx analysis is used to correct the predicted trajectory. Multiple scattering is also taken into account by dividing the track into segments and allowing for kinks between adjacent segments. After the track recognition in the main drift chamber has been completed, the tracks are traced back into the vertex drift chamber. All hits on their projected path are then assigned to the tracks. Since z-information is not available in the VDC, no attempt to find new tracks is made. An improved track fit is then performed using the VDC hits only, but with the track parameters determined from the DC fit employed to impose a constraint.

2.12.2 Vertex Reconstruction

The vertex finding procedure used with the ARGUS reconstruction program was designed for identifying possible interaction vertices and separated vertices of neutral particles which produce reconstructable tracks upon decay. The tracks are first extrapolated close to the beam line. In this procedure, energy loss is accounted for using the theoretical ionization loss for the mass hypothesis from the dE/dx measurement; errors due to Coulomb scattering in the beam pipe or in the chamber walls are included where appropriate. To find the coordinates of the primary vertex an iterative least squares fit procedure is used. The contribution of each track to the χ^2 is examined, and if no single contribution exceeds a predetermined value, the vertex which minimizes the χ^2 is retained. If the minimization procedure does not converge the track with the largest contribution to the χ^2 is discarded and the process repeated. After the main vertex is successfully identified, all remaining unassociated track pairs are considered for secondary vertices. A final pass is then made over all pairs of tracks in order to improve the efficiency for identifying K_s^0 and Λ vertices.

2.12.3 Particle identification

ARGUS provides two independent methods for charged particle identification, namely the measurement of the specific energy loss due to ionization in the drift chamber gas, and the measurement of the time-of-flight, which together with information on the momentum from the drift chamber allows the reconstruction of a particle's mass.

Energy loss

The energy deposition in a drift chamber cell is calculated for each hit on a track, using the ADC value and information derived from the track fit such as the track length in the drift cell and the distance of the track from the wire. A correction is made to the ADC values of the wires assigned to the track according to the angle between the track and the sense wire. The energy loss of a particle in a medium follows a Landau distribution, and since this has distinct long tails, a truncated mean is used to estimate the most probable energy loss. The truncated mean is obtained by discarding, for each track, the highest 30% and the lowest 10% of the measured dE/dx values, and then averaging the remaining measurements. This method is applied to make the distribution of the average energy loss resemble a Gaussian distribution. The energy loss per unit distance of a charged particle traversing a medium is given by the Bethe-Bloch equation:

$$\frac{dE}{dx} = \frac{D \cdot Z_{med} \cdot \rho_{med}}{A_{med}} \left[\frac{z_{inc}}{\beta}\right]^2 \times \left[ln\left(\frac{2m_e\gamma^2\beta^2c^2}{I}\right) - \beta^2 - \frac{\delta}{2} - \frac{c}{Z_{med}}\right](1+\nu)$$

where $D = 4\pi N_A r_e^2 m_e c^2 = 0.3070\ MeV \cdot cm^2/gr$, Z_{med} and A_{med} are the charge and mass numbers of the medium, ρ_{med} the density of the medium, and I, δ, c and ν are phenomenological functions [2]; which depend on the particle velocity. From the measurement of the energy loss one can determine β. In conjunction with the momentum measured in the track fit, an estimate of the mass of the charged particle can then be made. In this way, the identity of a particle is determined by comparing the truncated mean energy loss with that theoretically expected for different particle species. A χ^2 for each mass hypothesis is calculated:

$$\chi_i^2(dE/dx) = \frac{\left(\frac{dE}{dx} - \frac{dE}{dx_i^{th}}\right)^2}{\sigma_{dE/dx}^2 + \sigma_{th}^2} \qquad \text{where } i = e, \mu, \pi, k, p. \tag{2.10}$$

dE/dx_{meas} and dE/dx_i^{th} are respectively the measured and theoretical specific ionization losses for the i^{th} particle hypothesis respectively; $\sigma_{dE/dx}$ and σ_{th} are the corresponding uncertainties.

Time-of-Flight analysis

A procedure similar to the one described above is used for the TOF information. The velocity measured from the TOF system is compared to that expected for the different particle hypotheses, resulting in a χ^2 of the form

$$\chi_i^2(TOF) = \frac{\left(\frac{1}{\beta} - \frac{1}{\beta_i^{th}}\right)^2}{\sigma_{TOF}^2 + \sigma_{th}^2} \qquad (i = e, \mu, \pi, K, p) \tag{2.11}$$

where β, β_i^{th} are the particle velocities, measured and expected for the i^{th} particle hypothesis respectively, and σ_{TOF} and σ_{th} are the uncertainties of the measured and expected velocities, the latter coming from the momentum uncertainty. Eventually, at high momentum, particles with $\beta \longrightarrow 1$ can no longer be differentiated within the timing resolution of the TOF system.

Shower Counter analysis

Data from the shower counter ADC's are converted into measurements of energy deposition via a set of calibration constants pre-determined for each counter using Bhabha events. Using the information from the shower counters and the fact that the lateral energy deposit for electrons, muons and hadrons is different, separation of these particles can be achieved. Electrons are the only particles that deposit almost all their energy in the calorimeter. Also, for electrons the deposited energy and the particle momentum are strongly correlated, while for hadrons no correlation is observed. Furthermore, the lateral energy deposits of electrons and interacting hadrons differ drastically. For hadrons the energy is shared by more counters and is distributed more uniformly. Two "shower shape" parameters are therefore defined. The lateral width of the energy distribution

$$E_{lat} = \sum_{i=1}^{3} \frac{(\vec{r_i} - \vec{r})^2}{< \Delta r >^2} \cdot E_i \tag{2.12}$$

where

- $\vec{r_i}$ is the position of the center of counter i

- E_i is the energy deposition in counter i (with $E_1 > E_2 > ... > E_n$)

- $< \Delta r >$ is the average distance between the two shower counters and

- $\vec{r}$ is the position of the center of gravity of the shower

and the fractional lateral energy spread

$$f_{lat} = \frac{E_{lat}}{E_{lat} + E_1 + E_2} \tag{2.13}$$

The two counters with the highest energy deposit E_1 and E_2 do not contribute to E_{lat}. The variable f_{lat} is used for the separation of electrons from hadrons as shown in Figure 2.12.

This method works only for energies greater than 0.6 GeV because hadronic showers do not develop at lower energies, and the particle identification capability based on it improves with increasing momentum. The energy deposition in a cluster of counters not associated with any charged track serves as the energy measurement of a photon.

Likelihood function

Since the dE/dx and TOF measurements are independent, the two χ^2 's can be combined to give a single charged-particle discrimination variable:

$$\chi_i^2 = \chi_i^2(dE/dx) + \chi_i^2(TOF) \tag{2.14}$$

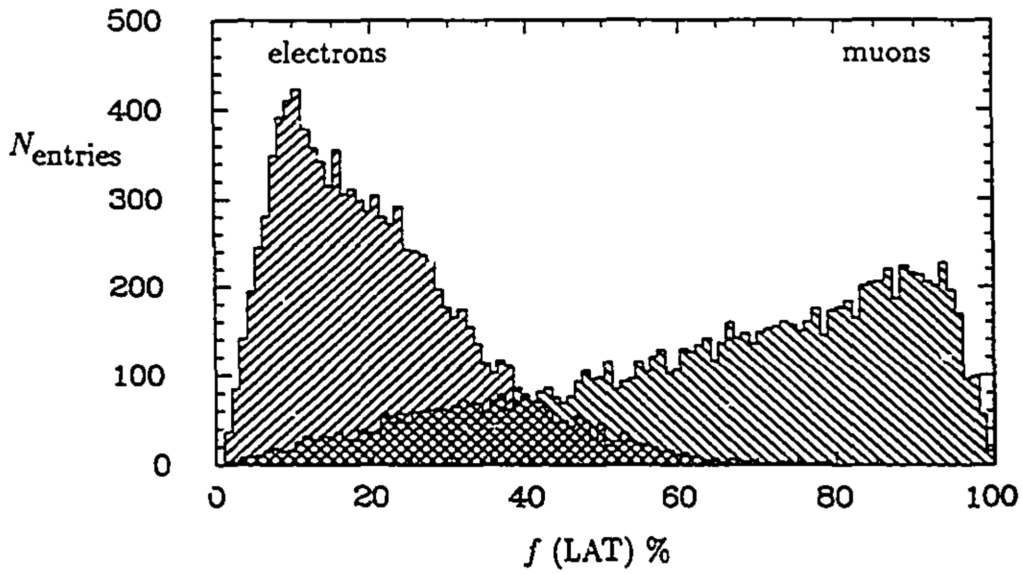

Figure 2.12: Distribution of f_{lat} for electrons and hadrons with $E \geq 1\ GeV$.

which is used to form a likelihood function

$$L_i = e^{\frac{-\chi_i^2}{2}} \qquad \text{where} \quad i = e, \mu, \pi, k, p. \tag{2.15}$$

From these likelihood functions, normalized likelihoods λ_i are constructed for each mass hypothesis:

$$\lambda_i = \frac{w^i L_i}{\sum_{j=e,\mu,\pi,k,p} w_j L_j} \tag{2.16}$$

where w^i are the relative production abundances. Roughly 80% of all measured charged particles can be uniquely identified by the dE/dx and TOF measurements.

As noted above, electrons are identified by independent dE/dx and TOF measurements, as well as by using shower counter information. However, none of these methods provide particle identification over the entire momentum range. Therefore, a combination of all available information is used in the form of a universal likelihood function. The normalized likelihood has the form

$$\lambda^e = \frac{w^e \prod_i p_i^e(x)}{\sum_j w^j \prod_j p_i^j(x)}, \qquad \text{where} \quad i = dE/dx, TOF, SC; \quad j = e, \mu, \pi, k, p.$$

where $p_i^j(x)$ are the probabilities for measured parameters x to be identified as particle type j by device i. The weights w^j are again the relative production rates.

For muon identification, a similar procedure is applied. Here, there is an additional condition to be met, namely that the tracks reconstructed in the drift chamber can be traced through the electromagnetic calorimeter, magnet coils and iron yoke, and can be assigned to hits in the muon chambers. During tracing, multiple Coulomb scattering, magnetic field and energy loss are taken into account. In this case the normalized likelihood has the form

$$\lambda^{\mu} = \frac{w^{\mu}\prod_i p_i^{\mu}(x)}{\sum_j w^j \prod_j p_i^j(x)}, \qquad \text{where} \quad i = dE/dx, TOF, SC, MC; \quad j = e, \mu, \pi, k, p.$$

where the information from the muon chambers (MC) is also considered. Pions decaying in flight and punch-through together result in a $\mu - \pi$ misidentification probability of $(2.2 \pm 0.2)\%$ per pion. For $\mu - K$ misidentification the fake rate is $(1.9 \pm 0.5)\%$ per kaon. The fake rates due to $e - \pi$ and $e - K$ misidentification are both $(0.5 \pm 0.1)\%$.

2.13 Monte Carlo Simulation

In order to determine detector efficiencies and resolutions, and to make use of the theoretical models referred to in this thesis, a Monte Carlo simulation of the physics process under study and of the detector performance is required. The Monte Carlo simulation steps are:

- **Event Generation:** The event generator is the source of information about all physical processes involved in e^+e^- collisions. For this work, two event generators were used. B meson pairs from $\Upsilon(4S)$ decays were generated and allowed to decay using the MOPEK (MOntecarlo Program for Event Kinematics) event generator [37], while $c\bar{c}$ pairs from e^+e^- annihilation were generated and allowed to fragment according to the JETSET 7.2 which includes higher excited charmed states or the JETSET 6.3 [38] string fragmentation model.

- **Detector Simulation:** The ARGUS program SIMARG [40] which is based on the CERN GEANT program [41] is used to simulate the response of the detector. All particles in the event record are traced through the detector geometry. Interaction with matter such as multiple scattering, ionization energy loss and photon conversions are included in the simulation. The treatment of electromagnetic interactions basically follows the procedure of the EGS program [42], while the simulation of hadronic processes is performed using GHEISHA [43]. The output of the detector, such as TDC and ADC values, is written in a format identical to that of real data.

- **Event Reconstruction:** Here, the events are processed through the normal reconstruction program and the output is used for subsequent analysis using KAL. In this step the events are treated identically to the data.

A large amount of CPU is required to process events through SIMARG. As an alternative, a less detailed simulation called "MINI-Monte Carlo" is also available. This is sufficient for modeling kinematics and convenient in the sense that very large Monte Carlo samples are possible, in contrast to cpu-limited SIMARG. During this work, whenever the "MINI-MC" was used, single particle momentum-dependent efficiencies were tuned to match the values obtained from detailed Monte Carlo simulation.

2.14 KAL: Kinematical Analysis Language

KAL is a special interpretive language [44] written in FORTRAN 77 and specifically intended to simplify the data analysis in ARGUS. KAL is used to perform particle identity determination, construct invariant mass combinations, calculate kinematical quantities for different systems of particles in different rest frames, carry out kinematical fits to measured particle masses, *etc.* The full event record is converted to a special condensed format for use by the KAL program, thus greatly simplifying the analysis.

Chapter 3

The decay $\bar{B}^0 \to D^{*+}\ell^-\bar{\nu}$

In this chapter a partial reconstruction technique for studying the decay $\bar{B}^0 \to D^{*+}\ell^-\bar{\nu}$ is introduced. This semileptonic decay proceeds via the spectator diagram shown in Figure 3.1 and the semi-exclusive reconstruction technique applied here is described in Section 3.1.

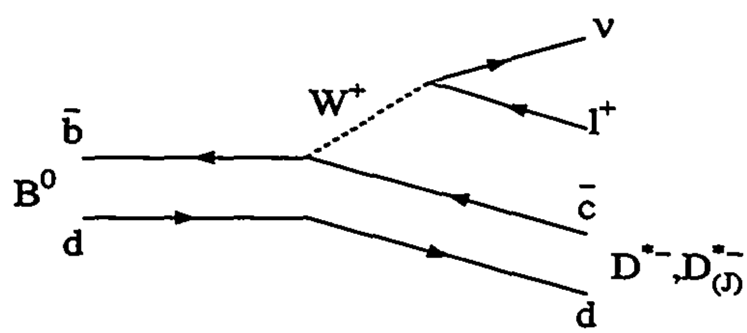

Figure 3.1: Feynman graph for the decay $\bar{B}^0 \to D^{*+}\ell^-\bar{\nu}$.

The standard method requires reconstruction of the D^{*+} candidate which is realized in the $D^{*+} \to D^0\pi^+$ mode. Therefore, due to the low value for $Br \cdot efficiency$ for the D^0 meson, the event samples used for the study of the decay $\bar{B}^0 \to D^{*+}\ell^-\bar{\nu}$ are statistically limited. The technique applied here makes use of the kinematics of the decay $D^{*+} \to D^0\pi^+$, together with the fact that B mesons are produced almost at rest in $\Upsilon(4S)$ decays, to provide a larger statistical sample of $\bar{B}^0 \to D^{*+}\ell^-\bar{\nu}$ events. The lepton from the $\bar{B}^0 \to D^{*+}\ell^-\bar{\nu}$ decay is combined with the slow pion from the decay $D^{*+} \to D^0\pi^+$ to *tag* $\bar{B}^0$ mesons in the decay $\bar{B}^0 \to D^{*+}\ell^-\bar{\nu}$, thus bypassing the low D^0 reconstruction efficiency. Compared to the full reconstruction method, more sources contribute to the background arising from the use of the partial reconstruction technique, thus necessitating a careful background study. This chapter is organized as follows: The method followed is described in Section 3.1. In Sections 3.2 and 3.3 the event selection criteria and the requirements that leptons need to fulfill are given, respectively. The background studies are presented in Section 3.4 where also the branching ratio for this decay is derived. Using the same method, the branching ratio for the process $Br(\bar{B}^0 \to D^{*+}_{(J)}\ \ell^-\bar{\nu})$ is extracted in Section 3.5.

3.1 The "Missing-Mass" Technique

The presence of an undetected neutrino limits the capability for exclusive reconstruction of the semileptonic $\bar{B}^0$ decay $\bar{B}^0 \to D^{*+}\ell^-\bar{\nu}$. However, the exceptionally low momentum of the B mesons produced in $\Upsilon(4S)$ decays offers the possibility to infer the effective neutrino mass from the D^* and ℓ kinematical quantities. The momentum and energy of the B are:

$$\begin{aligned} \vec{p}_B &= \vec{p}_{D^*} + \vec{p}_\ell + \vec{p}_\nu \\ E_B &= E_{D^*} + E_\ell + E_\nu. \end{aligned} \tag{3.1}$$

The neutrino mass is given by:

$$M_\nu^2 \;=\; E_\nu^2 - p_\nu^2 = (E_B - (E_{D^*} + E_\ell))^2 - (\vec{p}_B - (\vec{p}_{D^*} + \vec{p}_\ell))^2 = M^2_{recoil} \tag{3.2}$$

that is, M_ν^2 is the recoil mass M^2_{recoil} against the $D^*\ell$ system in the center of mass of the B-meson. The energy of the B meson is the beam energy E_{beam}. So, we have

$$M^2_{recoil} \;=\; (E_{beam} - E_{D^*} - E_\ell)^2 - |\vec{p}_{D^*} + \vec{p}_\ell|^2 - |\vec{p}_B|^2 + 2\vec{p}_B \cdot (\vec{p}_{D^*} + \vec{p}_\ell). \tag{3.3}$$

This is the square of a quantity referred to as the *missing mass*. The only unknown quantity in the above expression is the direction of motion of the B meson. The B mesons produced in $\Upsilon(4S)$ decays are nearly at rest ($\vec{p}_B$ = 340 MeV/c). This implies that the last two terms in this expression give a very small contribution, so that by approximating $|\vec{p}_B| \sim 0$ the mean value of M^2_{recoil} is not shifted significantly. The experimental resolution in M^2_{recoil} is dominated by the smearing introduced by ignoring the B momentum in equation 3.3. Since the neutrino mass is very small, or zero, we expect that the effective neutrino mass should be consistent with 0,

$$M^2_\nu = (E_{beam} - E_{D^*} - E_\ell)^2 - |\vec{p}_{D^*} + \vec{p}_\ell|^2 = M^2_{recoil} \tag{3.4}$$

that is for D^* ℓ combinations coming from the decay $\bar{B}^0 \rightarrow D^{*+}\ell^-\bar{\nu}$, the M^2_{rec} distribution should peak at zero.

The technique described above was first introduced by ARGUS [50] for measurements of exclusive semileptonic B meson decays and has been used extensively to study the decay $\bar{B}^0 \rightarrow D^{*+}\ell^-\bar{\nu}$ where the D^{*+} is fully reconstructed in its decay mode $D^{*+} \rightarrow D^0\pi^+$. Here this method is carried one step further by tagging the decay $D^{*+} \rightarrow D^0\pi^+$ using only the π^+ without reconstructing the D^0. This approach is conceivable because the energy release in the decay is only about 6 MeV, so the π^+ is nearly at rest in the D^* frame, which implies that the direction of the pion is close to that of the D^* and that their momenta are strongly correlated.

Two different approaches to parametrizing the D^* momentum are used. The first one makes an approximation to the D^* momentum, while the second one makes an approximation to the D^* energy. In both cases the flight direction of the low momentum π is taken as the D^* direction.

A) Using a Monte Carlo simulation study, it was found that the relation between the momenta of the D^* meson and the soft π^+ can be approximated by

$$p_{D^*} = \alpha p_\pi + \beta \tag{3.5}$$

with $\alpha = 8.23$ and $\beta = 0.41$ GeV/c (Figure 3.2).

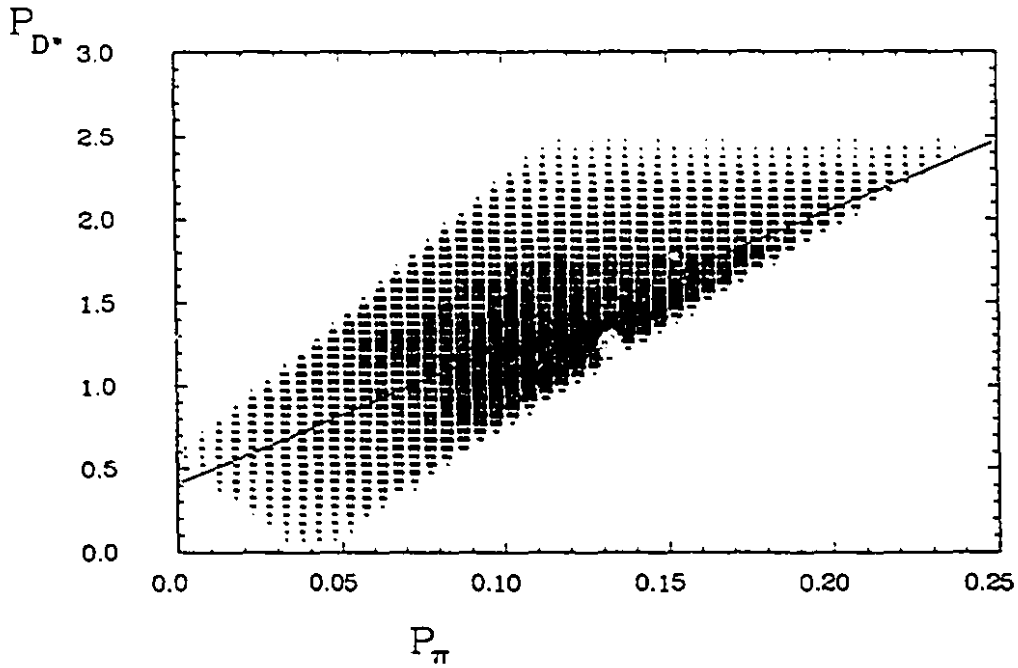

Figure 3.2: Correlation between the D^{*+} and the soft π^+ momenta. The linear relation used to calculate $p_{D^{*+}}$ from p_π is indicated by the solid line.

B) From the kinematics of the decay $D^{*+} \to D^0\pi^+$ the momentum p_π^{CM} of the soft pion in the D^* rest frame is 40 MeV/c. In the lab frame the D^* energy is $E_{D^*} = \gamma m_{D^*}$, and the energy of the π^+ is given by a Lorentz transformation

$$E_\pi = \gamma(E_\pi^{CM} + \beta p_\pi^{CM} cos\theta) \tag{3.6}$$

where θ is the decay angle of the π^+ in the D^{*+} rest frame with respect to the D^{*+} direction in the lab; since the the D^{*+} direction is approximated with the π^+ direction, $cos\theta = 1$. The mean energy of the π^+ in the lab is then γE_π^{CM} where $E_\pi^{CM} = 145$ MeV/c. Substituting $\gamma = \frac{E_\pi}{E_\pi^{CM}}$ in $E_{D^*} = \gamma m_{D^*}$ one gets

$$E_{D^*} = \frac{E_\pi}{E_\pi^{CM}} \cdot m_{D^*}. \tag{3.7}$$

3.2 Event Selection

The event selection criteria are chosen so as to enrich the data sample in $B\bar{B}$ events. For this purpose it is necessary to suppress continuum events as well as beam-gas and beam-wall events, which are events where the beam electrons interact with gas molecules in the storage ring or the beam pipe. The suppression of the last two classes of events is realized by demanding that tracks originate from a certain volume around the nominal interaction point with

$$r \leq 1.5\ cm \quad \text{and} \quad |z| \leq 5.0\ cm$$

where r is the radial distance from the nominal interaction point perpendicular to the beam axis and z the distance along the beam axis. The fact that continuum as well as background events have lower total multiplicities than $B\bar{B}$ events is taken advantage of: requiring that the total multiplicity of the event $N_{total} = N_{ch} + N_{\gamma}/2 \geq 5$, where N_{ch} is the number of charged tracks (originating from the interaction region), results in an efficient suppression of the above mentioned background sources, while $B\bar{B}$ events remain unaffected. Only tracks that point to the main vertex with a $\chi^2 \leq 36$ are considered. All mass hypotheses for each charged track are accepted for which the combined likelihood ratio, determined by dE/dx and TOF measurements (see Section 2.15.4), exceeds 1%. Using the knowledge that continuum events contain tracks with momenta above the limit for decay products of B mesons, the requirement that no track exists in the event with a momentum greater than 3.0 GeV/c is applied.

3.3 Lepton Selection

For the identification of electrons and muons the likelihood functions Lhe and $Lh\mu$ described in Section 2.15.4 are used. For lepton candidates

- $Lhe \geq 0.7$ and $|\cos\theta_e| \leq 0.9$

- $Lh\mu \geq 0.7$ and $|\cos\theta_\mu| \leq 0.9$

are required, where $\cos\theta$ is the angle of the track with respect to the beam direction. For muons, at least one hit in an outer layer of muon chambers is required. Also, for both electrons and muons, the tracks were required to originate from the interaction region with a $\chi^2 < 36$.

Electrons originating from converted photons were rejected by excluding all e^+e^- pairs with invariant mass less than 100 MeV/c^2, as well as e^+e^- pairs from secondary vertices. The χ^2 for forming a secondary vertex was requested to be less than 36.

To estimate the efficiency for leptons to pass the above selection criteria a Monte Carlo simulation was used (Fig.3.3).

There are three semileptonic quark transitions contributing to the resulting lepton sample: $b \to c\,\ell\,\nu$ and $b \to u\,\ell\,\nu$, constituting the primary lepton spectrum, and the cascade lepton component $c \to s\,\ell\,\nu$, as shown in Figure 3.4. Cascade leptons are also referred to as secondary leptons.

To minimize the cascade lepton component and to achieve a reduction of the contribution from continuum events, shown in Figure 3.5, a cut ($1.4 \leq p_\ell \leq 2.5$ GeV/c) is applied to the lepton momentum. The upper cut on the momentum of the lepton is applied to minimize the continuum contribution since the kinematical limit for leptons originating from B decays is 2.5 GeV/c.

3.4 Study of the decay $\bar{B}^0 \to D^{*+}\ell^-\bar{\nu}$

In order to reconstruct D^* mesons,

- every π^+ with momentum less than 200 MeV/c is used as a candidate for D^{*+} , thus incorporating 96% of the pions coming from D^{*+} decays;

- the D^{*+} direction is assumed to coincide with the π^+ direction;

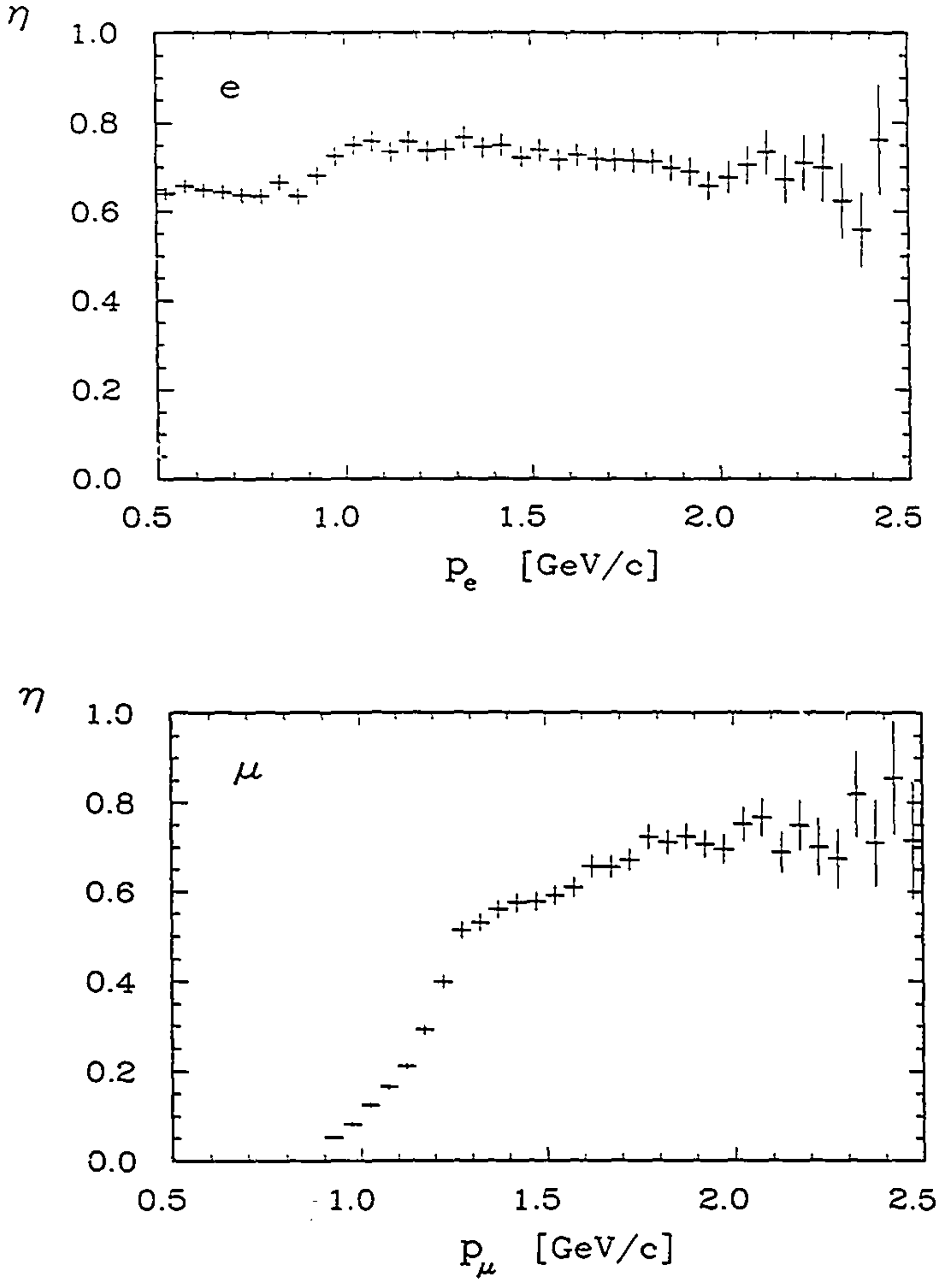

Figure 3.3: Lepton efficiencies obtained from Monte Carlo simulation for the selection criteria mentioned in Section 3.3.

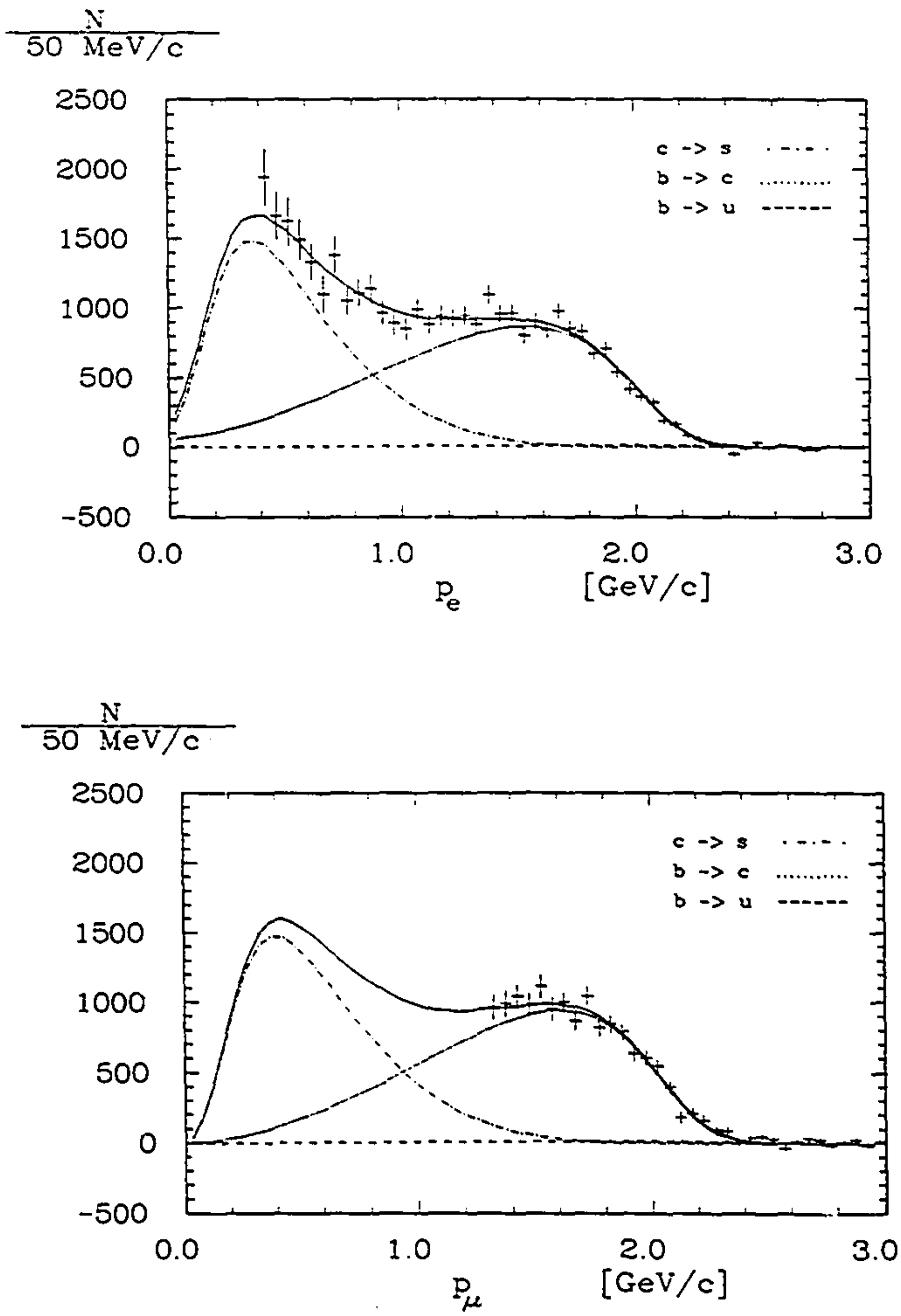

Figure 3.4: Inclusive electron and muon spectra from B-decays (crosses) as taken from [46]. The contribution of primary leptons ($b \to c\,\ell\,\nu$, $b \to u\,\ell\,\nu$) and the contribution of cascade decays of charmed hadrons ($c \to s\,\ell\,\nu$) are also shown.

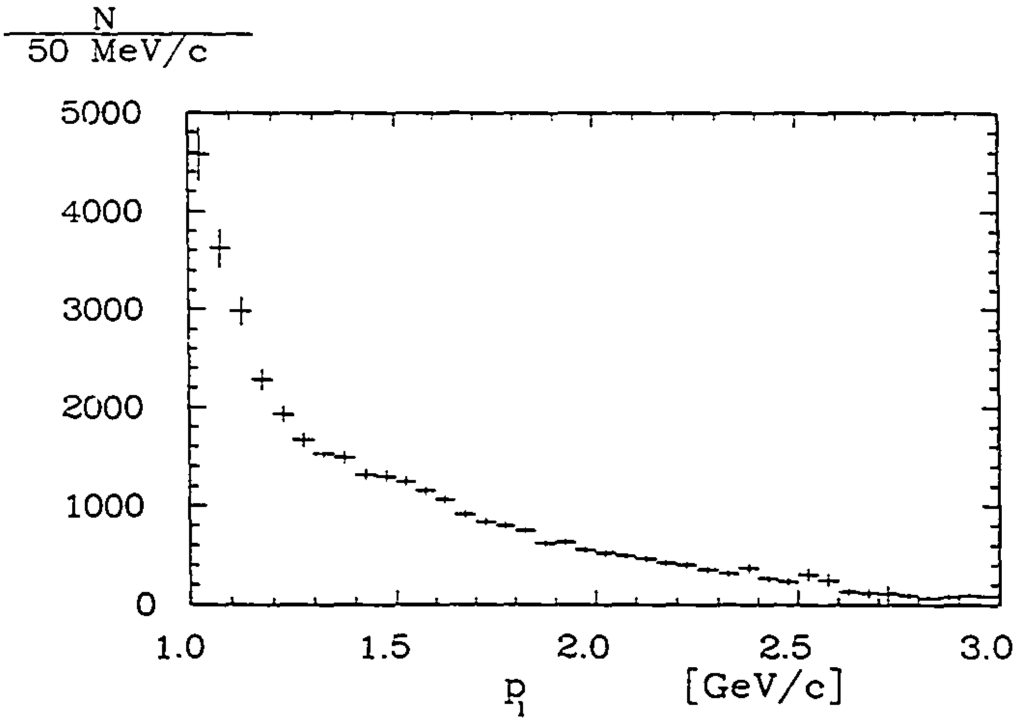

Figure 3.5: Lepton spectrum in the continuum under the $\Upsilon(4S)$.

- the D^{*+} momentum is calculated using parametrizations (A) or (B) described in Section 3.1.

The M^2_{recoil} distribution resulting from a Monte Carlo simulation of the decay $\bar{B}^0 \rightarrow D^{*+}\ell^-\bar{\nu}$ where the D^* further decays to $D^{*+} \rightarrow D^0\pi^+$ based on the IGSW [45] model is shown in Figure 3.6.

The signal can be distinguished from feeddown from the cascade decay

$$\begin{array}{l} \bar{B} \longrightarrow D^{*}_{(J)}\, \ell^- \, \bar{\nu} \\ \qquad\quad \hookrightarrow_{\pi}\, D^{*+}, \end{array}$$

by a positive shift of about 1.0 GeV^2/c^4 in the recoil mass spectrum. The shape of the contribution from this process is also shown in Figure 3.6.

The contribution from continuum events was determined using data collected at centre-of-mass energies below the $B\bar{B}$ production threshold, scaled using a *scaling factor* which takes into account the difference in the cross sections and the collected

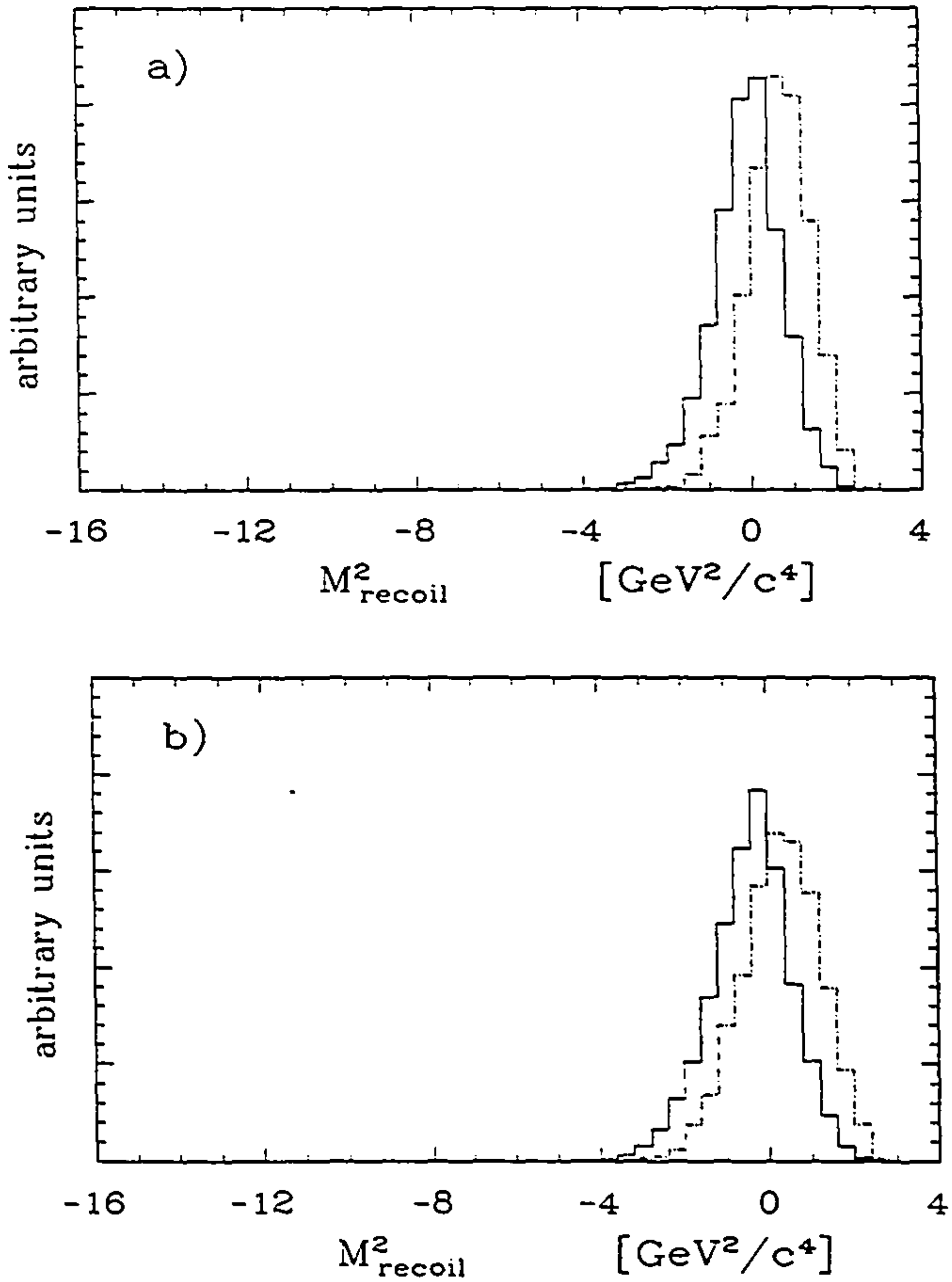

Figure 3.6: M^2_{recoil} spectra for $\bar{B}^0 \rightarrow D^{*+}\ell^-\bar{\nu}$ (histogram) and $B \rightarrow D^*_{(J)}\ell\nu$ (dotted histogram) obtained from Monte Carlo simulation. a) and b) correspond to the parametrizations (A) and (B) respectively. For comparison, the two histograms are normalized to unit area. A clear shift in the recoil mass between the two processes can be observed. In addition, one can see that parametrization (A) has better resolution than parametrization (B).

luminosities. The continuum scaling factor f is:

$$f = \frac{\mathcal{L}_{on}}{\mathcal{L}_{off}} \cdot \frac{s_{off}}{s_{on}} \tag{3.8}$$

where $\mathcal{L}_{on}$ and $\mathcal{L}_{off}$ are the measured time integrated luminosities on and off the $\Upsilon(4S)$ resonance respectively and s_{off} and s_{on} are the corresponding squared center of mass energies. The scaling factor f is found to be $f = 2.40 \pm 0.003$. To account for the different center of mass energies for $\Upsilon(4S)$ and continuum data, the momenta of the tracks measured in the continuum are scaled according to:

$$p_{scaled} = p \cdot \frac{\sqrt{s_{on}}}{\sqrt{s_{off}}}. \tag{3.9}$$

After continuum subtraction, the M^2_{recoil} spectrum shown in Figure 3.7 was obtained for $(\ell^+\pi^-)$ combinations. The prominent peak at $M^2_{recoil} \sim 0$ is attributed to $B \rightarrow D^* \ (\pi) \ \ell \ \nu$ decays. To extract the contribution from the decay chains

$$\begin{array}{lcl} \bar{B}^0 \longrightarrow D^{*+} \ \ell^- \ \bar{\nu} & \quad\text{and}\quad & \bar{B} \longrightarrow D^*_{(J)} \ \ell^- \ \bar{\nu} \\ \quad\; \hookrightarrow \pi^+ \ D^0 & & \quad\; \hookrightarrow \pi \ D^{*+} \\ & & \qquad\quad \hookrightarrow \pi^+ \ D^0 \end{array}$$

to the recoil mass spectrum, the corresponding M^2_{recoil} spectrum arising from uncorrelated lepton-pion combinations, which constitute the main source of background, needs to be studied. The M^2_{recoil} spectrum obtained for wrong-sign $(\ell^+\pi^+)$ combinations is used to describe this background.

The shapes of the spectra for right- and wrong-sign $\ell\pi$ combinations are well reproduced by a Monte Carlo simulation of $\Upsilon(4S) \rightarrow B\bar{B}$ events. Moreover, the shape of the background for the right-sign combinations is the same as that for the wrong-sign, with a well reproduced relative normalization (Fig. 3.8). This means that the pion is generally soft enough so as not to have a strong correlation with the lepton, as assumed, and that this correlation is charge independent.

The spectrum was fit using the shape of the background provided by the wrong-sign $(\ell^+\pi^+)$ combinations as derived from the data, and contributions from both the

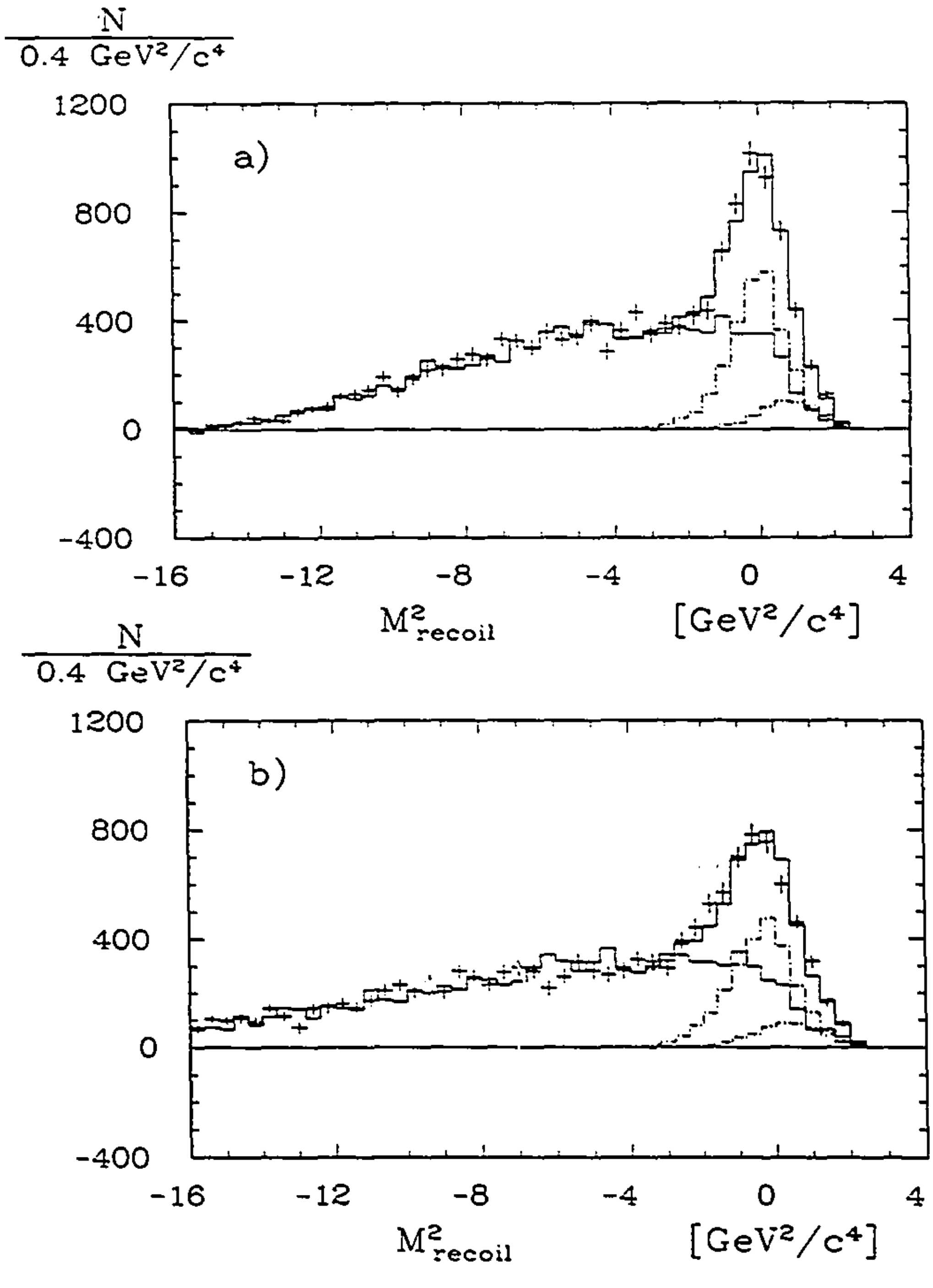

Figure 3.7: M^2_{recoil} spectra for right-sign $\ell - \pi$ combinations (points with error bars), wrong-sign $\ell - \pi$ combinations (dotted histogram) and the result of the fit (histogram). Also shown are the $\bar{B}^0 \to D^{*+}\ell^-\bar{\nu}$ and $B \to D^*_{(J)}\ell\nu$ contributions determined from the fit (dashed-dotted histograms). a) corresponds to parametrization (A) and b) to parametrization (B). The expected continuum contribution has been subtracted.

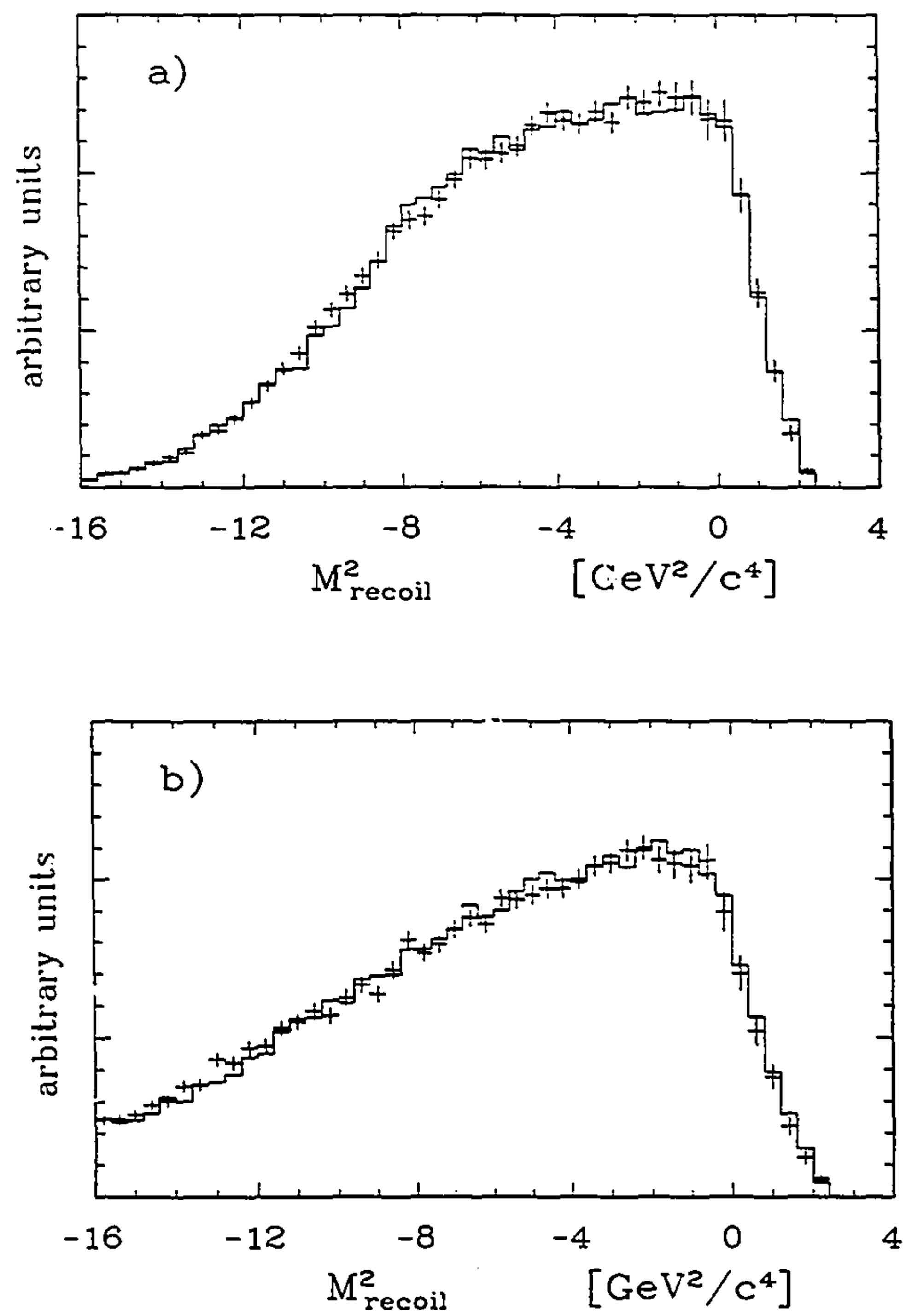

Figure 3.8: M^2_{recoil} spectra for uncorrelated right-sign $\ell - \pi$ combinations (points with error bars) and wrong-sign $\ell - \pi$ combinations (histogram) obtained from Monte Carlo simulation. a) and b) correspond to the M^2_{recoil} spectra obtained using parametrizations (A) and (B) respectively.

D^{*+} and $D^*_{(J)}$ channels (Fig. 3.7). The expected shapes of these last two contributions to the M^2_{recoil} distribution were derived from a Monte Carlo simulation based on the IGSW model [45] since this is so far the only model in which $B \to D^*_{(J)}\ell\nu$ decays are calculated.

From the fit

$$\begin{aligned} N_{D^*} &= 2705 \pm 162 \\ N_{D^*_{(J)}} &= 476 \pm 107 \end{aligned} \tag{3.10}$$

were found using parametrization (A) and

$$\begin{aligned} N_{D^*} &= 2466 \pm 171 \\ N_{D^*_{(J)}} &= 520 \pm 123 \end{aligned} \tag{3.11}$$

using parametrization (B).

Correlated background, that is D^*-lepton events in which the lepton and the D^* come from the same B meson decay, arises from the processes:

$$\begin{aligned} \bar{B}^0 &\longrightarrow D^{*+}\,\tau^-\,\bar{\nu}_\tau \\ &\qquad\qquad \hookrightarrow \ell^-\,\nu_\tau\,\bar{\nu} \end{aligned} \tag{3.12}$$

$$\begin{aligned} \bar{B}^0 &\longrightarrow D^{*+}D_s^{(*)-} \\ &\qquad\qquad \hookrightarrow (D_s^-\gamma) \\ &\qquad\qquad\qquad \hookrightarrow \ell^-\bar{\nu}\,(X) \end{aligned} \tag{3.13}$$

Using the value $\bar{B}^0 \to D^{*+}\tau^-\bar{\nu}_\tau = 1.2\%$ [62] and a Monte Carlo simulation, the contribution of this decay mode was estimated to be 19.2 ± 1.6 events. The corresponding recoil mass spectrum for $(\pi^\mp - \ell^\pm)$ combinations is shown in Figure 3.9. Since the M^2_{recoil} distribution is clearly shifted to positive values, this source contributes mainly to the $D^*_{(J)}$ yield and does not affect the D^{*+} signal.

The same holds for background arising from $\bar{B}^0 \longrightarrow D^{*+}D_s^{(*)-}$. For semileptonic decays of the D_s, only the branching ratio for $D_s^- \to \phi\,\ell^-\bar{\nu}$ is measured experimentally. Taking the value $Br(D_s^- \to \phi\,\ell^-\,\bar{\nu}) = (3.2 \pm 1.4)\%$ [51], the branching ratios for $D_s^- \to \eta\,\ell^-\bar{\nu}$ and $D_s^- \to \eta'\,\ell^-\bar{\nu}$, where ℓ is an electron or a muon, can be

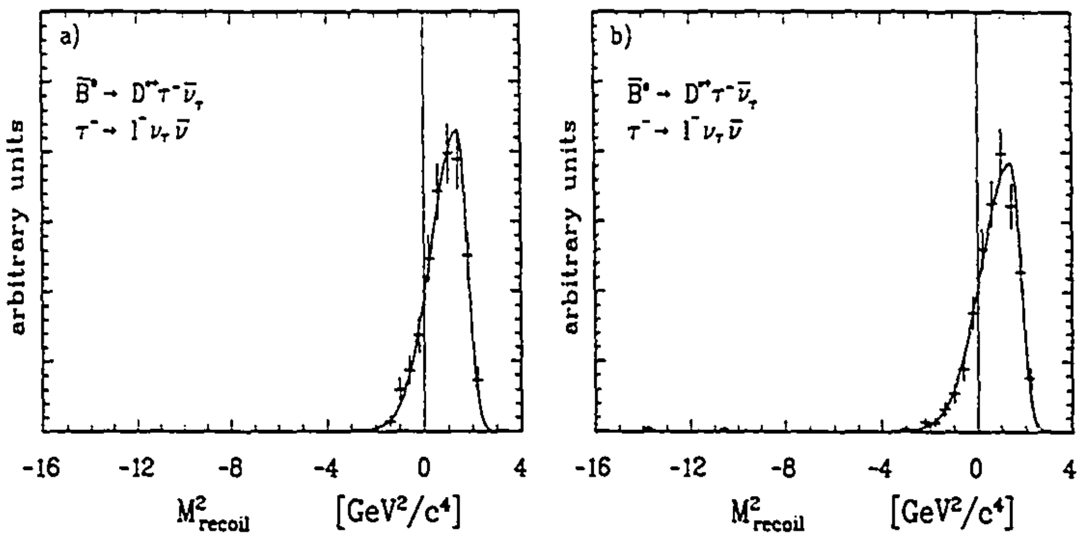

Figure 3.9: M^2_{recoil} distribution for $(\pi^\mp - \ell^\pm)$ combinations arising from the decay process $\bar{B}^0 \to D^{*+}\tau^-\bar{\nu}_\tau$ obtained from Monte Carlo simulation. a) and b) correspond to parametrizations (A) and (B) respectively.

determined via the BSW Model and used to estimate the ratio of widths for these three D_s semileptonic processes:

$$\Gamma(D_s^- \to \phi\, \ell^-\bar{\nu}) : \Gamma(D_s^- \to \eta\, \ell^-\bar{\nu}) : \Gamma(D_s^- \to \eta'\, \ell^-\bar{\nu}) = 12 : 15 : 4. \qquad (3.14)$$

The values obtained are shown in Table 3.1.

	decay channel	Branching ratio
I	$D_s^- \to \phi\, \ell^-\bar{\nu}$	$(3.2 \pm 1.4)\%$
II	$D_s^- \to \eta\, \ell^-\bar{\nu}$	$(4.0 \pm 1.7)\%$
III	$D_s^- \to \eta'\, \ell^-\bar{\nu}$	$(1.1 \pm 0.5)\%$

Table 3.1: Values considered for the different D_s semileptonic branching ratios.

The D_s daughter lepton momentum distributions for these channels are shown in Figure 3.10. Since the lepton momentum is required to be greater than 1.4 GeV/c,

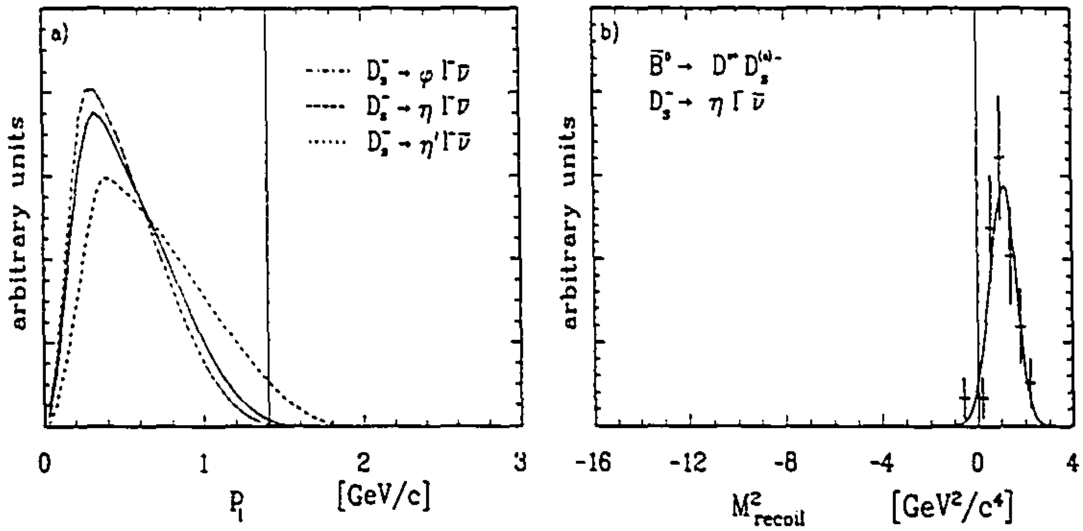

Figure 3.10: a) Lepton momentum distributions for the various D_s decays, and b) Monte Carlo provided M^2_{recoil} distribution for $(\pi^{\mp} - \ell^{\pm})$ combinations arising from the decay channel $D_s^- \to \eta\, \ell^- \bar{\nu}$. The vertical line represents the cut imposed on the lepton momentum.

only the decay $D_s^- \to \eta\, \ell^- \bar{\nu}$ is expected to contribute to the background. The background recoil mass spectrum is shown in Figure 3.10.

The sum of the branching ratios for the processes $\bar{B}^0 \to D^{*+}D_s^-$ and $\bar{B}^0 \to D^{*+}\, D_s^{*-}$ is measured by the ARGUS and the CLEO Collaborations to be $(4.0 \pm 1.8)\%$ [52], [22] and $(5.6 \pm 2.2)\%$ [53] respectively. The weighted average of these measurements, $Br(\bar{B}^0 \to D^{*+}D_s^{(*)+}) = (4.6 \pm 1.4)\%$ is further used to extract the contribution from this background source. The number of events obtained is 4.1 ± 2.2 events. As before, the background is subtracted from the $D^*_{(J)}$ yield given by the fit. Finally, background arising from purely leptonic D_s decays should be considered. Taking

$$\frac{\Gamma(D_s^- \to \mu^-\bar{\nu})}{\Gamma(D_s^- \to \phi\, \pi^-)} = 0.245 \pm 0.052 \pm 0.074, \tag{3.15}$$

from [54], and $Br(D_s^- \to \phi\, \pi^-) =$ (2.8±0.5)% [2], the value for the $Br(D_s^- \to \mu^-\bar{\nu}_\mu)$ shown in Table 3.2 is obtained. To estimate $Br(D_s^- \to \tau^-\bar{\nu}_\tau)$ the following formula

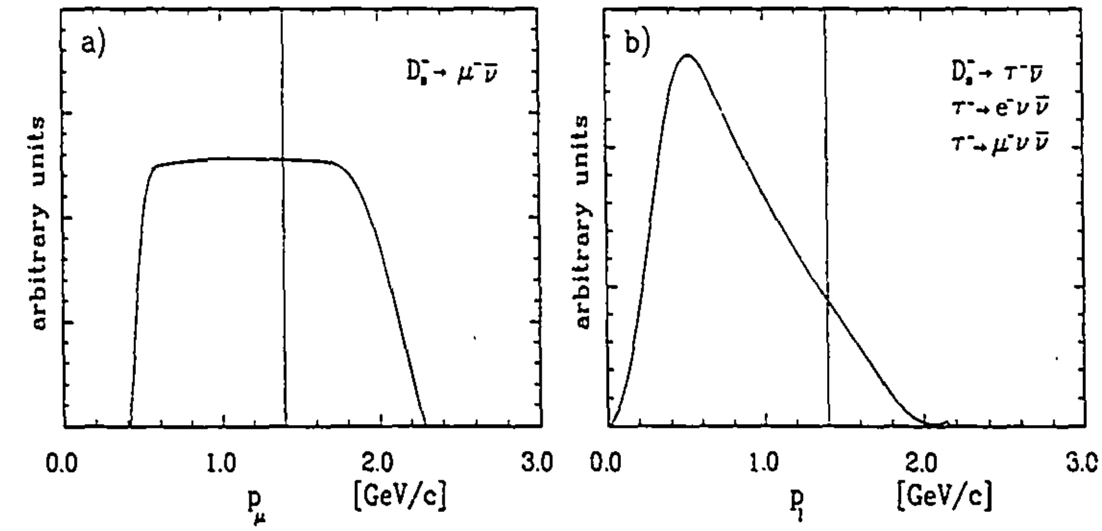

Figure 3.11: Lepton momentum distributions for the D_s decays $D_s^- \to \mu^- \ \bar{\nu}_\mu$ (a), and $D_s^- \to \tau^-(\to e^-/\mu^-\nu\bar{\nu})\ \bar{\nu}_\tau$ (b).

is used.

$$\Gamma(D_s^- \to \ell^-\bar{\nu}) = \frac{1}{8\pi} G_F^2 f_{D_s}^2 m_\ell^2 M_{D_s} (1 - \frac{m_\ell^2}{M_{D_s}^2})^2 |V_{cs}|^2. \tag{3.16}$$

Therefore,

$$\frac{\Gamma(D_s^- \to \tau^-\bar{\nu}_\tau)}{\Gamma(D_s^- \to \mu^-\bar{\nu}_\mu)} = \frac{m_\tau^2}{m_\mu^2} \cdot \frac{(1 - \frac{m_\tau^2}{M_{D_s}^2})^2}{(1 - \frac{m_\mu^2}{M_{D_s}^2})^2} \tag{3.17}$$

	decay channel	Branching ratio
IV	$D_s^- \to \mu^-\bar{\nu}_\mu$	$(0.69 \pm 0.28)\%$
V	$D_s^- \to \tau^-(\to e^-/\mu^-\nu\bar{\nu})\bar{\nu}_\tau$	$(6.29 \pm 2.55)\% \times (35.51 \pm 0.37)\%$

Table 3.2: Values considered for the different D_s leptonic branching ratios.

The purely leptonic branching ratios of the D_s are shown in Table 3.2. The momentum distributions of the D_s daughter leptons for the two leptonic decays are shown in Figure 3.11; while the recoil mass spectra are shown in Figure 3.12.

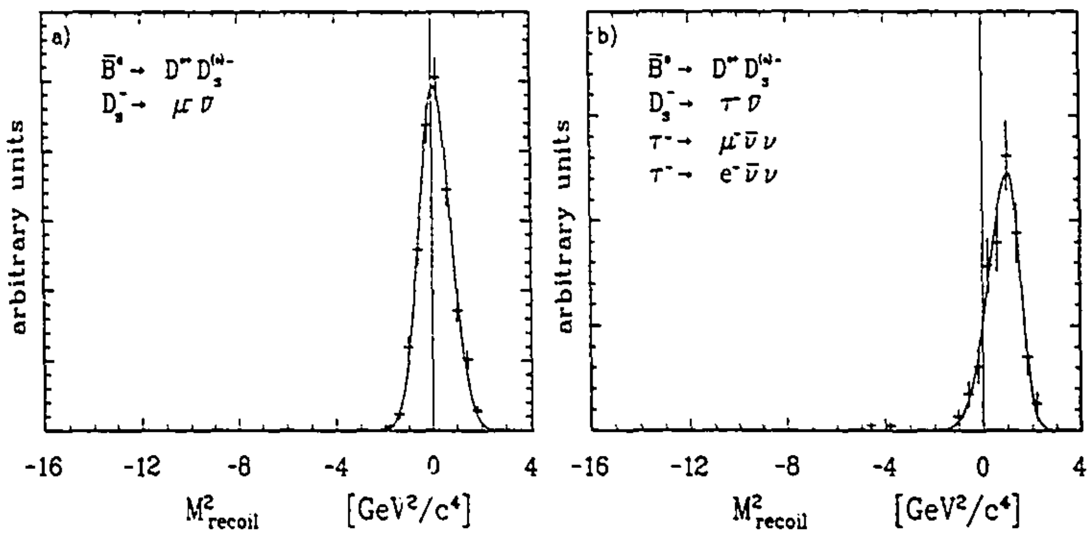

Figure 3.12: M^2_{recoil} distributions for the $(\pi^\mp - \ell^\pm)$ combinations arising from the decay channels $D_s^- \to \mu^-\bar{\nu}_\mu$ (a), and $D_s^- \to \tau^-(\to e^-/\mu^-\nu\bar{\nu})\ \bar{\nu}_\tau$ (b).

Using the branching ratios quoted in Table 3.2, process IV is found to contribute 8.8 ± 4.5 events to the background; while process V is found to contribute 7.1 ± 3.6 events. Considering the shape of the recoil mass spectrum shown in Figure 3.12 for $(\pi^\mp - \ell^\pm)$ combinations arising from these decay channels, the background coming from process IV is subtracted from the D^{*+} yield, whereas the background coming from process V is subtracted from the $D^*_{(J)}$ yield.

It is also possible to have correlated background from a combination of a D^* and a fake lepton (misidentified hadron) which are the daughters of the same B meson. (The contribution from fake leptons where the D^* and the lepton are uncorrelated is already taken into account using the wrong-sign lepton-pion combinations). The number of fakes contributing to this background was estimated by performing the same analysis using π-hadron combinations where the fast hadron is not identified as a lepton and scaling by the appropriate momentum dependent misidentification probability per hadron. To determine the hadron misidentification probability, data collected on the $\Upsilon(1S)$ resonance are used. The $\Upsilon(1S)$ resonance decays predominantly into hadrons via $\Upsilon(1S) \to ggg$, and thus comprises a lepton free data sample. Applying the same selection criteria as for the lepton sample from the $\Upsilon(4S)$ resonance, the momentum distribution of the misidentified hadrons is obtained. After continuum subtraction in the $\Upsilon(1S)$ data, the misidentification probability (or *fake rate*) is found when dividing by the momentum distribution of all hadrons in the $\Upsilon(1S)$ data. The fake rate was estimated to be $0.5 \pm 0.1\%$ for electrons and $1.5 \pm 0.15\%$ for muons and is shown in Figure 3.13.

By this means, the background due to fake leptons was found to be 6 ± 3 using parametrization (A) and 5 ± 2 events using parametrization (B). These numbers were obtained by fitting the recoil mass spectra for $(\pi^{\mp} - h^{\pm})$ combinations when the M^2_{recoil} spectrum for $(\pi^{\mp} - h^{\mp})$ combinations is considered for the background parametrization. Taking the momentum dependence of hadrons in $(\pi - h)$ combinations into account, the number of fakes obtained is 5 ± 4 events using parametrization (A) and 4 ± 3 events using parametrization (B). The difference between the numbers obtained with these two methods is taken into account when estimating the systematic error. The fake lepton contribution was subtracted from the yields mentioned above.

The above mentioned background sources should be subtracted from the number of events N_{D^*} and $N_{D^*_{(J)}}$ obtained from the fit. The resulting yields are:

$$\begin{aligned} N_{D^*} &= 2690 \pm 162 \\ N_{D^*_{(J)}} &= 445 \pm 107 \end{aligned} \tag{3.18}$$

using parametrization (A) and

$$\begin{aligned} N_{D^*} &= 2453 \pm 172 \\ N_{D^*_{(J)}} &= 490 \pm 123 \end{aligned} \tag{3.19}$$

using parametrization (B).

Fitting the recoil mass distribution in bins of lepton momentum allows the extraction of the lepton momentum spectra for each subprocess. Once again, the fit is performed using the shape of the background provided by the wrong-sign $(\ell^+\pi^+)$ combinations for the same lepton momentum intervals, and the contributions from

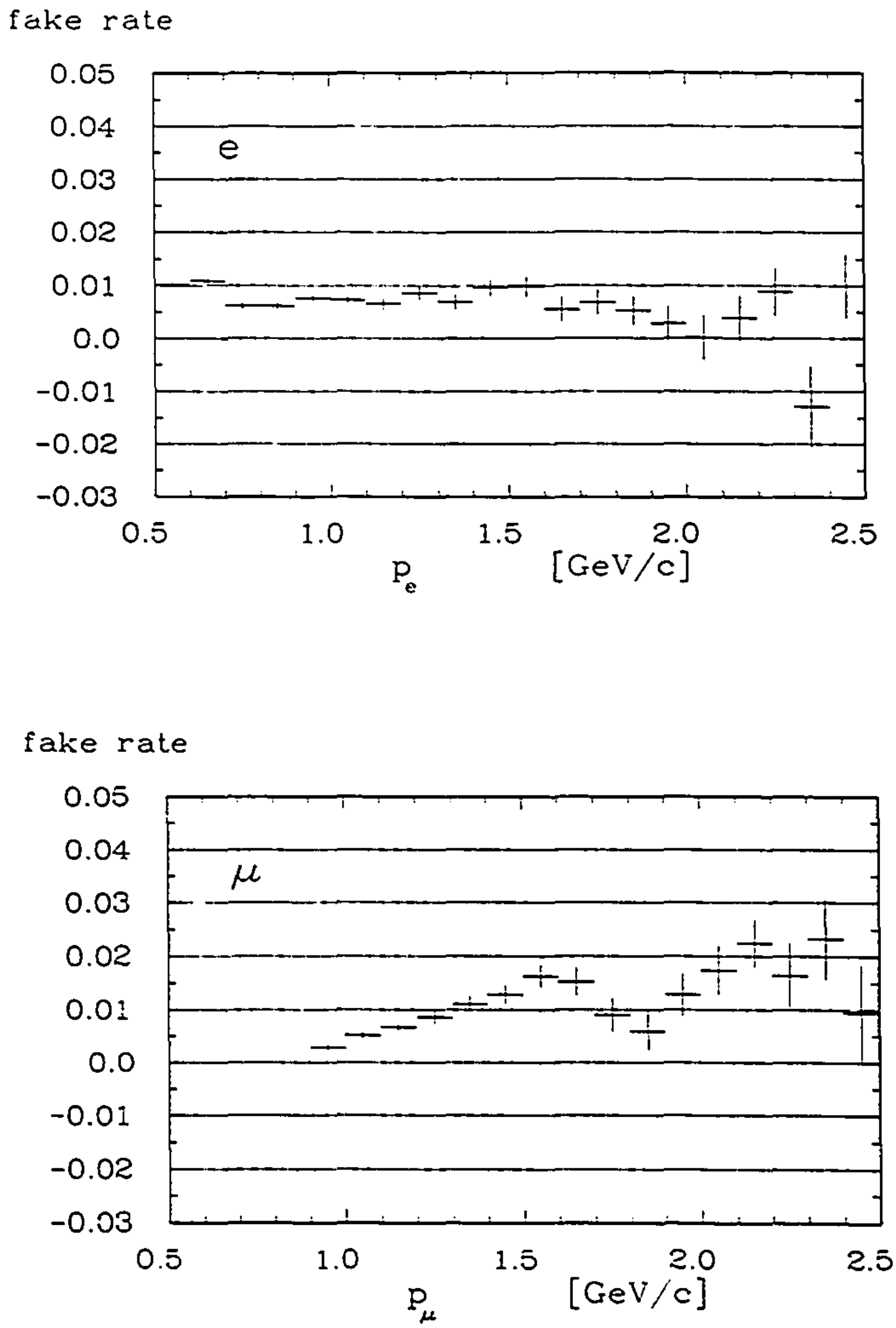

Figure 3.13: Fake rate for electrons and muons as a function of the momentum.

both the D^{*+} and $D^{*}_{(J)}$ channels as taken from a Monte Carlo based on the IGSW model [45]. For the extraction of the lepton spectra the $D^{*}_{(J)}$ was taken as a pure $^3P_1$ state. The resulting distributions are then divided by the lepton efficiency to give the desired lepton momentum spectra. In order to improve the statistical significance, the fits are performed for electrons and muons together. The spectra obtained, as well as the ones expected according to the IGSW model, are shown in Figure 3.14.

The acceptance was obtained from a Monte Carlo simulation using the IGSW model [45]. The overall efficiency η was determined to be 0.215 ± 0.011 for parametrization (A), and 0.199 ± 0.012 for parametrization (B). The branching ratio for the process $\bar{B}^0 \to D^{*+}\ell^-\bar{\nu}$ is:

$$Br(\bar{B}^0 \to D^{*+}\ell^-\bar{\nu}) = \frac{N_{D^{*+}}}{N_{B^0}\cdot \ Br(D^{*+} \to D^0\pi^+)\cdot \ \eta} \tag{3.20}$$

The number of $B\bar{B}$ pairs for the data sample used for this analysis is 209000 ± 9500. The error is dominated by the uncertainty in the ratio of luminosities for the $\Upsilon(4S)$ and the continuum data, which is 1.7% [47]. Assuming the branching ratios of the $\Upsilon(4S)$ to charged and neutral B mesons to be equal $f = \frac{f_{+-}}{f_{00}} = 1.0$, the number of neutral B mesons is $N_{B^0} = 209000 \pm 9500$. Using the CLEO measurement [55] of

$$Br(D^{*+} \to D^0\ \pi^+) = (68.1\ \pm 1.0\ \pm 1.3)\%$$

the branching ratio obtained is:

$$Br(\bar{B}^0 \to D^{*+}\ell^-\bar{\nu}) = (4.40 \pm 0.26)\% \quad \text{where} \quad \ell = e \text{ or } \mu$$

using parametrization (A) and

$$Br(\bar{B}^0 \to D^{*+}\ell^-\bar{\nu}) = (4.33 \pm 0.30)\% \quad \text{where} \quad \ell = e \text{ or } \mu$$

using parametrization (B).

3.4.1 Systematic errors

To study the systematic error:

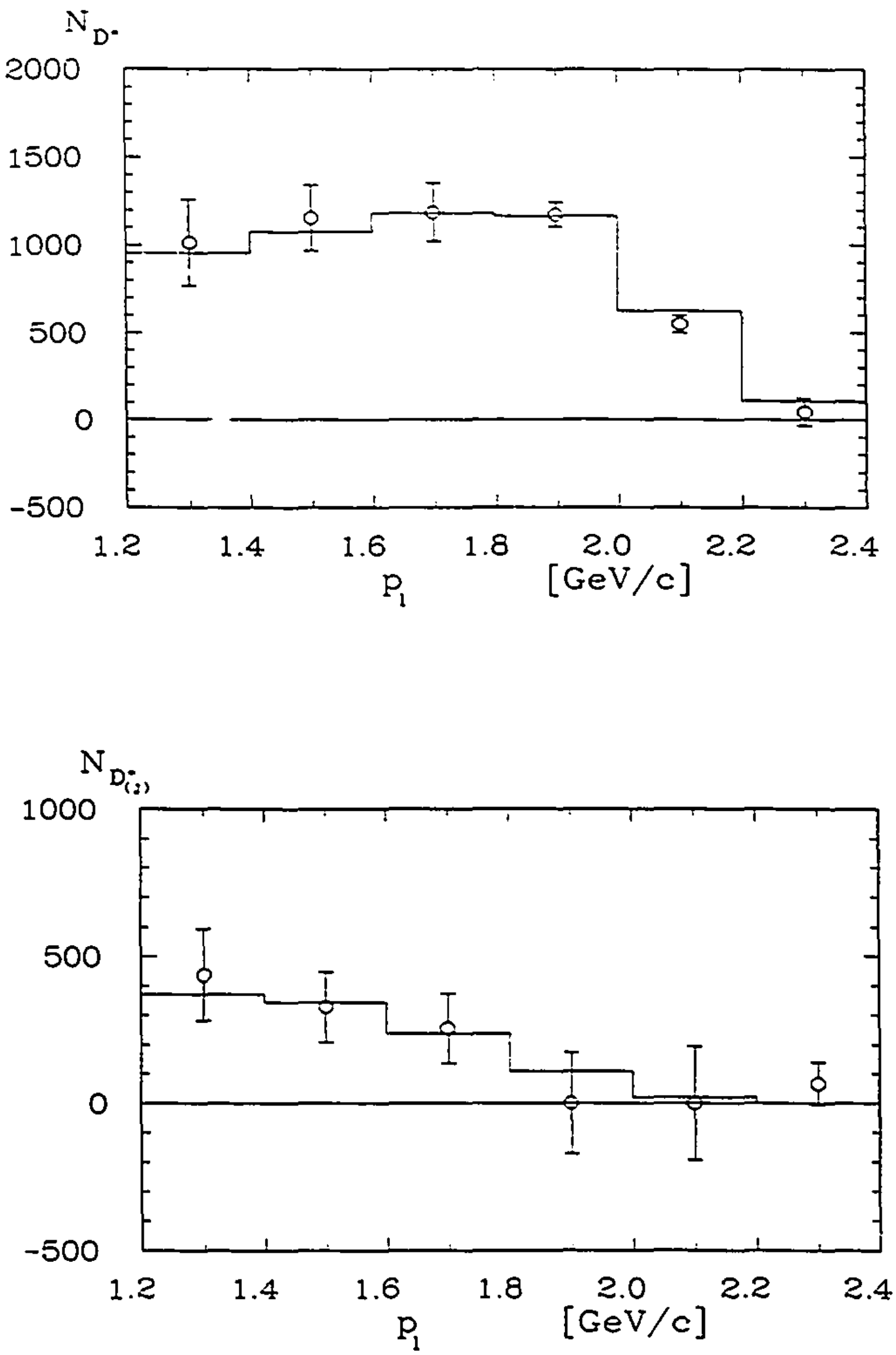

Figure 3.14: Lepton momentum spectra extracted by fitting the recoil mass distribution in bins of the lepton momentum (points with error bars), compared to the IGSW model expectations (histogram).

cut applied	systematic error
slow pion momentum	0.10%
lepton identification	0.05%
background estimation and fitting procedure	0.23%
number of B mesons	0.2%
scaling factor for the continuum subtraction	$< 0.01\%$
error on $Br(D^{*+} \rightarrow D^0\pi^+)$	0.1%
total	0.34%

Table 3.3: Sytematic errors for the study of the decay $\bar{B}^0 \rightarrow D^{*+}\ell^-\bar{\nu}$.

- The cut on the momentum of the slow pion used to tag the $D^{*+} \rightarrow D^0\pi^+$ decay was varied. The influence of this variation constitutes an additional 0.1% to the systematic error.

- To study the uncertainty on the lepton identification in ARGUS, radiative Bhabha events were used as an electron sample, while for muons cosmic-ray muon events were used. A comparison of the resulting efficiencies with the ones obtained from a Monte Carlo simulation was then made. This contribution to the systematic error was found to be 0.05% for electron and 0.04% for muon identification [61].

- The background estimation and the fitting procedure used in this analysis lead to an additional systematic error of 0.23%.

- Introducing the uncertainties on the number of B^0 mesons, on the scaling factor for the continuum subtraction and on the measured branching ratio for the $D^{*+} \rightarrow D^0\pi^+$ decay, another 0.22% should be added to the systematic error.

$Br(\bar{B}^0 \to D^{*+}\ell^-\bar{\nu})$	Branching ratio
$(5.2 \pm 0.5 \pm 0.6)\%$	ARGUS [58]
$(4.6 \pm 0.5 \pm 0.7)\%$	CLEO [60]
$(4.4 \pm 0.3 \pm 0.3 \pm 0.3)\%$	this measurement

Table 3.4: Comparison of the value obtained for $Br(\bar{B}^0 \to D^{*+}\ell^-\bar{\nu})$ with previous ARGUS and CLEO results.

To estimate the systematic uncertainty introduced by the use of a particular theoretical model for the description of the decay $\bar{B}^0 \to D^{*+}\ell^-\bar{\nu}$

- a variation of the value of the D^{*+} polarization within measurement errors was performed.
- the decay $\bar{B}^0 \to D^{*+}\ell^-\bar{\nu}$ was simulated using the BSW [48] and the KS [49] models.

These resulted in an additional systematic error of 0.25% and 0.76% for the $Br(\bar{B}^0 \to D^{*+}\ell^-\bar{\nu})$ and 0.06 and 0.09 for the $\frac{D^{**}}{D^*}$ ratio, when making use of parametrization (A) or (B) respectively.

The value obtained for the branching ratio is therefore:

$$Br(\bar{B}^0 \to D^{*+}\ell^-\bar{\nu}) = (4.40 \pm 0.26\ (\mathrm{stat}) \pm 0.34\ (\mathrm{sys}) \pm 0.25\ (\mathrm{model}))\%$$

using parametrization (A) and

$$Br(\bar{B}^0 \to D^{*+}\ell^-\bar{\nu}) = (4.33 \pm 0.30\ (\mathrm{stat}) \pm 0.34\ (\mathrm{sys}) \pm 0.76\ (\mathrm{model}))\%$$

using parametrization (B).

The result is in good agreement with previous measurements by ARGUS [58], [59] and CLEO [60].

3.5 $Br(\bar{B}^0 \rightarrow D^{*+}_{(J)} \ \ell^-\bar{\nu})$

The branching ratio for the process

$$\bar{B}^0 \longrightarrow D^{*+}_{(J)} \ \ell^- \ \bar{\nu}$$
$$\hookrightarrow D^{*+} \ \pi^0$$

is given by:

$$Br(\bar{B}^0 \rightarrow D^{*+}_{(J)} \ \ell^-\bar{\nu}) = \frac{\frac{1}{3} N_{D^*_{(J)}}}{N_{B^0} \cdot \ Br(D^{*+} \rightarrow D^0\pi^+) \cdot \ \epsilon_{D^*_{(J)}}} \tag{3.21}$$

where $\epsilon_{D^*_{(J)}}$ is:

$$\epsilon_{D^*_{(J)}} = \sum_i \frac{Br(\bar{B}^0 \rightarrow D_i^{**+}\ell^-\bar{\nu})}{Br(\bar{B}^0 \rightarrow D^{**+}\ell^-\bar{\nu})} \cdot Br(D_i^{**+} \rightarrow D^{*+}\pi^0) \cdot \eta_i. \tag{3.22}$$

To extract the last expression for $\epsilon_{D^*_{(J)}}$, the following assumptions have been made.

- $f = \frac{f_{+-}}{f_{00}} = \frac{N_{B^-}}{N_{B^0}} = 1.$
- $2 \cdot Br(\bar{B}^0 \rightarrow D^{**+}\ell^-\bar{\nu}) \cdot Br(D^{**+} \rightarrow D^{*+}\pi^0) = Br(B^- \rightarrow D^{**0}\ell^-\bar{\nu}) \cdot Br(D^{**0} \rightarrow D^{*+}\pi^-)$

The last relation follows from isospin conservation and is responsible for the factor 1/3 in the numerator of equation 3.21. The additional assumption that the decay $D^{**} \rightarrow D^{*+}X$ is saturated with $X = \pi^0/\pi^-$ is made, thus neglecting radiative and multi-pion decays of the D^{**} mesons. To obtain $\epsilon_{D^*_{(J)}}$, a theoretical model must be used to determine the production fractions of the different $D^*_{(J)}$ modes, $\frac{Br(B^0 \rightarrow D_i^{**+}\ell^-\bar{\nu})}{Br(B^0 \rightarrow D^{**+}\ell^-\bar{\nu})}$, and to extract the efficiencies η_i. The GISW model was employed for this purpose as in [58], and the resulting values are shown in Table 3.5.
Inserting the values shown in Table 3.5 in equation 3.22, $\epsilon_{D^*_{(J)}}$ is calculated to be $\epsilon_{D^*_{(J)}} = 0.021$.

Substituting $\epsilon_{D^*_{(J)}}$ in equation 3.21, the value obtained for the branching ratio is:

$$Br(\bar{B}^0 \rightarrow D^{*+}_{(J)} \ \ell^-\bar{\nu}) = (2.46 \pm 0.59)\% \quad \text{where } \ell = e \text{ or } \mu$$

i	type of $D^*_{(J)}$	$\frac{Br(\bar{B}^0 \to D_i^{**+}\ell^-\bar{\nu})}{Br(\bar{B}^0 \to D^{**+}\ell^-\bar{\nu})}$ GISW	$Br(D_i^{**+} \to D^{*+}\pi^0)$	η GISW
1	$D(1^1P_1)$	0.41	$1 \times 1/3$	0.090
2	$D(1^3P_0)$	0.11	$0 \times 1/3$	0.000
3	$D(1^3P_1)$	0.21	$1 \times 1/3$	0.052
4	$D(1^3P_2)$	0.14	$1/4 \times 1/3$	0.115
5	$D(2^1S_0)$	0.07	$1 \times 1/3$	0.090
6	$D(2^3S_1)$	0.06	$3/4 \times 1/3$	0.126

Table 3.5: Values considered for the estimation of $\epsilon_{D^*_{(J)}}$

cut applied	systematic error
slow pion momentum	0.06%
lepton identification	0.03%
background estimation and fitting procedure	0.37%
number of B mesons	0.11%
scaling factor for the continuum subtraction	$< 0.01\%$
error on $Br(D^{*+} \to D^0\pi^+)$	0.06%
variation of the D^{*+} polarization	0.33%
total	0.52%

Table 3.6: Systematic errors for the study of the decay $\bar{B}^0 \to D^{*+}_{(J)}\ \ell^-\bar{\nu}$.

using parametrization (A) and

$$Br(\bar{B}^0 \rightarrow D^{*+}_{(J)}\ \ell^-\bar{\nu}) = (2.70 \pm 0.68)\% \quad \text{where} \ \ \ell = e \text{ or } \mu$$

using parametrization (B). All sources of systematic error considered for the study of the $Br(\bar{B}^0 \rightarrow D^{*+}\ell^-\bar{\nu})$ were taken into account for this study as well and are summarized in Table 3.6. In addition, variation of the D^{*+} polarization value introduces a systematic error of 0.33%.

The value obtained for the branching ratio is therefore:

$$Br(\bar{B}^0 \rightarrow D^{*+}_{(J)}\ \ell^-\bar{\nu}) = (2.46 \pm 0.59 \text{ (stat)} \pm 0.52 \text{ (sys)})\% \quad \text{where} \ \ \ell = e \text{ or } \mu$$

using parametrization (A) and

$$Br(\bar{B}^0 \rightarrow D^{*+}_{(J)}\ \ell^-\bar{\nu}) = (2.70 \pm 0.68 \text{ (stat)} \pm 0.50 \text{ (sys)})\% \quad \text{where} \ \ \ell = e \text{ or } \mu$$

using parametrization (B).

Chapter 4

$B^0\bar{B}^0$ mixing using partial D^{*+} reconstruction

In this chapter further use of the partial reconstruction technique introduced in Section 3.1 is made. An approach which was first applied by the ARGUS Collaboration, and has since been extensively used for studies of $B^0\bar{B}^0$ mixing, is to reconstruct one of the B mesons in the $\bar{B}^0 \to D^{*+}\ell^-\bar{\nu}$ decay mode using the *missing mass* technique described in Section 3.1, and then *tag* the other B meson using the charge of a fast lepton. Unlike the dilepton analysis, which tags the flavour content of both B mesons using the charge of their daughter leptons from the decay $\bar{B} \to X\ell^-\bar{\nu}$, this method provides a result which is independent of $\lambda = b_+^2 f_+/b_0^2 f_0$. Here, f^+ (f^0) is the branching ratio for $\Upsilon(4S)$ decaying into charged (neutral) B mesons and b_+ (b_0) the semileptonic branching ratio of charged (neutral) B mesons, and λ enters the calculation of the mixing parameter to account for the number of dileptons coming from the decay of charged B mesons. An attempt is made here to apply the same principle and at the same time have the advantage of working with a larger statistical sample. Making use of the partial D^{*+} reconstruction technique, the statistical significance of the result should increase, with the advantages of using full reconstruction remaining available. It is expected that in this analysis the background cannot be as clean as for the D^{*+} in the decay $\bar{B}^0 \to D^{*+}\ell^-\bar{\nu}$ [71]. It is shown in

Section 4.1 however, that an efficient description of the background can be made, thus making possible the determination of the mixing parameter.

The results presented in the following analysis have been obtained using only the first approach (A) introduced in Section 3.1. to parametrizing the D^{*+} momentum, because of the better resolution provided (Fig. 4.1). When making use of parametrization (B) similar results are obtained, but with a smaller statistical significance.

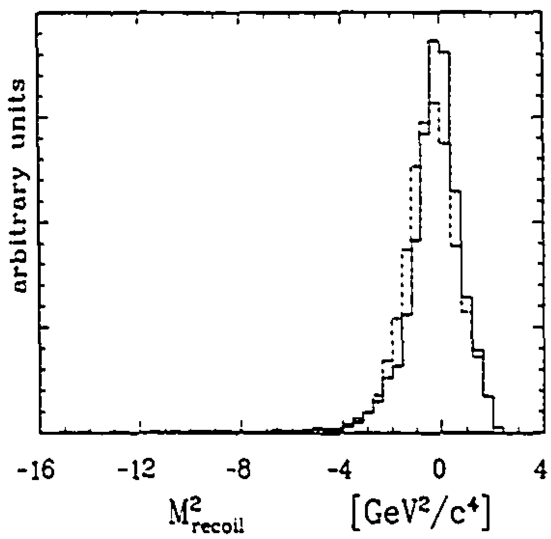

Figure 4.1: M^2_{recoil} mass spectra for ($\ell^{\pm} - \pi^{\mp}$) combinations for Monte Carlo simulation of the decay $\bar{B}^0 \to D^{*+}\ell^-\bar{\nu}$ obtained using parametrization (A) and parametrization (B) (dash-dotted histogram). For comparison, the two histograms are normalized to unit area.

4.1 Measurement of the $B^0\bar{B}^0$ mixing parameter

Tagging in the $\bar{B}^0 \to D^{*+}\ell^-\bar{\nu}$ mode provides a sample of $\bar{B}^0$ mesons, with which a measurement of the $B^0\bar{B}^0$ mixing rate can be made. This can be achieved using the sign of a fast lepton as a tag for the flavour of the other B meson, as indicated in Table 4.1.

The mixing parameter r which is equal to the ratio of mixed over unmixed events will then be

$$r_d = \frac{N(\bar{B}^0\ell^-)}{N(\bar{B}^0\ell^+)}. \tag{4.1}$$

The requirement of an additional lepton with momentum $1.4 \leq p_\ell \leq 2.5\ GeV/c$ in the event is therefore made. Furthermore, the charged track multiplicity, n_{cha},

$B^0\bar{B}^0$ events	B^0B^0 or $\bar{B}^0\bar{B}^0$ events
$\left.\begin{array}{l}\bar{B}^0 \to D^{*+}\ell_1^-\bar{\nu} \\ B^0 \to \ell_2^+\nu X\end{array}\right\} \Rightarrow D^{*+}\ell_1^- \;\; \ell_2^+$	$\left.\begin{array}{l}\qquad\quad \bar{B}^0 \to D^{*+}\ell_1^-\bar{\nu} \\ B^0 \to \;\; \bar{B}^0 \to \ell_2^-\nu X\end{array}\right\} \Rightarrow D^{*+}\ell_1^- \;\; \ell_2^-$

Table 4.1: Signature for mixed/unmixed events in $(D^*\ell)\ell$ correlations.

was required to be $n_{cha} \geq 4$. To extract the mixing parameter r, the M^2_{recoil} distribution for these events was studied.

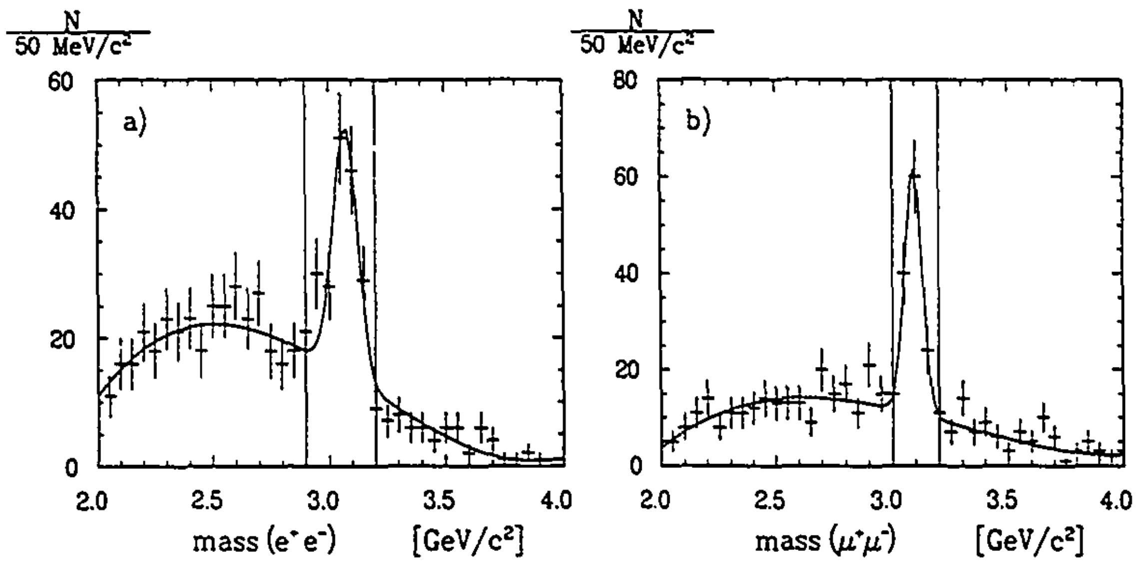

Figure 4.2: Mass spectra for e^+e^- (a) and $\mu^+\mu^-$ (b). The mass intervals used for rejecting leptons from J/ψ decays are also shown.

To suppress leptons coming from J/ψ decays, all e^+e^- pairs with invariant mass in the region $2.9-3.2$ GeV/c^2, and all $\mu^+\mu^-$ pairs with invariant mass in the region $3.0-3.2$ GeV/c^2, were rejected. The e^+e^- and $\mu^+\mu^-$ invariant mass spectra are shown in Figure 4.2. The asymmetric mass cut is due to the distortion of the J/ψ invariant mass distribution due to the radiation of a Bremsstrahlung photon from the decay electrons.

Using a Monte Carlo simulation, the shape of the uncorrelated background with and without the requirement of an additional lepton in the event was compared.By this means it was found that the background shape used in the D^*-lepton analysis (described in Chapter 3.3) provides a good description here as well. For comparison, the M^2_{recoil} spectrum resulting from a Monte Carlo simulation for "wrong sign" $(\ell^\pm - \pi^\pm)$ combinations is normalized separately to the number of uncorrelated $(\ell^\pm - \pi^\mp)$ background events for the cases of $(\ell^\pm - \pi^\mp)\ \ell^\pm$ and of $(\ell^\pm - \pi^\mp)\ \ell^\mp$ and the spectra are shown in Figure 4.3 (a) and (b) respectively.

The M^2_{recoil} distributions are therefore fitted using the shape of the background from the previous analysis; that is, using the shape of the "wrong sign" $(\ell^\pm - \pi^\pm)$ combinations obtained for $\Upsilon(4S)$ events after subtracting the continuum contribution. The resulting distributions for like- and unlike-sign dileptons, as well as the result of the fit, are shown in Figure 4.4.

The relative contributions of D^*_J and D^{*+} to the spectra were fixed from the one lepton case, and the fits were performed taking into consideration that

$$\begin{aligned} 2 \cdot Br(\bar{B}^0 \to D^{**+}\ell^-\bar{\nu}) \cdot Br(D^{**+} \to D^{*+}\pi^0) = \\ Br(B^- \to D^{**0}\ell^-\bar{\nu}) \cdot Br(D^{**0} \to D^{*+}\pi^-) \end{aligned}$$

according to isospin invariance. Charged B mesons accompanied by a primary lepton are expected to contribute only to the unlike-sign dilepton signal.

$$\begin{aligned} B^- &\longrightarrow D_J^{*0}\ell_1^-\ \bar{\nu} \\ &\qquad\quad \lfloor\!\longrightarrow D^{*+}\pi^- \\ B^+ &\longrightarrow \ell_2^+\nu X \end{aligned}$$

The continuum contribution was also subtracted. The fit yielded

$$\begin{aligned} N\ ((\ell^\pm - \pi^\mp)\ \ell^\pm) &= 42.4 \pm 10.6 \\ N\ ((\ell^\pm - \pi^\mp)\ \ell^\mp) &= 171.6 \pm 17.8. \end{aligned} \tag{4.2}$$

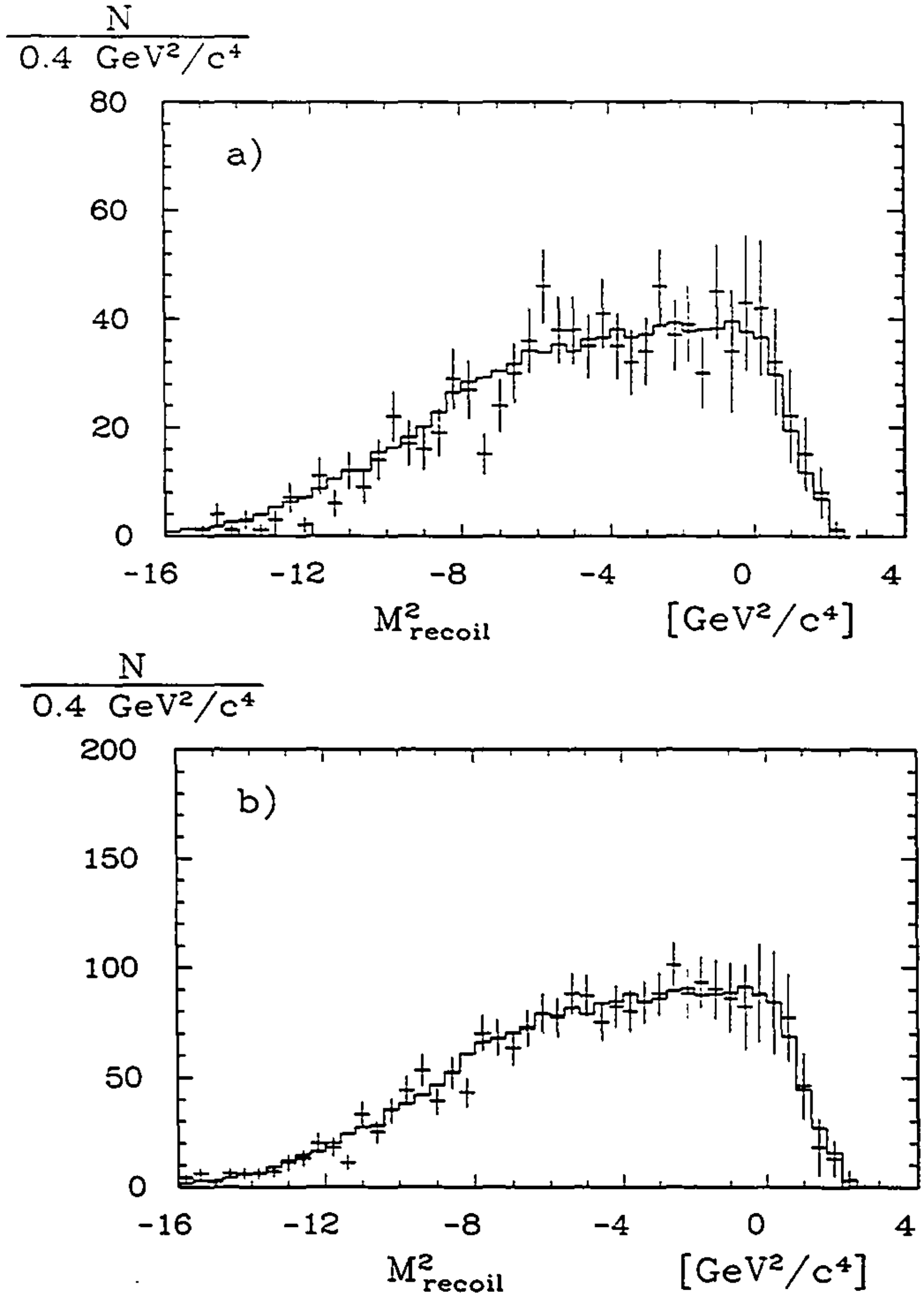

Figure 4.3: M^2_{recoil} spectra for uncorrelated "right-sign" ($\ell^\pm - \pi^\mp$) combinations in the case of $(\ell^+ - \pi^-)\ell^\pm$ (points with error bars) and normalized "wrong-sign" ($\ell^\pm - \pi^\pm$) combinations when no additional lepton is required (histogram), both obtained from Monte Carlo simulation. a) and b) correspond the cases of $(\ell^+ - \pi^-)\ell^+$ and $(\ell^+ - \pi^-)\ell^-$ respectively.

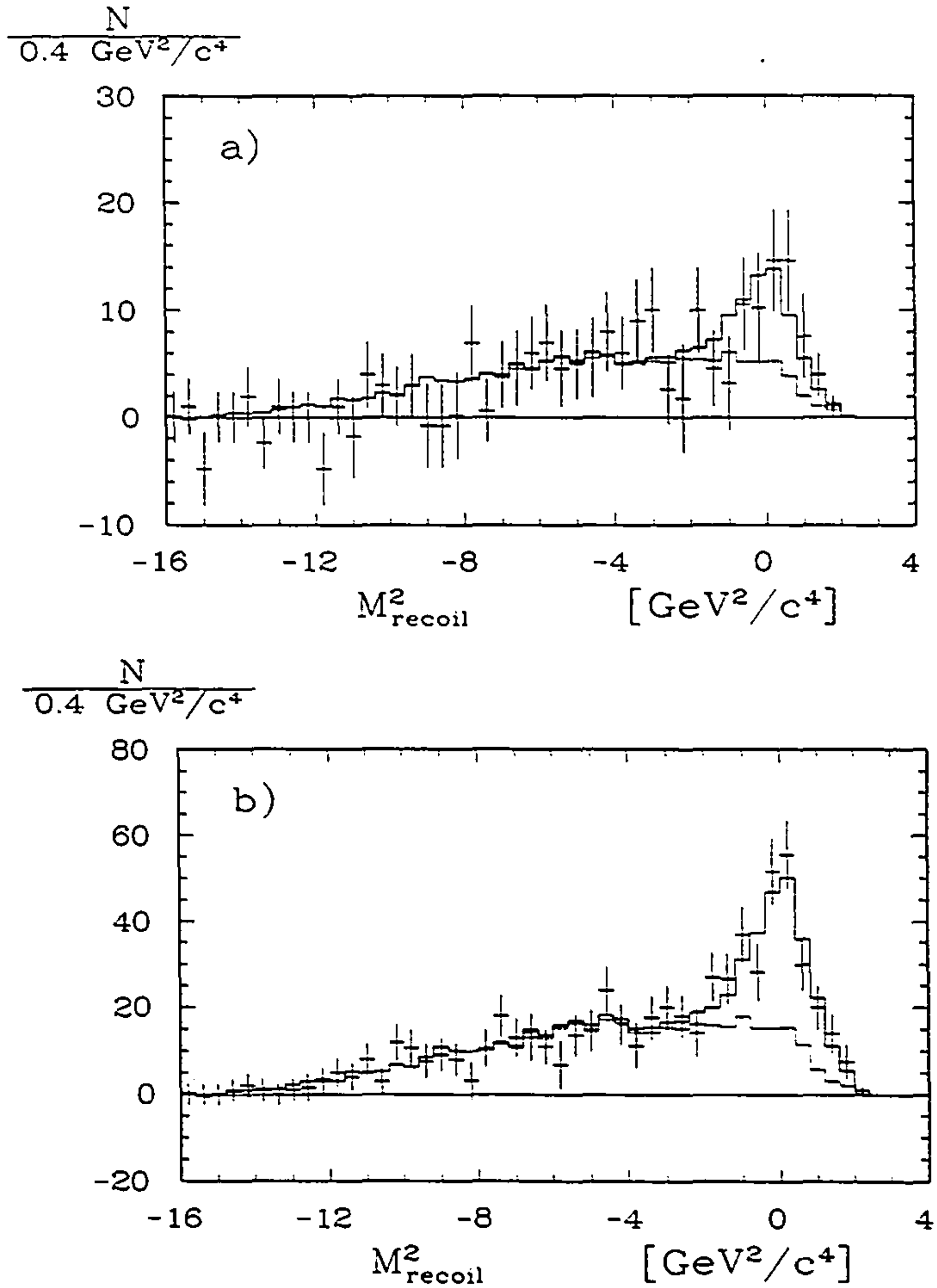

Figure 4.4: M^2_{recoil} spectra for $\ell^+\pi^-$ (points with errors) for events with an additional lepton with momentum $1.4 < p_\ell < 2.5$ GeV/c showing background (dotted histogram) and the result of the fit (full histogram) a) for like-sign dileptons (mixed candidate events); b) for unlike-sign dileptons (unmixed candidate events).

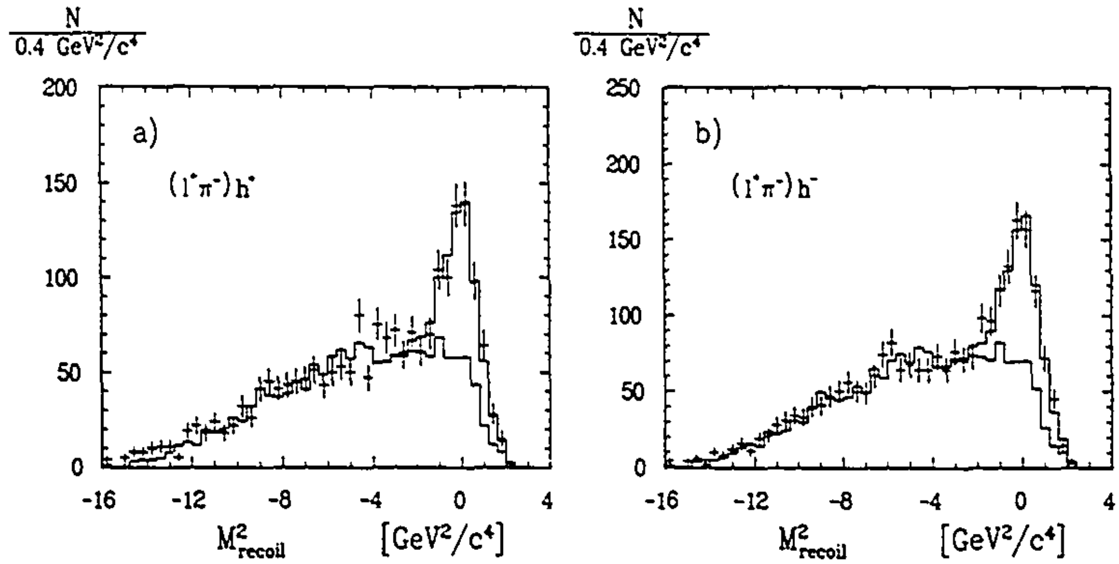

Figure 4.5: M^2_{recoil} mass spectra for $(\ell^{\pm} - \pi^{\mp})\ h^{\pm}$ (a) and $(\ell^{\pm} - \pi^{\mp})\ h^{\mp}$ (b) for $\Upsilon(4S)$ data. The results of the fits are also shown.

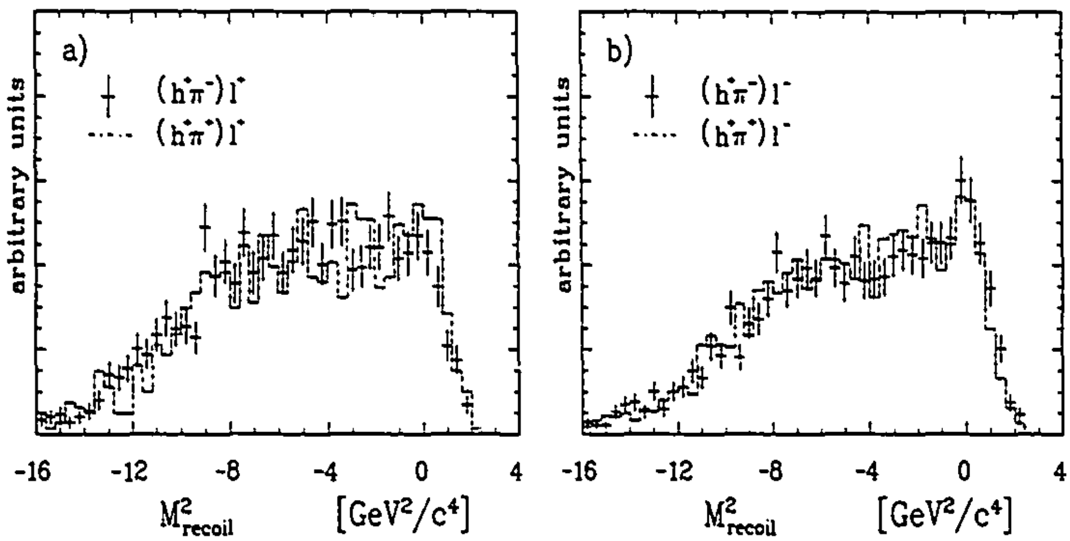

Figure 4.6: M^2_{recoil} mass spectra for $(h^{\pm} - \pi^{\mp})\ \ell^{\pm}$ (points with error bars) and $(h^{\pm} - \pi^{\pm})\ \ell^{\pm}$ (dash-dotted histogram) (a) and $(h^{\pm} - \pi^{\mp})\ \ell^{\mp}$ (points with error bars) and $(h^{\pm} - \pi^{\pm})\ \ell^{\mp}$ (dash-dotted histogram) (b) for $\Upsilon(4S)$ data. For comparison, all distributions are normalized to unit area.

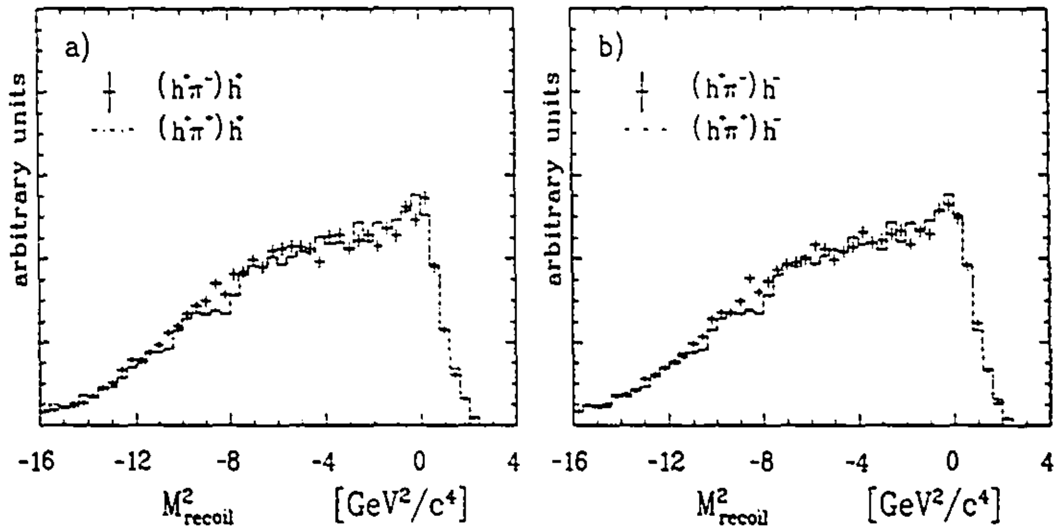

Figure 4.7: M^2_{recoil} mass spectra for $(h^\pm - \pi^\mp)$ $h^\pm$ (points with error bars) and $(h^\pm - \pi^\pm)$ $h^\pm$ (dash-dotted histogram) (a) and $(h^\pm - \pi^\mp)$ $h^\mp$ (points with error bars) and $(h^\pm - \pi^\pm)$ $h^\mp$ (dash-dotted histogram) (b) for $\Upsilon(4S)$ data. For comparison, all distributions are normalized to unit area.

The number of fake leptons was determined from the data by taking those events with a right sign $(\ell^\pm - \pi^\mp)$ combination containing an additional hadron with momentum lying in the same interval as that of the additional lepton. The M^2_{recoil} spectrum was then fit in the same way as for $(\ell^\pm - \pi^\mp)$ ℓ combinations, as shown in Figure 4.5, and the resulting $N(l^+\pi^-)h^\pm$ were multiplied with the hadron fake probability. As already noted in Section 3.4, the latter was estimated to be $0.5 \pm 0.1\%$ for electrons and $1.5 \pm 0.15\%$ for muons.

The case $(h^+\pi^-)\ell^\pm$ was also studied by taking right and wrong-sign $(h - \pi)$ combinations, where the hadron momentum was again required to lie in the interval $1.4 \leq p_h \leq 2.5$ GeV/c, along with an additional lepton. The M^2_{recoil} distributions for the cases of right and wrong-sing $(h-\pi)\ell$ combinations were found to be the same, as expected, implying that this case is already accounted for in the uncorrelated background. The M^2_{recoil} spectra are shown in Figure 4.6.

For the same reason, $(h - \pi)h$ combinations are also expected to contribute no background to the M^2_{recoil} distribution under study. The recoil mass spectra for $(h^+ - \pi^-)\ h^{\pm}$ and $(h^+ - \pi^+)\ h^{\pm}$ are shown in Figure 4.7. The total number of fake signal events was found to be:

$$\begin{aligned} N\left((\ell^{\pm} - \pi^{\mp})\ h^{\pm}\right) &= 7.0 \pm 0.9 \\ N\left((\ell^{\pm} - \pi^{\mp})\ h^{\mp}\right) &= 6.7 \pm 0.9 \end{aligned} \tag{4.3}$$

The number of $(D^*\ell)\ell$ events therefore has to be calculated according to:

$$N(D^{*-}\ell^+)\ell^{\pm} = (N_{events from fit} - N_{fakes}) \cdot (1 - D^{**} contribution) \tag{4.4}$$

The numbers obtained using 4.4 still contain contributions from $(D^*\ell)\ell_{sec}$ combinations which are a significant source of background for the processes shown in Table 4.1:

$$\left.\begin{array}{l} \bar{B}^0 \to D^{*+}\ell_1^-\bar{\nu} \\ B^0 \to X\ \ Y \\ \quad\hookrightarrow \ell^-_{2sec}\ \bar{\nu}\ Z \end{array}\right\} \Rightarrow D^{*+}\ell_1^-\ \ell^-_{2sec} \qquad \left.\begin{array}{l} \qquad\quad \bar{B}^0 \to D^{*+}\ell_1^-\bar{\nu} \\ B^0 \to \bar{B}^0 \to X\ \ Y \\ \qquad\qquad\hookrightarrow \ell^+_{2sec}\ \bar{\nu}\ Z \end{array}\right\} \Rightarrow D^{*+}\ell_1^-\ \ell^+_{2sec}$$

To extract the $(D^*\ell)\ell_{prim}$ contribution, the fraction of primary leptons was determined from Monte Carlo simulation.

Before taking the value for this contribution from Monte Carlo, a check was made to ensure that the Monte Carlo provides a good description of the data. For this purpose, the momentum distributions for the additional lepton were extracted for electrons and muons separately, when $M^2_{recoil} > -2.0\ GeV^2/c^4$. In this case the momentum cut for the additional lepton was relaxed to $p_e > 0.5\ GeV/c$ and $p_\mu > 0.9\ GeV/c$, since the cut of $p_\ell > 1.4\ GeV/c$ would leave very few cascade leptons, and the fit would therefore provide a very poor estimate. The cut on M^2_{recoil} is made to enrich the sample in events of the type $B \to D^*\ell\nu X$. After continuum subtraction, the fake lepton contribution is found by taking the hadron momentum spectrum for $(D^*\ell)h^{\pm}$ combinations for events for which the calculated M^2_{recoil} for the $(D^*\ell)$ combination is again $M^2_{recoil} > -2.0\ GeV^2/c^4$, and multiplying by the momentum dependent hadron-lepton fake probability. The contribution of fake leptons is then subtracted and the momentum spectrum of the additional lepton obtained after dividing by the lepton efficiencies. These lepton momentum spectra are subsequently fitted with the primary and secondary lepton spectra taken from the ISGW model. The fits for $(D^{*\mp}\ell^{\pm})e^{\pm}$, $(D^{*\mp}\ell^{\pm})\mu^{\pm}$, $(D^{*\mp}\ell^{\pm})e^{\mp}$ and $(D^{*\mp}\ell^{\pm})\mu^{\mp}$ are shown in Figures 4.8 and 4.9.

A comparison is then made between the fractions of primary leptons given from the fits and the corresponding Monte Carlo fractions. The resulting fractions for the case of electrons for the data are:

$$\frac{(D^{*\mp}\ell^{\pm})e^{\pm}}{(D^{*\mp}\ell^{\pm})e^{\mp}} = \frac{0.71 \pm 0.12}{0.44 \pm 0.07}, \tag{4.5}$$

or a ratio of 1.62 ± 0.37; the corresponding Monte Carlo fractions are:

$$\frac{(D^{*\mp}\ell^{\pm})e^{\pm}}{(D^{*\mp}\ell^{\pm})e^{\mp}} = \frac{0.74 \pm 0.06}{0.44 \pm 0.03}, \tag{4.6}$$

with a ratio of 1.66 ± 0.18. In the case of muons, where the statistics is lower, this ratio is 1.51 ± 0.76 from the data and 1.71 ± 0.61 from the Monte Carlo. For the specific interval $1.4 \leq p_\ell \leq 2.5$ GeV/c, these fractions give the following ratio:

$$\frac{\text{fraction of primary leptons in } (D^{*\mp}\ell^{\pm})e^{\pm}}{\text{fraction of primary leptons in } (D^{*\mp}\ell^{\pm})e^{\mp}} = 0.88 \pm 0.24 \tag{4.7}$$

while the corresponding Monte Carlo value is 0.93 ± 0.11.

The same test was performed for the region $M^2_{recoil} < -2.0$ GeV^2/c^4. The values extracted from the data for the fractions and ratios mentioned above agree well with the ones obtained from Monte Carlo. Since the comparison shows that the Monte Carlo provides a consistent description of the data, the fraction of primary leptons for signal events was taken from the Monte Carlo.
The results are summarized in Table 4.2.

A correction factor for the anti-J/ψ cut efficiency needs to be applied. This correction factor was calculated using Monte Carlo and was checked by fitting the J/ψ signal as obtained in the data. For this check, the anti J/ψ cut was removed and the recoil mass spectra for the cases of like and unlike-sign dilepton pairs were again fitted. A comparison of the excess of events given from the fit for the $N((D^{*\mp}\ell^{\pm})\ell^{\pm})$

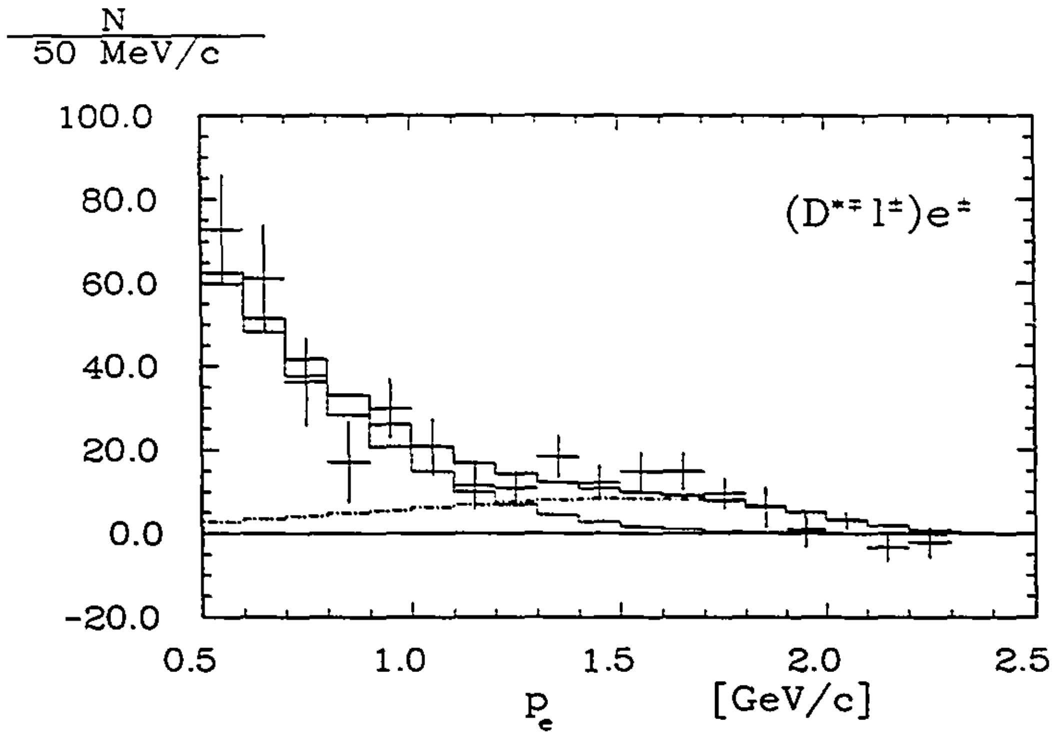

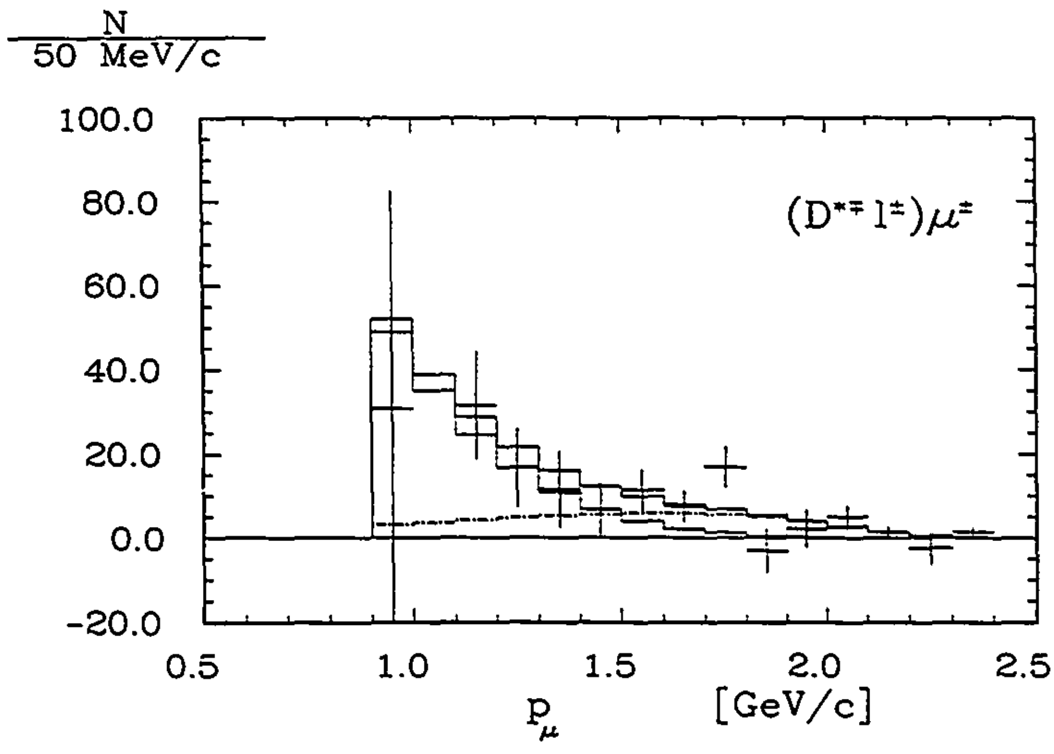

Figure 4.8: Fit results for $(D^{*\mp}\ell^{\pm})\ell^{\pm}$ combinations with $M^2_{recoil} > -2.0\ GeV^2/c^4$. Also shown are the primary (dashed-dotted histogram) and cascade (dotted histogram) lepton components.

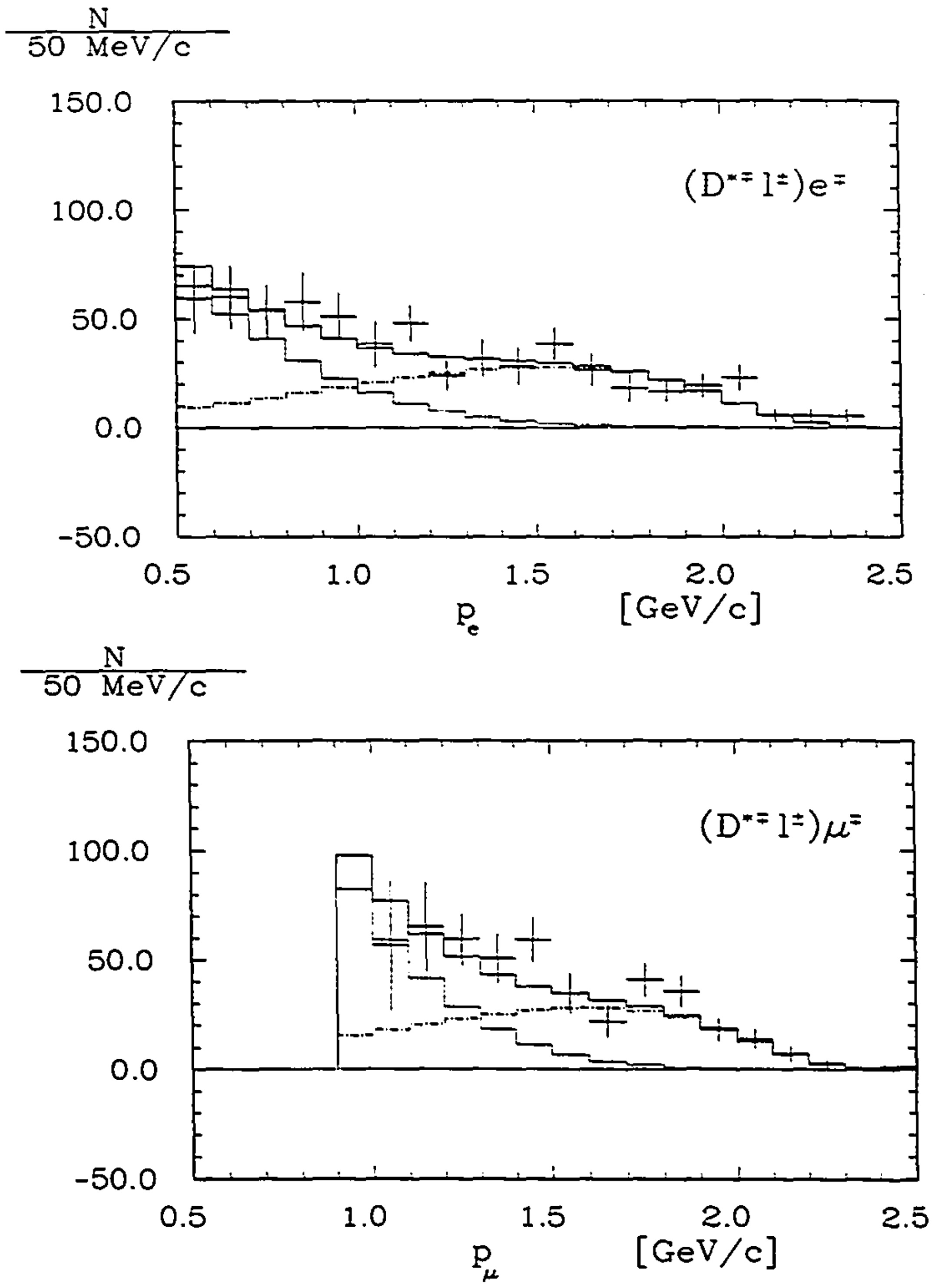

Figure 4.9: Fit results for $(D^{*\mp}\ell^{\pm})\ell^{\mp}$ combinations with $M^2_{recoil} > -2.0\ GeV^2/c^4$. Also shown are the primary (dashed-dotted histogram) and cascade (dotted histogram) lepton components.

Table 4.2: Observed numbers of events and corrections

	$N(D^{*-}\ell^+)\ell^+$	$N(D^{*-}\ell^+)\ell^-$
$\Upsilon(4S) - Continuum(scaled)$	42.4 ± 10.6	171.6 ± 17.8
Fakes	7.0 ± 0.9	6.7 ± 0.9
fraction of primary leptons	0.794	0.955
(1 - D^{**}contribution)	0.941	0.824
Direct leptons from neutral B decays	26.5 ± 8.0	129.8 ± 14.0

and $N((D^{*\mp}\ell^{\pm})\ell^{\mp})$ was then made with the ratio of background under the J/ψ signal and the signal itself. The number extracted from the data using this method agrees well with the one given from Monte Carlo, but since the statistics is very poor, the Monte Carlo value for this correction factor $\eta_{J/\psi} = 0.95$ was taken.

The mixing parameter r_d is

$$r_d = \frac{N((D^{*\mp}\ell^{\pm})\ell^{\pm})}{N((D^{*\mp}\ell^{\pm})\ell^{\mp})} \cdot \eta_{J/\psi} \tag{4.8}$$

Using (4.8), the value

$$r_d = 0.194 \pm 0.062$$

is found.

4.1.1 Systematic errors

To study the systematic errors contributing to this measurement:

- Different fitting procedures were followed to test the sensitivity of the result to the way the fit of the distributions was performed (e.g. the M^2_{recoil} spectra in $\Upsilon(4S)$ and continuum were fitted separately and then the scaled continuum yield was subtracted). The contribution of this source to the systematic error was found to be 0.015.

- The cut on the momentum of the additional lepton was changed and the procedure described above repeated. The variation of the mixing parameter with the lepton momentum cut contributes 0.049 to the systematic error.

- The uncertainties for the measured branching ratios for the different cascade lepton production mechanisms were considered. Taking a deviation of 1 σ from the values quoted by the Particle Data Group [2] for the various $c \rightarrow s$ semileptonic processes, results in an error in the knowledge of the fraction of primary leptons which in turn imposes an additional contribution of 0.006 to the systematic error.

- The $\frac{D^*_{(J)}}{D^*}$ ratio used in the fitting procedure was changed to 22.0% which is the value reported in [58] corresponding to $p_\ell \geq 1.4$ GeV/c for the momentum of the lepton that accompanies the D^* in the $B \rightarrow D^*_{(J)}\ell\nu$ decay mode. This resulted in a contribution of 0.010 to the systematic error.

- To study the uncertainty on the lepton identification in ARGUS, radiative Bhabha events were used as an electron sample, while for muons cosmic-ray muon events were used. A comparison of the resulting efficiencies with the ones obtained from a Monte Carlo simulation was then made. This contribution to the systematic error was found to be 1.2% for electron and 1.0% for muon identification [61], leading to a systematic error of 0.002.

- Finally, uncertainties in the ratio of the fractions of primary leptons obtained from Monte Carlo for the two samples, that is for $(D^{*-}\ell^+)\ell^+$ and $(D^{*-}\ell^+)\ell^-$, and in the correction factor for the anti J/ψ cut efficiency required an additional systematic error of 0.013 and 0.006 respectively.

The systematic errors are summarized in Table 4.3.

The value obtained for the mixing parameter r_d is therefore

$$r_d = 0.194 \pm 0.062 \pm 0.054$$

source	systematic error
background estimation and fitting procedure	1.47%
cut on the lepton momentum	4.93%
uncertainty in the estimated fraction of primary leptons	0.61%
uncertainty in the $\frac{D^*_{(J)}}{D^*}$ ratio	0.96%
lepton identification	0.21%
uncertainty in ratio of the fractions of primary leptons for mixed/unmixed candidates	1.26%
correction factor for the anti-J/psi cut	0.56%
total	5.4%

Table 4.3: Systematic errors for the determination of the mixing parameter r.

leading to a $\chi_d = r_d/(1 + r_d)$ value of

$$\chi_d = 0.162 \pm 0.044 \pm 0.038.$$

This measurement is independent of $\lambda = b_+^2 f_+ / b_0^2 f_0$, where f^+ (f^0) is the branching ratio for $\Upsilon(4S)$ decaying into charged (neutral) B mesons and b_+ (b_0) the semileptonic branching ratio of charged (neutral) B mesons.

4.2 Measurement of the semileptonic branching ratio of the neutral B meson

Using the mode $\bar{B}^0 \to D^{*+}\ell^-\bar{\nu}$ to tag the $\bar{B}^0$ meson, a sample of events where $\Upsilon(4S) \to B^0\bar{B}^0$ (B^0B^0) is provided and hence a measurement of the semileptonic branching ratio of the neutral B meson can be made.

$$Br(\bar{B}^0 \to \ell^- \bar{\nu} X) \; = \;$$

$$\frac{[N(\bar{B}^0 \to D^{*+}\ell^-\bar{\nu}, B^0 \to \ell^+\nu X)] + [N(\bar{B}^0 \to D^{*+}\ell^-\bar{\nu}, \bar{B}^0 \to \ell^-\bar{\nu} X)]}{N(\bar{B}^0 \to D^{*+}\ell^-\bar{\nu})}$$

or

$$Br(\bar{B}^0 \to \ell^- \bar{\nu} X) = \frac{N^{corr}(D^{*+}\ell^-)\ell}{N(D^{*+}\ell^-)} \cdot \frac{\epsilon^{\ell}_{mult}}{\epsilon^{\ell\ell}_{mult}} \tag{4.9}$$

where $N^{corr}(D^{*+}\ell^-)\ell$ stands for the acceptance corrected number of $(D^{*+}\ell^-)\ell$ and $\epsilon^{\ell,\ell\ell}_{mult}$ are the efficiencies of the multiplicity cut for the single lepton and dilepton samples respectively.

$$N^{corr}(D^{*+}\ell^-)\ell \; = \; \frac{N(D^{*+}\ell^-)\ell^- + N(D^{*+}\ell^-)\ell^+}{\eta_\ell}$$

where η_ℓ is the efficiency for observing a lepton with momentum in the momentum interval $1.4 \leq p_\ell \leq 2.5 \;\; GeV/c$. To calculate this efficiency, the fraction of primary leptons that are produced with momentum lying in this particular interval has to be known. For this reason, a model had to be used for the extrapolation of the primary lepton momentum spectrum to low values of lepton momenta. Employing the IGSW model for this purpose, η_ℓ was found to be

$$\eta_\ell \; = \; 0.341 \pm 0.022.$$

Also,

$$N(D^{*+}\ell^-)\ell \; = \; 163.9 \pm 16.9.$$

The fractions of primary leptons, as well as the $D^*_{(J)}$ contributions and the correction factor for the anti-J/ψ cut efficiency $\eta_{J/\psi}$, are all considered separately for the $N(D^{*+}\ell^-)\ell^-$ and $N(D^{*+}\ell^-)\ell^+$, and the two numbers are then added to give $N(D^{*+}\ell^-)\ell$.

From a Monte Carlo simulation it was found that

$$\frac{\epsilon^{\ell}_{mult}}{\epsilon^{\ell\ell}_{mult}} = 1.046 \pm 0.023.$$

Taking these values along with

$$N_{D^{*+}\ell^-} = 2705 \pm 161.5$$

and using (4.9), the $\bar{B}^0$ semileptonic branching ratio is found to be

$$Br(\bar{B}^0 \to X\ \ell^- \bar{\nu}) = (9.3 \pm 1.1)\%.$$

For the systematic error estimate:

- the sensitivity of the result to the fitting procedure followed introduced a systematic error of 0.004;
- the dependence of the resulting branching ratio on the cut on the momentum of the additional lepton required adding 0.010 to the systematic error;
- use of the BSW model [48] to calculate the fractions of primary leptons for the cases of $N(D^{*+}\ell^-)\ell^-$ and $N(D^{*+}\ell^-)\ell^+$, as well as for the calculation of the efficiency η_ℓ, resulted in an additional systematic error of 0.009 and
- finally, including the errors on the ratio $\frac{\epsilon^{\ell}_{mult}}{\epsilon^{\ell\ell}_{mult}}$ and on η_ℓ, another 0.002 should be added to the systematic error.

The value obtained for the semileptonic branching ratio of the neutral B meson is therefore:

$$Br(\bar{B}^0 \to X\ \ell^- \bar{\nu}) = (9.3 \pm 1.1 \pm 1.5)\%, \tag{4.10}$$

which is in good agreement with the previous CLEO [68] measurement. The value is also consistent with the mean semileptonic branching ratio obtained by taking a weighted average of ARGUS [67] and CLEO [68] results, $Br(\bar{B} \to X\ \ell^- \bar{\nu}) = 9.85 \pm 0.5\%$. This value for the mean semileptonic branching ratio can be used together with the value obtained for the inclusive semileptonic branching ratio of neutral B mesons 4.10 to extract a value for the ratio of lifetimes of charged and neutral B mesons. Starting from the relation

$$< b >= f_+ b_+ + f_0 b_0, \tag{4.11}$$

where $< b >= Br(B \to X\ \ell^+\nu)$, $b_+(b_0) = Br(B^+(B^0) \to X\ \ell^+\nu)$ and f_+,f_- are the branching ratios of the $\Upsilon(4S)$ to charged and neutral B mesons, and taking $f_+/f_0 = 1.00 \pm 0.05$ [68], one obtains:

$$\frac{b_+}{b_0} = \frac{< b > - f_0 b_0}{f_+ b_0} = \frac{< b >}{f_+ b_0} - \frac{1}{f_+/f_0} = \frac{< b >}{b_0} \cdot (1 + \frac{1}{f_+/f_0}) - \frac{1}{f_+/f_0}. \tag{4.12}$$

Since semileptonic decays proceed via W emission, the semileptonic widths of the charged and neutral B mesons should be equal in the spectator model, implying that

$$\frac{b_+}{b_0} = \frac{\tau_+}{\tau_0}$$

(since $b = \tau \cdot \Gamma_{sl}$).

Thus, using:

$$\frac{Br(\bar{B} \to X\ \ell^-\bar{\nu})}{Br(\bar{B}^0 \to X\ \ell^-\bar{\nu})} = 1.06 \pm 0.14 \pm 0.17$$

an estimate of the ratio of the lifetimes of charged and neutral B mesons can be made. The value obtained is:

$$\tau(B^+)/\tau(B^0) = 1.12 \pm 0.27 \pm 0.34.$$

The theoretical uncertainty in the ratio f_+/f_0 has only very small influence on the result. The systematic error introduced by this source is 0.003.

This value is in good agreement with the expectation that non-spectator effects in B meson decays are small.

Chapter 5

Study of the $B^0\bar{B}^0$ mixing using D^{*+} $K^{\pm}$ correlations

5.1 Introduction

In the analysis presented in Chapter 4, the flavour content of B mesons is tagged by the charge of the fast lepton originating from the semileptonic decay of the B as shown in the Feynman graph of Figure 5.1.

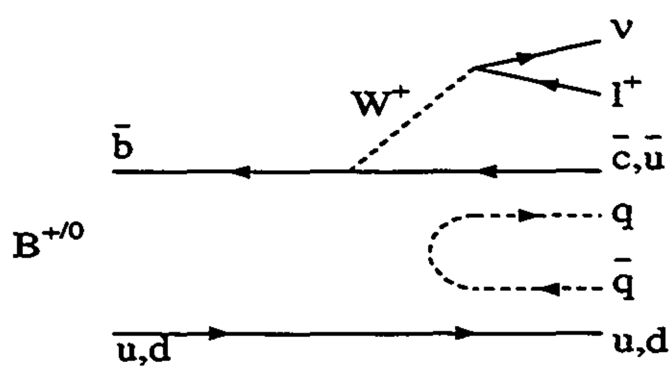

Figure 5.1: B meson semileptonic decay in the spectator model.

Another possibility to tag the B meson flavour is from the charge of the kaon coming from the $c \to s$ transition. The idea of kaon tagging is new and has been applied for the first time in this work. The motivation comes from the measurement of the number of kaons in $\Upsilon(4S)$ decays [73], [75] which indicates that making use of kaons for flavour tagging provides much higher statistics than the lepton tagging technique. In this case, however, exact knowledge of the kaon production rates is important. In this section, D^{*+} $K^{\pm}$ correlations are studied in an attempt to extract a value for the mixing parameter χ. To accomplish this, the flavour of one of the B mesons will be tagged from the charge of the D^* meson, while for the other B meson the charge of the kaon will be used.

Thus, events containing D^* and K of opposite charge provide a signature for mixing as indicated in the following Table: (Table 5.1).

$B^0\bar{B}^0$ events	B^0B^0 or $\bar{B}^0\bar{B}^0$ events
$\left.\begin{array}{l}\bar{B}^0 \to D^{*+}X \\ B^0 \to K^+X\end{array}\right\} \Rightarrow D^{*+}\ K^+$	$\left.\begin{array}{l}\bar{B}^0 \to D^{*+}X \\ B^0 \to \ \bar{B}^0 \to K^-X\end{array}\right\} \Rightarrow D^{*+}\ K^-$

Table 5.1: Signature of mixed/unmixed events through D^* K correlations.

In this case, if the charged D^* and the charged kaon were "perfect" flavour tags, the mixing parameter r would simply be given from:

$$r_d \; = \; \frac{N(D^{*+}K^-)}{N(D^{*+}K^+)}.$$

In the spectator model, D^{*+} mesons are produced when the c quark hadronizes together with the spectator quark as shown in Figure 5.2. When a B^0 decays, however, a certain fraction of "wrong" charged D^* mesons will also be produced due to the fragmentation of the quark pair created by the virtual W from the $b \to c$ transition as shown in Figure 5.3. For the same reason, and also due to the decays

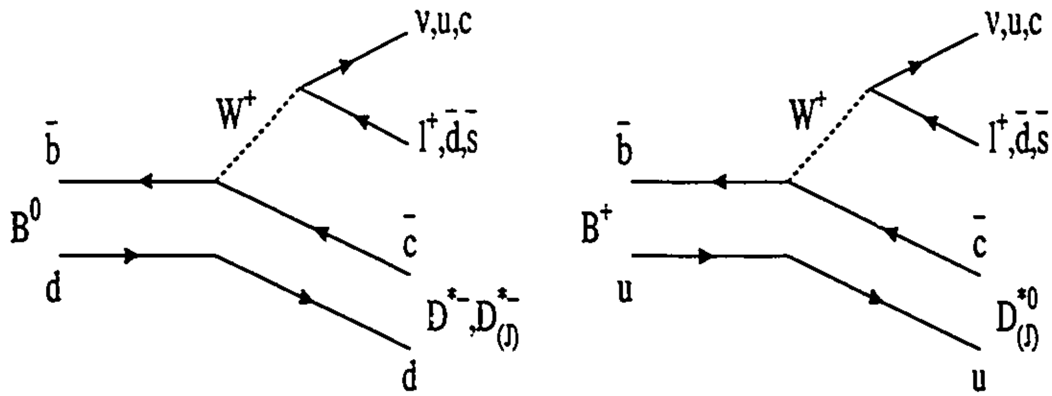

Figure 5.2: D^{*+} production in the spectator model.

Decay modes	$B^0, B^+ \rightarrow D^{*+}X : B^0 \rightarrow D^{*-}X : B^+ \rightarrow D^{*-}X$
Ratio of branching ratios	0.05 : 1 : 0.28

Table 5.2: Ratio of branching ratios for the different D^{*+} production mechanisms.

of higher excited $D^*_{(J)}$ states produced in B meson decays, a number of $D^{*\pm}$ mesons arising from the decay of the $B^{\pm}$ will also be present, as shown in Figures 5.2, 5.3.

To extract the mixing parameter χ the ratio $\frac{N(D^{*+}K^-)}{N(D^{*+}K^+)}$ will be used. This depends only on the ratio of branching ratios

$$Br(B^0, B^+ \rightarrow D^{*+}X) \ : \ Br(B^0 \rightarrow D^{*-}X) \ : \ Br(B^+ \rightarrow D^{*-}X)$$

and not on their absolute values as is also indicated by 5.13 and the set of equations 5.6 to 5.11 presented in Section 5.4. The $D^{*\pm}$, as well as the $K^{\pm}$ production rates, are taken from Monte Carlo and are presented in Tables 5.2 and 5.3 respectively. Comparisons of Monte Carlo and data are made in addition as a means to discovering possible discrepancies in these production rates.

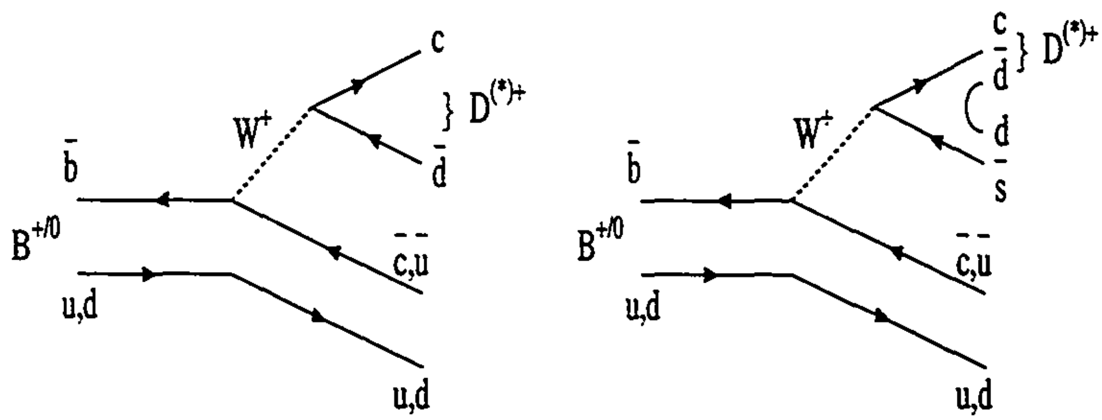

Figure 5.3: Production of "wrong" charged D^* mesons in the spectator model.

Decay mode	Branching ratio
$Br(B^0 \to K^+X)$	$(54.66 \pm 0.22)\%$
$Br(B^0 \to K^-X)$	$(14.38 \pm 0.10)\%$
$Br(B^+ \to K^+X)$	$(66.38 \pm 0.23)\%$
$Br(B^+ \to K^-X)$	$(13.94 \pm 0.09)\%$

Table 5.3: $K^{\pm}$ production rates considered for this analysis.

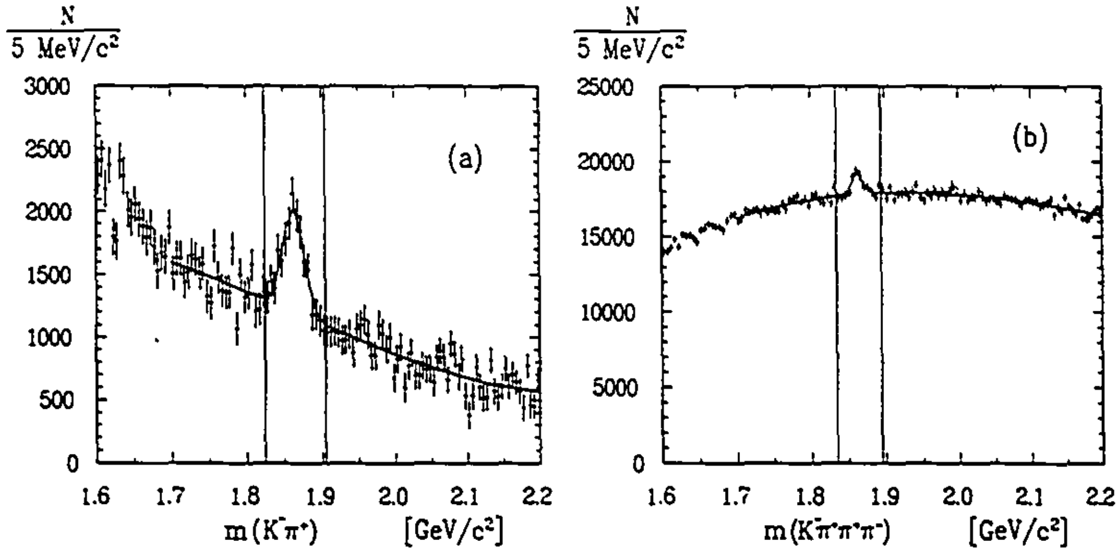

Figure 5.4: Invariant mass spectra for $K^-\pi^+$ (a) and $K^-\pi^+\pi^+\pi^-$ (b) combinations. A clear peak corresponding to the D^0 meson is observed. The accepted mass region for D^0 candidates is also indicated on the plots.

5.2 The decay $\bar{B} \to D^{*+}X$

As a consistency check, the inclusive $Br(\bar{B} \to D^{*+}X)$ has been determined. Here, a D^{*+} is meant to imply the sum of D^{*+} and D^{*-} mesons and, in addition, the charge of the B meson is not determined. For this analysis, events were required to have at least 5 charged tracks originating from the interaction region and to contain no track with momentum greater than 3.0 GeV/c which is the kinematical limit for tracks originating from B decays.

D^{*+} mesons were reconstructed through the decay modes:

$$D^{*+} \longrightarrow D^0\ \pi^+ \hookrightarrow K^-\ \pi^+ \quad \text{(i)} \qquad \text{and} \qquad D^{*+} \longrightarrow D^0\ \pi^+ \hookrightarrow K^-\ \pi^+\ \pi^+\ \pi^- \quad \text{(ii)}$$

D^0 candidates from the decays (i) and (ii) had to have a mass lying within 40 MeV/c^2 and 30 MeV/c^2, respectively, of the nominal D^0 mass (Fig. 5.4).

It was further required that the D^{*+} candidate have a scaled momentum $x_{p_{D^*}} < 0.5$, where x_p is defined as

$$x_{p_{D^*}} = \frac{|\vec{p_{D^*}}|}{p_{max}} \quad \text{where} \quad p_{max} = \sqrt{(E_{cms}/2)^2 - M_{D^{*}}^2}. \tag{5.1}$$

This $x_{p_{D^*}}$ cut enriches the sample with D^* mesons coming from B decays since $x_p = 0.5$ is approximately the upper kinematical limit for B meson daughter particles. The invariant mass distributions obtained for D^{*+} mesons reconstructed via the decay channel (i) and (ii) are shown in Figure 5.5 (a) and (b) respectively.

To fit these distributions, a second-order polynomial multiplied by a (square root) threshold function is used to parametrize the background and a Gaussian is used to describe the D^* signal. The number of events resulting from the fit is:

- For D^* mesons reconstructed via decay mode (i):

$$N_{D^*} = 702 \pm 50 \tag{5.2}$$

  with $\sigma = 0.954 \pm 0.048\ MeV/c^2$

- For D^*'s reconstructed via decay mode (ii):

$$N_{D^*} = 632 \pm 90 \tag{5.3}$$

  with $\sigma = 0.988 \pm 0.085\ MeV/c^2$.

The D^{*+} reconstruction efficiency is obtained from Monte Carlo simulation and is found to be:

- $\eta_i = 0.328 \pm 0.007$ when D^*'s are reconstructed via decay mode (i) and
- $\eta_{ii} = 0.156 \pm 0.009$ when D^*'s are reconstructed via decay mode (ii).

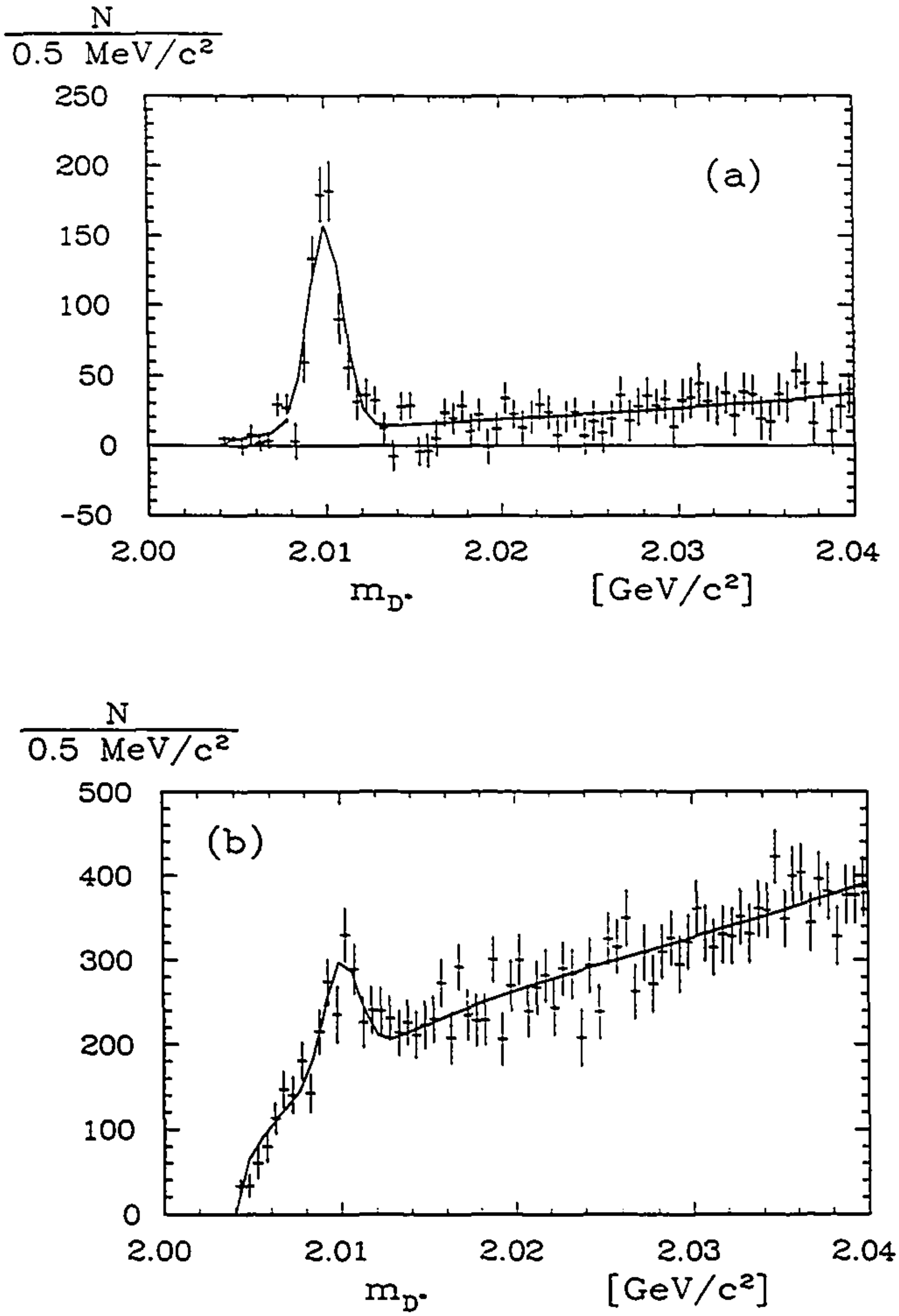

Figure 5.5: Invariant mass spectra for $D^0\pi^+$ combinations where the D^0 meson is reconstructed via the $K^-\pi^+$ (a) and $K^-\pi^+\pi^+\pi^-$ (b) channels for $\Upsilon(4S)$ events. The expected continuum contribution is subtracted from both plots.

The inclusive branching ratio for D^{*+} is then calculated from:

$$Br(\bar{B} \rightarrow D^{*+}\, X) = \frac{N_{D^{*+}}}{N_B \cdot\ Br(D^{*+} \rightarrow D^0\pi^+) \cdot Br(D^0 \rightarrow K^-\pi^+ \text{ .OR. } K^-\pi^+\pi^+\pi^-) \cdot (\eta_i \text{ .OR. } \eta_{ii})}.$$

Using the CLEO measurement [55] for

$$Br(D^{*+} \rightarrow D^0\, \pi^+) = (68.1\ \pm 1.0\ \pm 1.3)\%$$

and for the D^0 decays

$$Br(D^0 \rightarrow K^-\pi^+) = (4.01 \pm 0.14)\%$$

$$Br(D^0 \rightarrow K^-\pi^+\pi^+\pi^-) = (8.1 \pm 0.5)\%$$

as given in [2], the inclusive $B \rightarrow D^{*+}X$ branching ratio is extracted. The number of B mesons is $N_B = 396250 \pm 18000$. The value obtained for the branching ratio is :

$$Br(\bar{B} \rightarrow D^{*+}\, X) = (19.8 \pm 1.4 \pm 1.6 \pm 0.8)\% \tag{5.4}$$

when D^*'s are reconstructed via decay mode (i) and

$$Br(\bar{B} \rightarrow D^{*+}\, X) = (18.6 \pm 2.7 \pm 3.5 \pm 1.2)\% \tag{5.5}$$

when D^*'s are reconstructed via decay mode (ii). These measurements lead to a combined average value of

$$Br(\bar{B} \rightarrow D^{*+}\, X) = (19.6 \pm 1.9)\%.$$

The first error quoted in 5.4, 5.5 is the statistical error, while the next two are systematic errors. The first systematic error includes:

source	systematic error	
	decay channel (i)	decay channel (ii)
background estimation and fitting procedure	0.80%	3.1%
cut on the difference of the mass of the D^0 candidate from the nominal D^0 mass	0.98%	0.92%
number of B mesons and error on the D^{*+} reconstruction efficiency	1.00%	1.36%
total	1.6%	3.5%

Table 5.4: Systematic errors for the decay $Br(\bar{B} \to D^{*+}\ X)$.

- the error on the number of B mesons and the statistical error on the D^{*+} meson reconstruction efficiency which contribute in total 1.00% and 1.36% to the systematic error when D^* mesons are reconstructed via the decay channels (i) and (ii) respectively,
- a contribution from the fitting procedure of an additional 0.8% and 3.1% to the systematic error for the decay channels (i) and (ii), respectively,
- the influence of the cut on the difference of the mass of the D^0 candidates from the nominal D^0 meson mass. This was determined by relaxing the cut to 60 MeV/c^2 and 40 MeV/c^2 for the decays $D^0 \to K^-\pi^+$ and $D^0 \to K^-\pi^+\pi^+\pi^-$, respectively, and refitting the obtained D^{*+} signal. This results in an additional systematic error of 0.98% and 0.92% for the decay channels (i) and (ii) respectively.

The second systematic error quoted above is the propagated error on $Br(D^{*+} \to D^0\pi^+)$ and the D^0 meson decay branching ratio. The systematic errors are summarized in Table 5.4. The result is in good agreement with published

$Br(\bar{B} \to D^{*+}X)$	Reference
$(26.8 \pm 4.6)\%$	ARGUS [56]
$(21.2 \pm 4.0)\%$	CLEO [57]
$(19.6 \pm 1.9)\%$	this measurement

Table 5.5: Comparison of the value obtained for $Br(B \to D^{*+}X)$ with previous ARGUS and CLEO results. The error is the result of adding statistical and systematic errors in quadrature.

measurements by ARGUS [56] and CLEO [57] as shown in Table 5.5 where, for comparison, the values for the branching ratio have been re-evaluated to correspond with the D^{*+} and D^0 decay branching ratios used in this work.

As already mentioned, good agreement between Monte Carlo and data is important since the $D^{*\pm}$ and $K^{\pm}$ production rates are taken from Monte Carlo. Hence, as a first check, the observed momentum spectrum of D^* meson will be compared to that obtained from the Monte Carlo simulation which also incorporates the D^{*+} meson production via the virtual W bosons. To extract the momentum spectrum of the D^{*+} meson produced in B decays the procedure described below is followed. The invariant mass distribution of the $(D^0\pi^+)$ system was plotted for different momentum intervals and these distributions were then fitted using a free width for the Gaussian used to describe the D^{*+} signal. For this purpose, only the $D^0 \to K^-\pi^+$ channel was used since the signal to background ratio is much better and this channel therefore provides more accurate results. The width obtained from the fit for different D^{*+} meson momentum intervals is shown in Figure 5.6. The x_p spectrum of the D^{*+} meson is obtained by following the same procedure and is shown in Figure 5.8 for $\Upsilon(4S)$ events after subtracting the continuum contribution.

A fit was performed to extract the dependence of the D^{*+} width on the D^{*+} momentum, as shown by the solid line in Figure 5.6. The width was then constrained to the result of this fit and the mass distributions were refitted to obtain

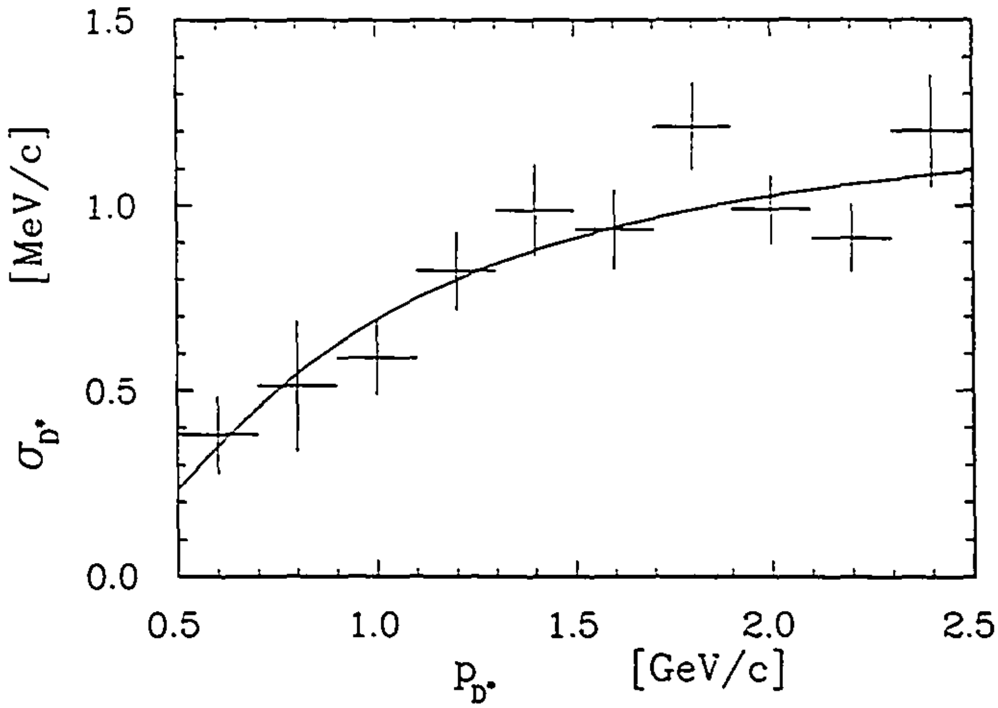

Figure 5.6: Dependence of the D^{*+} width on the momentum of the D^{*+} candidate.

the momentum spectrum of the charged D^* meson in B decays.

To extract the acceptance-corrected momentum spectrum of D^{*+} mesons produced in B decays (Figure 5.7), the momentum spectrum is divided by the D^{*+} reconstruction efficiency. The D^{*+} reconstruction efficiency as a function of the momentum of the reconstructed D^{*+} is found using Monte Carlo simulation and is shown in Figure 5.9.

5.3 Comparison of the data with the simulation

A study of the $B^0\bar{B}^0$ mixing using D^{*+} $K^{\pm}$ correlations requires exact knowledge of the D^* meson and kaon production rates, which for this analysis will be taken from the Monte Carlo simulation. Figure 5.7 shows the (efficiency corrected) D^{*+} meson momentum spectrum as obtained for $B\bar{B}$ events from data. For comparison, the results of the simulation which also includes D^{*+} production arising from the virtual

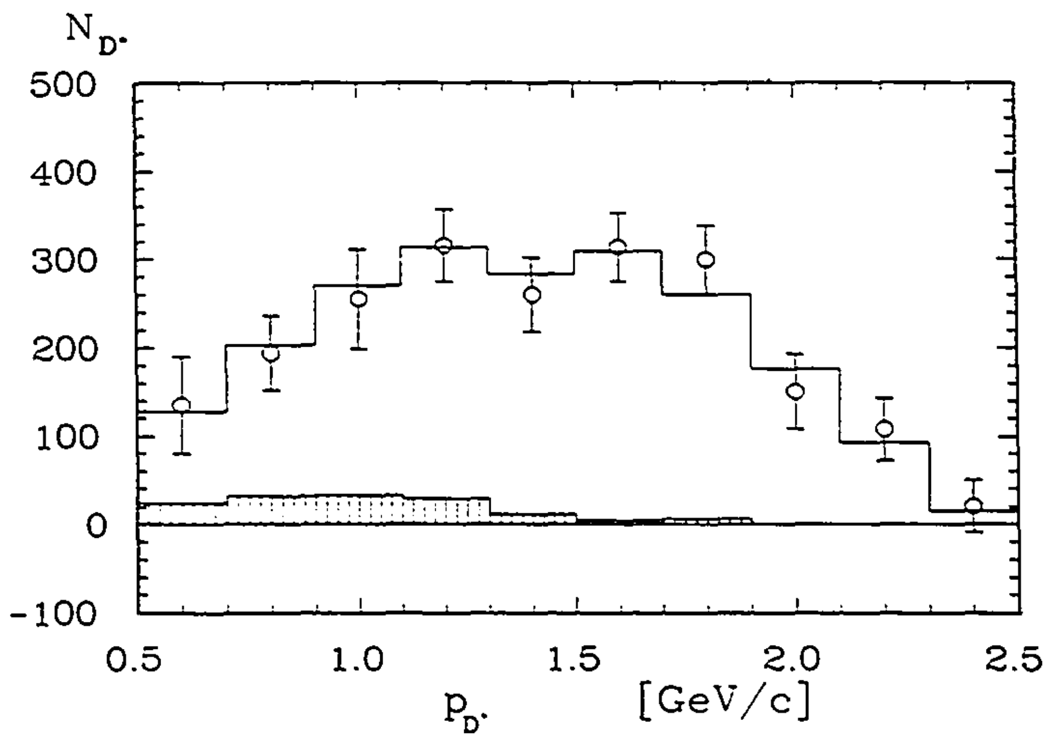

Figure 5.7: Efficiency corrected momentum spectrum for charged D^* mesons produced in B decays as obtained from data (points with error bars) and through Monte Carlo simulation (histogram). For comparison the distribution for Monte Carlo events is normalized to the same area as obtained in the data. The momentum distribution of the D^{*+} mesons coming from the virtual W for Monte Carlo simulated events is also shown (hatched histogram).

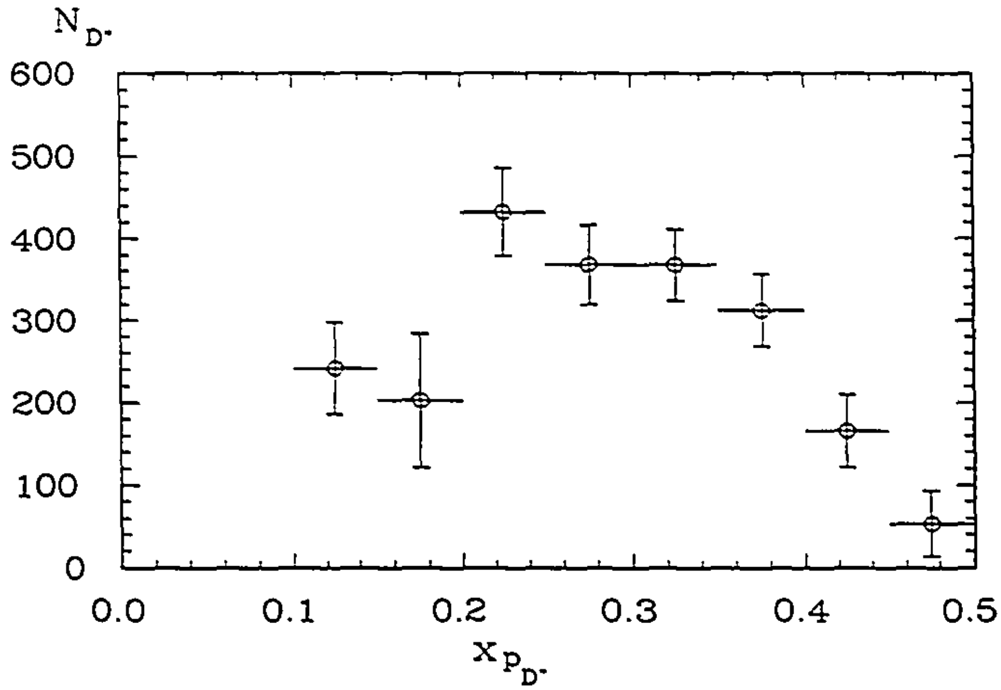

Figure 5.8: x_p spectrum for the D^{*+} meson produced in B decays.

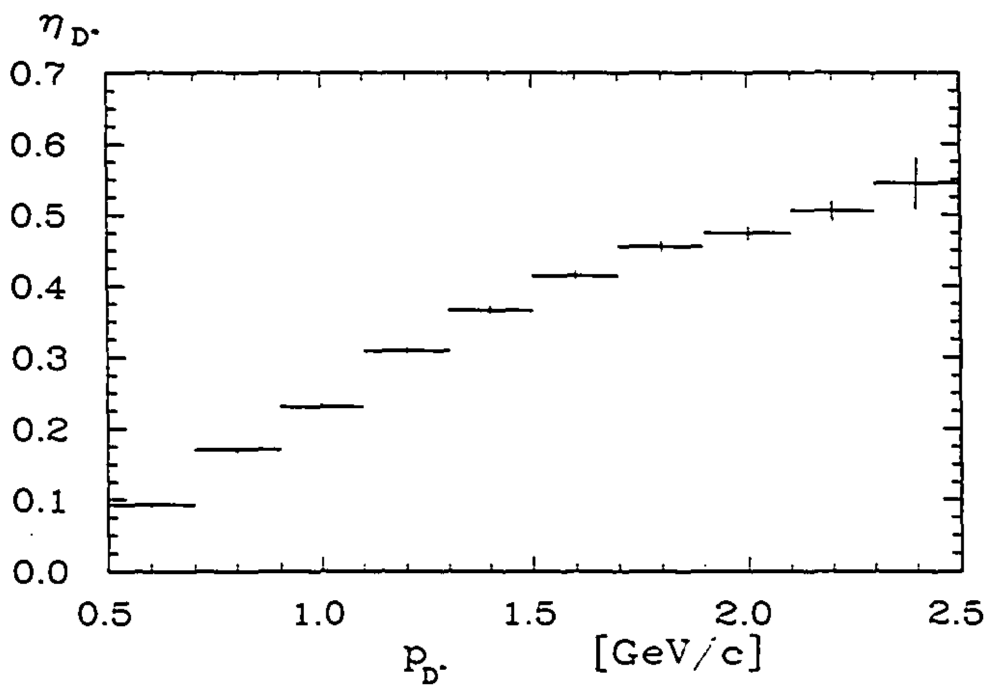

Figure 5.9: D^{*+} efficiency for the decay chain $D^{*+} \to D^0\pi^+$, $D^0 \to K^-\pi^+$ derived using Monte Carlo simulation.

W is indicated.

The kaon momentum spectrum obtained for $B\bar{B}$ events from the data also needs to be compared to the Monte Carlo simulation. For this purpose, the kaon efficiency was calculated by studying the decay $\phi \rightarrow K^+K^-$. For both $\Upsilon(4S)$ data and Monte Carlo, the number of ϕ's found when both selected kaons fulfilled the usual likelihood cut $LhK_1, LhK_2 \geq 0.01$, was compared to the number of ϕ's obtained when one of the kaons was required to have a likelihood greater than 80%, that is, $LhK_1 \geq 0.01$, $LhK_2 \geq 0.80$. The K^+K^- invariant mass spectra for different kaon momentum intervals ($0.2 \leq p_K \leq 0.5$, $0.5 \leq p_K \leq 0.8$, $0.8 \leq p_K \leq 1.0$ GeV/c) are shown in Figure 5.10 for $\Upsilon(4S)$ events and for Monte Carlo generated events.

The numbers of ϕ's resulting from the fit for different momentum intervals with and without the hard likelihood cut for the kaon hypothesis are shown in Table 5.6 and the efficiencies obtained are shown in Table 5.7.

p_K	$\Upsilon(4S)$		simulation	
	$LhK_2 \geq 0.01$	$LhK_2 \geq 0.80$	$LhK_2 \geq 0.01$	$LhK_2 \geq 0.80$
p_K (0.2-0.5) GeV/c	3356 ± 69	3300 ± 68	2536 ± 60	2474 ± 59
p_K (0.5-0.8) GeV/c	4164 ± 81	2882 ± 64	2502 ± 58	1737 ± 47
p_K (0.8-1.0) GeV/c	1971 ± 72	485 ± 29	510 ± 33	123 ± 12

Table 5.6: Number of ϕ's obtained from $\Upsilon(4S)$ data and from the Monte Carlo simulation for different intervals of the kaon momentum with/without application of the hard likelihood cut.

Since the kaon efficiency derived from the data is in very good agreement with the one obtained from the Monte Carlo simulation for all momentum intervals considered, the momentum dependent efficiency used to extract the kaon momentum spectrum shown in Figure 5.11b) is taken from Monte Carlo and is shown in Figure 5.11a).

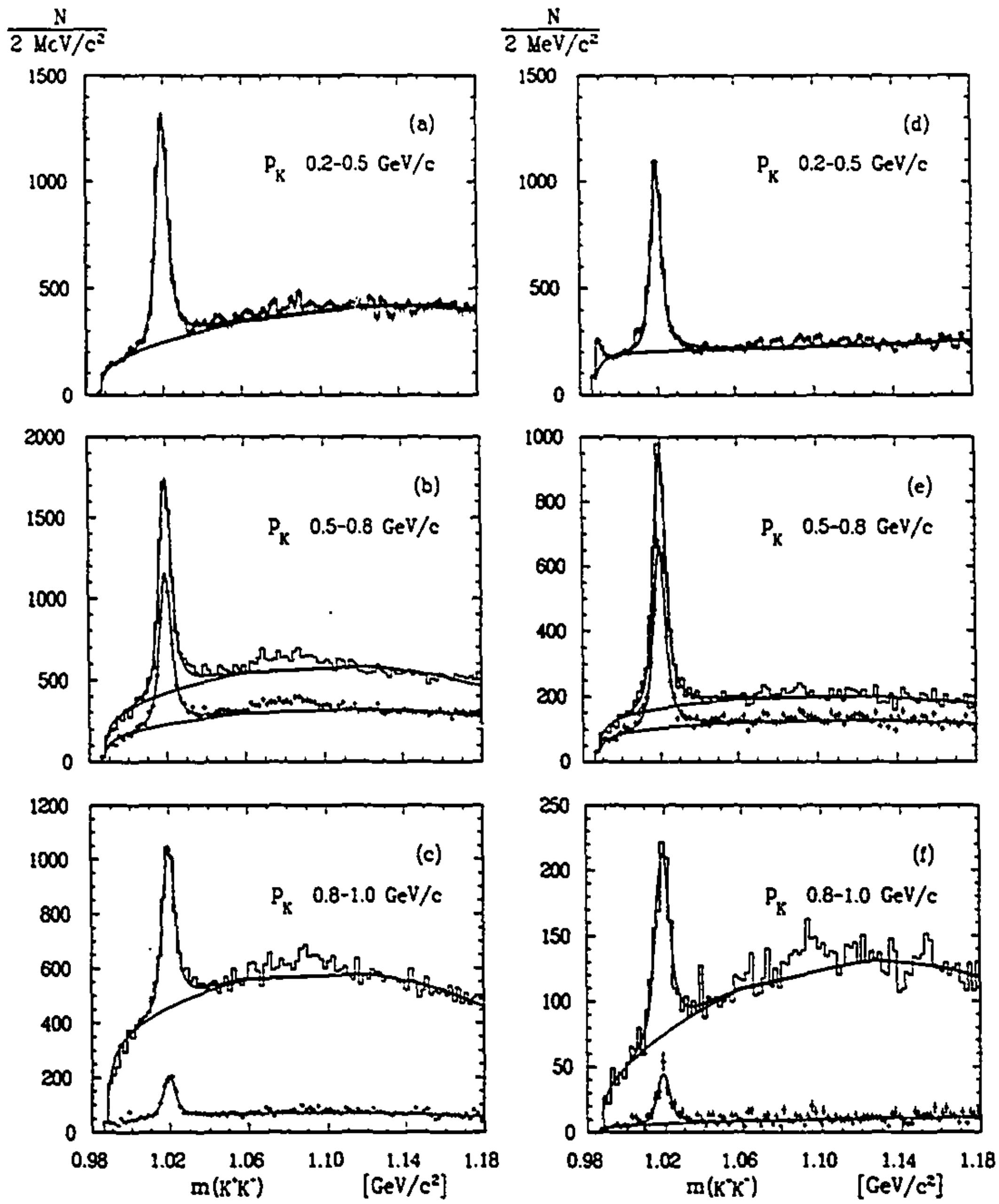

Figure 5.10: The K^+K^- invariant mass spectra for combinations with $LhK_1, LhK_2 \geq 0.01$ (histogram) and with $LhK_1 \geq 0.01$, $LhK_2 \geq 0.80$ (points with error bars). Both $\Upsilon(4S)$ data (a),(b),(c) and Monte Carlo generated events (d),(e),(f) are shown. The region $(1.06 - 1.12)$ GeV/c^2 where the reflection from the decay $K^* \rightarrow K\pi$ is expected, (π misidentified as K) was not included in the fit.

p_K	ratio for $\Upsilon(4S)$	ratio for simulation
(0.2-0.5) GeV/c	0.9833 ± 0.0286	0.9755 ± 0.0328
(0.5-0.8) GeV/c	0.6921 ± 0.0204	0.6942 ± 0.0247
(0.8-1.0) GeV/c	0.2460 ± 0.0173	0.2412 ± 0.0282

Table 5.7: Comparison of the kaon efficiencies for $\Upsilon(4S)$ and for Monte Carlo events for different intervals of the kaon momentum.

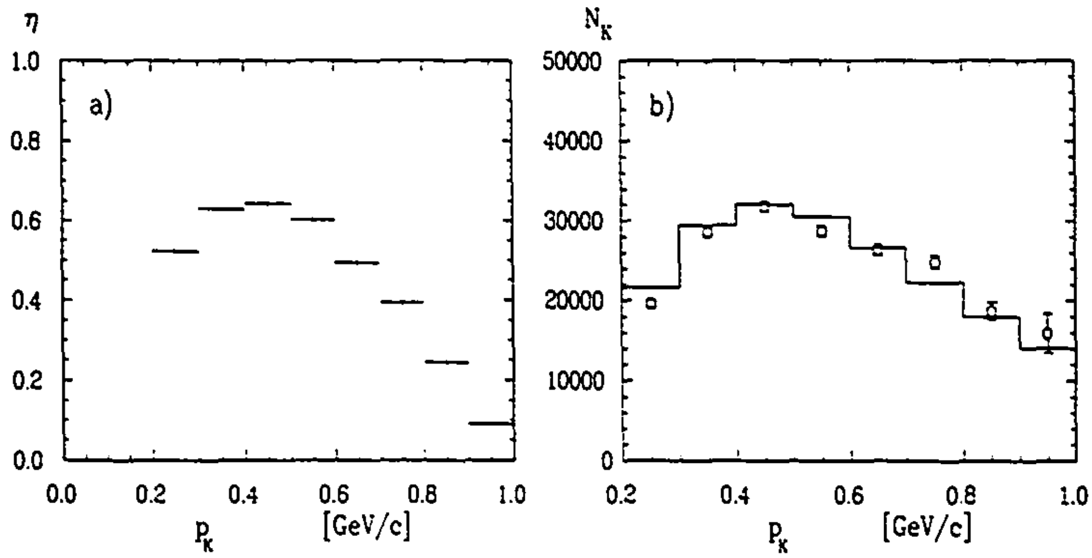

Figure 5.11: a) kaon efficiency derived using Monte Carlo simulation and b) comparison of the kaon momentum spectrum extracted from the data (points with error bars) and from the Monte Carlo simulation (histogram).

5.4 D^{*+} $K^{\pm}$ correlations

The number of D^{*+} $K^{\pm}$ pairs found in the decay of $B\bar{B}$ events is given by the following set of equations:

$$[N(D^{*+}K^+)]_{B^+B^-} = N^+_{++} = \\ (Br(B^+ \to D^{*+}) \cdot Br(B^+ \to K^-)) + (Br(B^+ \to D^{*-}) \cdot Br(B^+ \to K^+)) \quad (5.6)$$

$$[N(D^{*+}K^-)]_{B^+B^-} = N^+_{+-} = \\ (Br(B^+ \to D^{*+}) \cdot Br(B^+ \to K^+)) + (Br(B^+ \to D^{*-}) \cdot Br(B^+ \to K^-)) \quad (5.7)$$

$$[N(D^{*+}K^+)]_{B^0\bar{B}^0} = (1-\chi) \cdot N^0_{++} = \\ (1-\chi) \cdot [(Br(B^0 \to D^{*+}) \cdot Br(B^0 \to K^-)) + \\ (Br(B^0 \to D^{*-}) \cdot Br(B^0 \to K^+))] \quad (5.8)$$

$$[N(D^{*+}K^-)]_{B^0\bar{B}^0} = (1-\chi) \cdot N^0_{+-} = \\ (1-\chi) \cdot [(Br(B^0 \to D^{*+}) \cdot Br(B^0 \to K^+)) + \\ (Br(B^0 \to D^{*-}) \cdot Br(B^0 \to K^-))] \quad (5.9)$$

$$[N(D^{*+}K^+)]_{B^0B^0/\bar{B}^0\bar{B}^0} = \chi \cdot N^0_{+-} = \\ \chi \cdot [(Br(B^0 \to D^{*+}) \cdot Br(B^0 \to K^+)) + (Br(B^0 \to D^{*-}) \cdot Br(B^0 \to K^-))] \quad (5.10)$$

$$[N(D^{*+}K^-)]_{B^0B^0/\bar{B}^0\bar{B}^0} = \chi \cdot N^0_{++} = \\ \chi \cdot [(Br(B^0 \to D^{*+}) \cdot Br(B^0 \to K^-)) + (Br(B^0 \to D^{*-}) \cdot Br(B^0 \to K^+))]. \quad (5.11)$$

These give the ratio

$$\frac{N(D^{*+}K^-)}{N(D^{*+}K^+)} = \frac{N^+_{+-} + (1-\chi) \cdot N^0_{+-} + \chi \cdot N^0_{++}}{N^+_{++} + (1-\chi) \cdot N^0_{++} + \chi \cdot N^0_{+-}}, \quad (5.12)$$

or equivalently

$$\frac{N(D^{*+}K^{-})}{N(D^{*+}K^{+})+N(D^{*+}K^{-})}=\frac{(N^{+}_{+-}+N^{0}_{+-})\ +\ \chi\cdot(N^{0}_{++}-N^{0}_{+-})}{N^{+}_{++}+N^{+}_{+-}+N^{0}_{++}+N^{0}_{+-}}. \tag{5.13}$$

The quantities N^{+}_{++}, N^{+}_{+-}, N^{0}_{++}, and N^{0}_{+-}, which are the products of the branching ratios noted above, are all taken from Monte Carlo. The fact that there exists no measurement in B decays of the ratio of "wrong" to "right" charged D^* meson production, or of "wrong" to "right" charged kaon production, constitutes the major drawback of this method. One therefore has to rely on the Monte Carlo simulation. Using the values presented in Table 5.3 for these ratios, χ can be expressed as:

$$\chi\ =\ 2.568\cdot\frac{N(D^{*+}K^{-})/N(D^{*+}K^{+})}{1\ +\ N(D^{*+}K^{-})/N(D^{*+}K^{+})}\ -\ 0.625 \tag{5.14}$$

Events with a D^{*+} candidate are further required to have at least one kaon which has momentum $0.2 \leq p_K \leq 0.8\ GeV/c$ and a combined likelihood ratio for the kaon hypothesis, determined by dE/dx and TOF measurements (see Section 2.12.3), exceeding 80%. The kaon used to reconstruct the D^* candidate was not selected as a K candidate for B tagging.

The number $N(D^{*+}K^{\pm})$ is extracted by fitting the D^{*+} invariant mass distribution for events having a tagging kaon which fulfills the selection requirements noted above. The main background consists of D^{*+} $K^{\pm}$ combinations where both particles come from the same B meson. In Figure 5.12, the angle between the D^{*+} and the kaon is plotted for Monte Carlo generated B decays. If they are daughters of the same B meson, the D^* and kaon are mainly produced back-to-back. Therefore, a cut is applied to the angle, $cos\theta(D^{*+}K^{\pm}) > -0.5$, which results in an efficient suppression of this background.

After subtracting the continuum contribution, the invariant mass spectra shown in Figure 5.13 and 5.14 for the cases where the D^{*+} is reconstructed through the

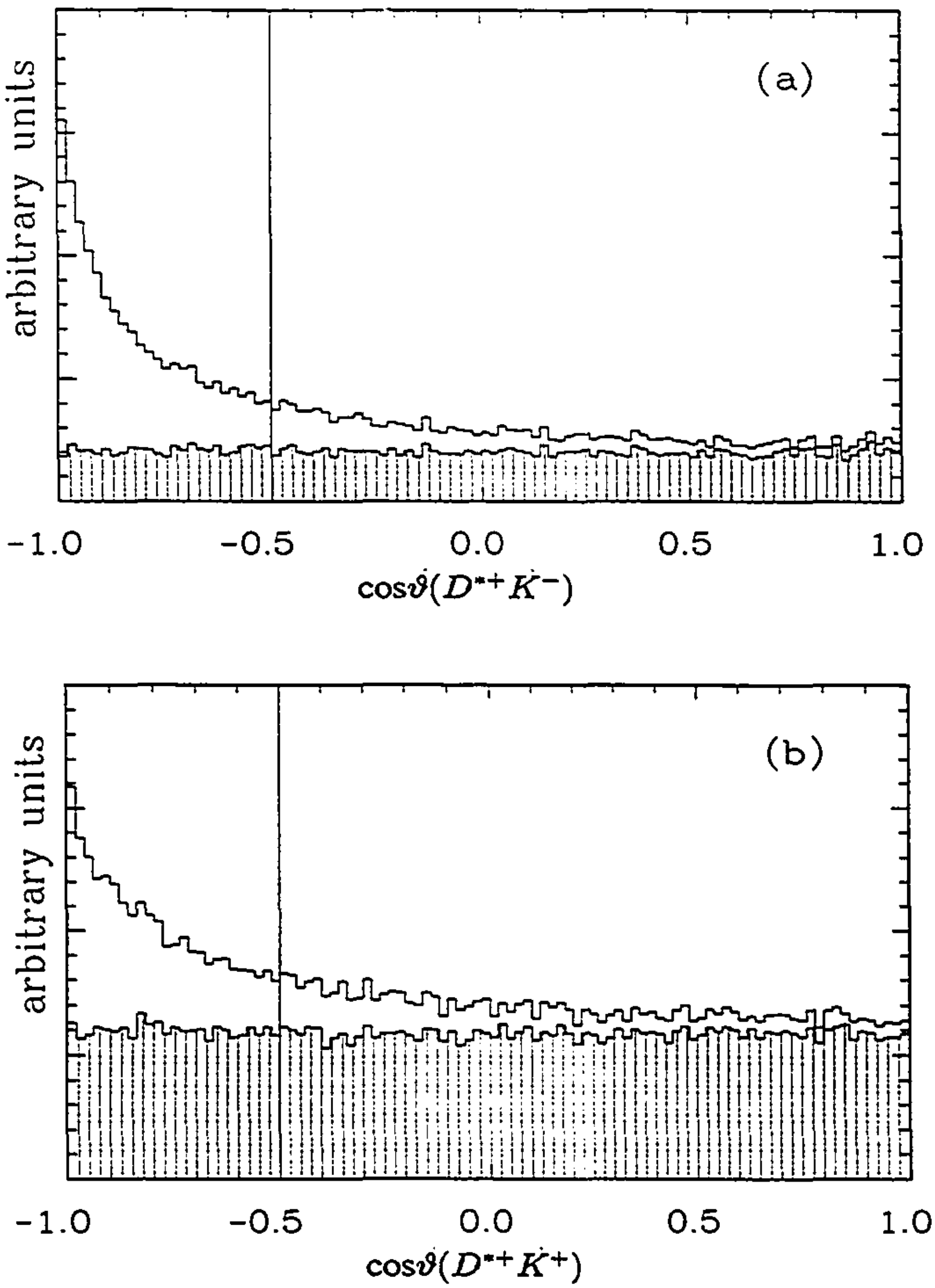

Figure 5.12: For $D^{*+}K^-$ (a) and for $D^{*+}K^+$ (b) combinations the angle between the D^{*+} and the K is shown for Monte Carlo generated events where all combinations (histogram) are considered and where only combinations for which the D^{*+} and the kaon come from different B mesons are taken (hatched histogram).

channels $D^0(\rightarrow K\pi)\pi$ and $D^0(\rightarrow K3\pi)\pi$, respectively are obtained. The spectra are fitted as described previously for the inclusive $\bar{B} \rightarrow D^{*+}X$; the width of the Gaussian used to describe the D^{*+} signal in the case of D^{*+} $K^{\pm}$ combinations is fixed to the width resulting from the fit of the inclusive D^{*+} signal.
The fit yielded

$$\begin{aligned} N_{D^{*+}K^-} &= 54 \pm 12 \\ N_{D^{*+}K^+} &= 116 \pm 15 \end{aligned} \tag{5.15}$$

when the D^{*+} is reconstructed in the decay channel (i) and

$$\begin{aligned} N_{D^{*+}K^-} &= 68 \pm 25 \\ N_{D^{*+}K^+} &= 132 \pm 27 \end{aligned} \tag{5.16}$$

when decay channel (ii) is used.

From these yields one has to subtract the contribution of events with a D^{*+} accompanied by a fake kaon. The hard likelihood cut applied on the kaon hypothesis guarantees that the fake rate is very low. For the momentum interval considered here, only $\pi - K$ misidentification needs to be taken into account. The $\pi - K$ fake rate was estimated using pions from K_s^0's with reconstructed secondary vertices and is shown in Figure 5.15 as a function of the momentum.

To find the number of pions which are misidentified as kaons, the mass spectrum of the D^* candidate is fitted when the D^* is accompanied by a pion and the fit is performed for different intervals of the π momentum. The numbers resulting from the fit are then multiplied by the fake rate for each momentum interval separately and the results are added to obtain the fake kaon contribution. When reconstructing the D^{*+} through decay channel (i)

$$N(D^{*+}\text{“}K\text{”}^-) = 1.1 \pm 0.1$$

$$N(D^{*+}\text{“}K\text{”}^+) = 0.8 \pm 0.1$$

are found and when reconstructing the D^{*+} through decay channel (ii) the fake kaon contribution is found to be:

$$N(D^{*+}\text{“}K\text{”}^-) = 0.4 \pm 0.2$$

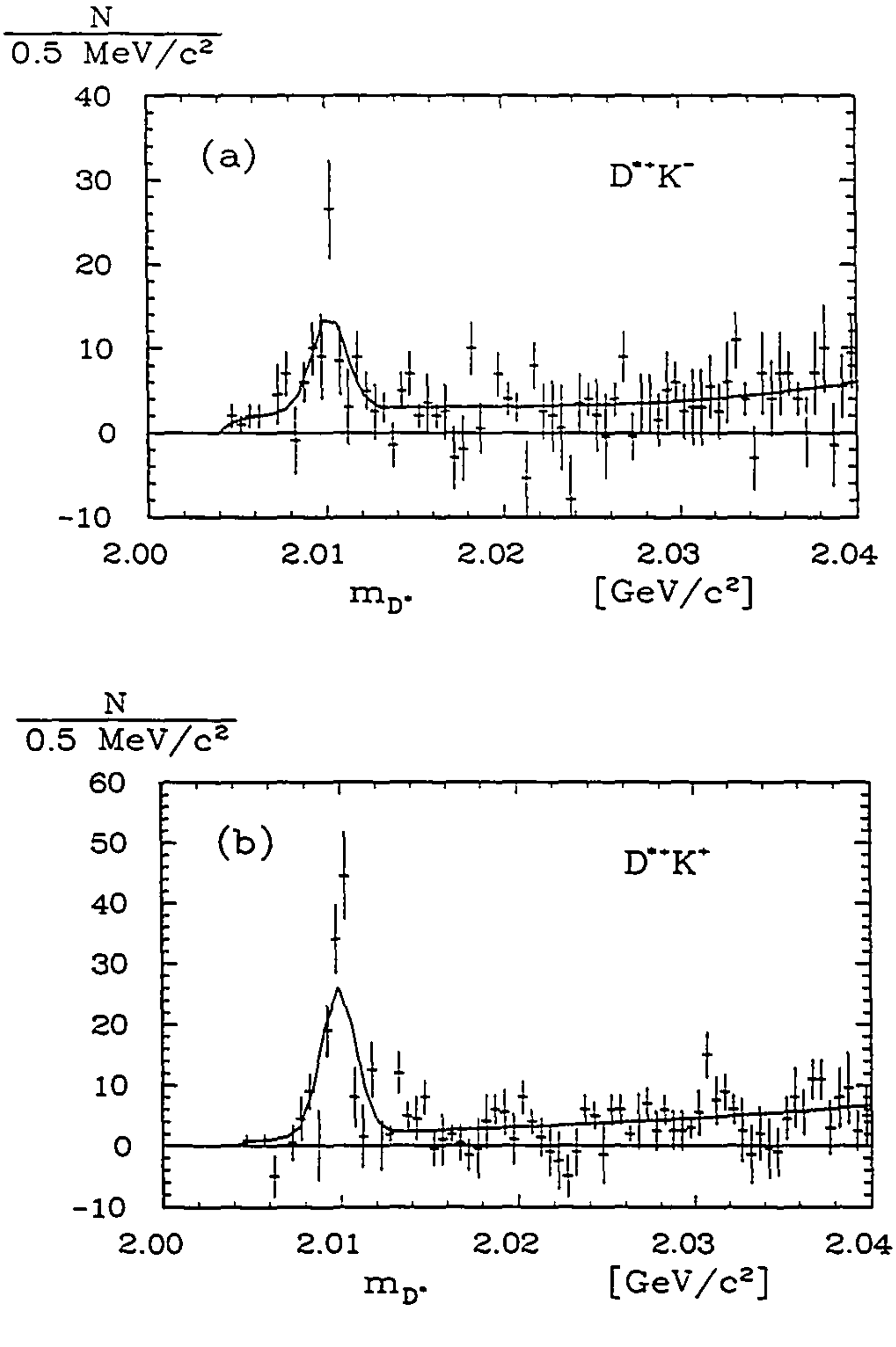

Figure 5.13: Invariant mass spectra for $D^0\pi^+$ combinations accompanied by a K^- (a) or by a K^+ (b). The D^0 is reconstructed through its $K\pi$ decay channel for continuum subtracted $\Upsilon(4S)$ events.

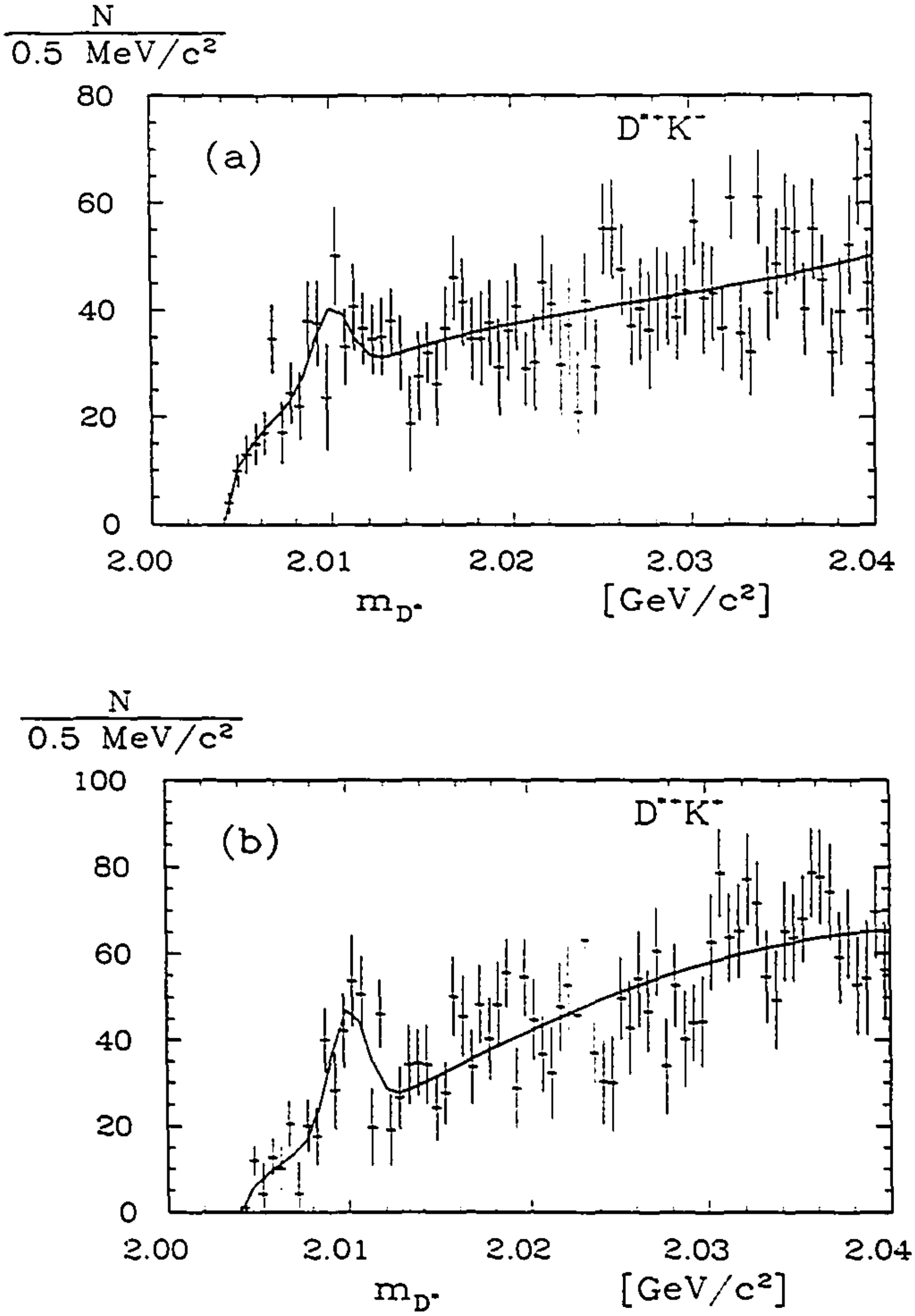

Figure 5.14: Invariant mass spectra for $D^0\pi^+$ combinations accompanied by a K^- (a) or by a K^+ (b). The D^0 was reconstructed from the $K3\pi$ for continuum subtracted $\Upsilon(4S)$ data.

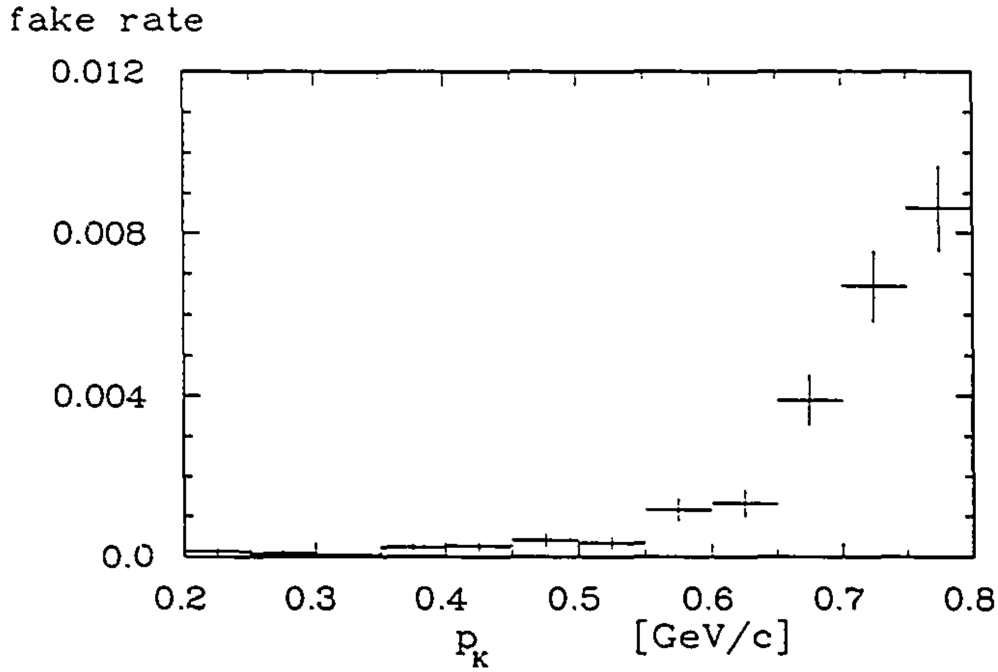

Figure 5.15: $\pi - K$ fake rate as a function of momentum.

$$N(D^{*+}\text{“}K\text{”}^{+}) = 0.3 \pm 0.1$$

After subtraction of the estimated fake kaon contribution, the D^{*+} yields quoted above transform to the following values for the ratio $N(D^{*+}K^-)/N(D^{*+}K^+)$:

$$\frac{N(D^{*+}K^-)}{N(D^{*+}K^+)} = 0.456 \pm 0.122 \tag{5.17}$$

when reconstructing the D^{*+} through decay channel (i) and

$$\frac{N(D^{*+}K^-)}{N(D^{*+}K^+)} = 0.515 \pm 0.216 \tag{5.18}$$

when decay channel (ii) is used for the D^{*+} reconstruction. Averaging these two values, the ratio obtained is:

$$\frac{N(D^{*+}K^-)}{N(D^{*+}K^+)} = 0.470 \pm 0.106 \tag{5.19}$$

which in turn, using equation 5.15, leads to the following value for χ:

$$\chi = 0.196 \pm 0.126. \tag{5.20}$$

The dependence of the result on the rate of the D^{*+} production from the virtual W, which produces D^* mesons with opposite charge to those originating from the b to c transition, was investigated. The extreme case of having no D^* production from the virtual W was considered. Hence, ignoring the "wrong" charge D^* production and re-calculating the $N(D^{*+}K^+/K^-)$ given by equations 5.6 - 5.11 leads to the following expression for the mixing parameter χ:

$$\chi = 2.024 \cdot \frac{N(D^{*+}K^-)/N(D^{*+}K^+)}{1 + N(D^{*+}K^-)/N(D^{*+}K^+)} - 0.449. \tag{5.21}$$

The mixing parameter χ resulting after putting the value found for the ratio $N(D^{*+}K^-)/N(D^{*+}K^+)$ in 5.21 is therefore

$$\chi = 0.268 \pm 0.110$$

5.4.1 Systematic errors

For the systematic error:

- the uncertainty in the description of the background was estimated to produce a contribution of 7.0%.
- the influence of the cut on the difference of the mass of the D^0 candidates from the nominal D^0 mass was studied. For this purpose, the cut was relaxed to 60 MeV/c^2 and 40 MeV/c^2 for the decays $D^0 \rightarrow K^-\pi^+$ and $D^0 \rightarrow K^-\pi^+\pi^+\pi^-$, respectively, and the procedure repeated. The contribution of this source to the systematic error is 0.5%.
- the dependence of the result on the branching ratio for the process $D^*_{(J)}$ was investigated. To account for the large uncertainty in the production ratio $\frac{D^{*\ spect}_{(J)}}{D^{*\ spect}}$, a conservative variation of 40% was allowed which resulted in a systematic error of 3.0%.

- the influence of a change in the values used for the branching ratios for the processes $(B^0, B^+ \rightarrow K^+X)$ and $(B^0, B^+ \rightarrow K^-X)$ was studied. There exists no information from experiment up to now on these individual branching ratios. As a check, the branching ratios for the processes $B \rightarrow D^{\pm}X$, $D^+ \rightarrow K^+X$, $D^+ \rightarrow K^-X$ and $B \rightarrow D^0, \bar{D}^0X$, $D^0 \rightarrow K^+X$, $D^0 \rightarrow K^-X$ obtained from Monte Carlo were compared with the ones reported in [2] and were found to be in good agreement. A change of 20% in these branching ratios was made to account for a 1σ variation of the product of branching ratios $Br(B \rightarrow D^+X) \cdot Br(D^+ \rightarrow K^+ \text{ .OR. } K^-X)$ and $Br(B \rightarrow D^0X) \cdot Br(D^0 \rightarrow K^+ \text{ .OR. } K^-X)$ and the results implied a systematic error of 3.9%.

- the contribution from D^{*+} mesons coming from the virtual W was investigated. For this purpose, the virtual $W^+ \rightarrow c\bar{s}$ decay rate was estimated using

$$Br(B \rightarrow D_s^+X) \;\cdot\; Br(D_s^+ \rightarrow \phi\pi^+) = (2.92 \pm 0.5) \cdot 10^{-3}$$

  reported in [22] and the value [2] $Br(D_s^+ \rightarrow \phi\pi^+) = (3.5 \pm 0.7)\%$. This results in $Br(B \rightarrow D_s^+X) = (8.3 \pm 2.2)\%$. Taking into account that the two body component of the decay $B \rightarrow D_s^+X$ resulting from the fit of the D_s x_p spectrum is $(58 \pm 11)\%$ [22], the probability for the decay $W^+ \rightarrow c\bar{s}s\bar{s}$ is expected to be $\sim 2\%$. To find the production rate for D^{*+} mesons from the virtual W the result needs to be multiplied by a factor $\eta_1 \sim 2.5$ to account for the rate for $d\bar{d}/s\bar{s}$ production from the vacuum and a factor $\eta_2 = V \;/\; (\; V \;+\; P\;) \sim 3/4$ to account for the formation of a D^{*+} meson(V and P stand for vector meson and pseudoscalar, respectively). The factors η_1 and η_2 are taken from the LUND fragmentation model [38]. This rough calculation results in $Br(W^+ \rightarrow D^{*+}\,X) \sim 3.7\%$. The value obtained from the Monte Carlo is $Br(W^+ \rightarrow D^{*+}\,X) = 2.4\%$. The ratio was accordingly varied within the bounds $1.1\% - 3.7\%$ and the results indicated a systematic error of 8.4%.

source	systematic error
background estimation and fitting procedure	7.0%
cut on the difference of the mass of the D^0 candidate from the nominal D^0 mass	0.5%
$\frac{D^{*\ spect}_{(J)}}{D^{*\ spect}}$ production ratio	3.0%
branching ratios for the processes $(B^0, B^+ \rightarrow K^+ .OR. K^- X)$	3.93%
contribution of the D^{*+} mesons originating from the virtual W	8.4%
total	12.0%

Table 5.8: Systematic errors for the determination of the mixing parameter χ.

The systematic errors are summarized in Table 5.8. The value obtained for the mixing parameter is therefore

$$\chi = 0.196 \pm 0.126 \text{ (stat) } \pm 0.120 \text{ (syst)}.$$

Chapter 6

Study of the $B^0\bar{B}^0$ mixing using $(D^*\ell)$ K correlations

6.1 Introduction

In this chapter the sample of $\bar{B}^0$ mesons provided by tagging in the $\bar{B}^0 \to D^{*+}\ell^-\bar{\nu}$ mode is again used to study $B^0\bar{B}^0$ mixing. This study is based on the same principle as the study presented in Chapter 4. To *tag* the flavour of one of the B mesons, the partial reconstruction technique introduced in Section 3.1 for studying the decay $\bar{B}^0 \to D^{*+}\ell^-\bar{\nu}$ is again used. However, where in the previous analysis the flavour of the other B meson was tagged using the charge of the lepton originating from the semileptonic B decay, here, in order to achieve a larger sample, the charge of the kaon coming from the $b \to c \to s$ decay is used. For this purpose, the kaon production rates in neutral B decays need to be exactly known. The use of the partial reconstruction of the $\bar{B}^0 \to D^{*+}\ell^-\bar{\nu}$ decay results in a larger background relative to the full reconstruction. However, as illustrated in Section 6.3, an efficient background description can be achieved allowing the extraction of a value for the mixing parameter. Hence, events containing $D^{*+}\ell^-$ and K^- provide a signature for mixing, as indicated in Table 6.1.

To achieve a large sample, the D^{*+} is not fully reconstructed; rather, the tech-

$B^0\bar{B}^0$ events	B^0B^0 or $\bar{B}^0\bar{B}^0$ events
$\left.\begin{array}{l}\bar{B}^0 \to D^{*+}\ell^-\bar{\nu} \\ B^0 \to K^+X\end{array}\right\} \Rightarrow D^{*+}\ell^-\ K^+$	$\left.\begin{array}{ll} & \bar{B}^0 \to D^{*+}\ell^-\bar{\nu} \\ B^0 \to & \bar{B}^0 \to K^-X\end{array}\right\} \Rightarrow D^{*+}\ell^-\ K^-$

Table 6.1: Signature for mixed/unmixed events in $D^*\ell$ K correlations.

nique already employed for tagging in the $\bar{B}^0 \to D^{*+}\ell^-\bar{\nu}$ mode, described in detail in Chapter 3, is again used. Here, as was explained in Chapter 4, only the first approach (A) introduced in Section 3.1 is used to parametrize the D^{*+} momentum because of the better resolution provided (see Figure 4.1).

6.2 $(D^*\ell)$ K correlations

To extract the mixing parameter using $(D^*\ell)K$ correlations the number of events with $(D^{*+}\ell^-)K^{\mp}$ needs to be calculated. This is done using a set of equations, as in the case of $D^{*+}K^{\pm}$ correlations:

$$[N((D^{*-}\ell^+)K^-)]_{B^+B^-} = [Br(B^+ \to D^{*-}\ell^+\nu X)\cdot Br(B^+ \to K^+)] \tag{6.1}$$

$$[N((D^{*-}\ell^+)K^+)]_{B^+B^-} = [Br(B^+ \to D^{*-}\ell^+\nu X)\cdot Br(B^+ \to K^-)] \tag{6.2}$$

$$[N((D^{*-}\ell^+)K^-)]_{B^0\bar{B}^0} = (1-\chi)\cdot\ [Br(B^0 \to D^{*-}\ell^+\nu X)\cdot Br(B^0 \to K^+)] \tag{6.3}$$

$$[N((D^{*-}\ell^+)K^+)]_{B^0\bar{B}^0} = (1-\chi)\cdot\ [Br(B^0 \to D^{*-}\ell^+\nu X)\cdot Br(B^0 \to K^-)] \tag{6.4}$$

$$[N((D^{*-}\ell^+)K^-)]_{B^0B^0/\bar{B}^0\bar{B}^0} = \chi\cdot\ [Br(B^0 \to D^{*-}\ell^+\nu X)\cdot Br(B^0 \to K^-)] \tag{6.5}$$

$$[N((D^{*-}\ell^+)K^+)]_{B^0B^0/\bar{B}^0\bar{B}^0} = \chi\cdot\ [Br(B^0 \to D^{*-}\ell^+\nu X)\cdot Br(B^0 \to K^+)]. \tag{6.6}$$

Taking into consideration that, according to isospin invariance,

$$\begin{aligned} 2 \cdot Br(\bar{B}^0 \to D^{**+}\ell^-\bar{\nu}) \cdot Br(D^{**+} \to D^{*+}\pi^0) &= \\ Br(B^- \to D^{**0}\ell^-\bar{\nu}) \cdot Br(D^{**0} \to D^{*+}\pi^-), \end{aligned}$$

the above relations become:

$$\begin{aligned} N((D^{*-}\ell^+)K^+) &= [(1-\chi)\cdot Br(B^0 \to K^-) + \chi \cdot Br(B^0 \to K^+)] \cdot N_{D^{*-},} \\ &+ [2/3 \cdot Br(B^+ \to K^-) + (1-\chi)\cdot 1/3 \cdot Br(B^0 \to K^-) + \\ &\chi \cdot 1/3 \cdot Br(B^0 \to K^+)] \cdot N_{D^*_J,} \quad (6.7) \end{aligned}$$

and

$$\begin{aligned} N((D^{*-}\ell^+)K^-) &= [(1-\chi)\cdot Br(B^0 \to K^+) + \chi \cdot Br(B^0 \to K^-)] \cdot N_{D^{*-},} \\ &+ [2/3 \cdot Br(B^+ \to K^+) + (1-\chi)\cdot 1/3 \cdot Br(B^0 \to K^+) + \\ &\chi \cdot 1/3 \cdot Br(B^0 \to K^-)] \cdot N_{D^*_J,} \quad (6.8) \end{aligned}$$

thus leading to the ratio

$$\frac{N((D^{*-}\ell^+)\ K^+)}{N((D^{*-}\ell^+)\ K^+) + N((D^{*-}\ell^+)\ K^-)} =$$

$$\frac{[(1-\chi)\cdot Br(B^0 \to K^-) + \chi \cdot Br(B^0 \to K^+)]}{Br(B^0 \to K^\pm)}. \quad (6.9)$$

Using the values presented in Table 6.2 for the branching ratios $(B \to K^\pm X)$, χ is given by:

$$\chi = (1.714 \pm 0.012) \cdot \frac{N((D^{*-}\ell^+)\ K^+)/N((D^{*-}\ell^+)\ K^-)}{1 + N((D^{*-}\ell^+)\ K^+)/N((D^{*-}\ell^+)\ K^-)} - (0.357 \pm 0.003).$$

6.3 Measurement of the $B^0\bar{B}^0$ mixing parameter

In order to reconstruct a B^0 meson in the decay mode $B^0 \to D^{*-}\ell^+\nu$, a lepton and a pion which fulfill the criteria described in Sections 3.3 and 3.4 are selected. An additional tagging kaon with momentum $0.2 \leq p_K \leq 0.8$ GeV/c and combined likelihood ratio for the kaon hypothesis (see Section 2.12.3) exceeding 80% is required.

To extract the mixing parameter χ, the M^2_{recoil} distribution for $\pi^+ - \ell^-$ combinations was studied. The observed M^2_{recoil} spectra are shown in Figure 6.1. The estimated background contribution (extracted using $(\pi^+ - \ell^+)K^\pm$ combinations) is also shown.

The peak at recoil masses $M^2_{rec} > -2.0$ GeV^2/c^4 contains contributions from the following sources.

(I) $\bar{B}^0_1 \rightarrow D^{*+}\ell^-\bar{\nu}$ and $B^0_2 \rightarrow K^+/K^-X$

(II) $\bar{B}^0_1 \longrightarrow D^{*+}_J\ell^-\bar{\nu}$ and $B^0_2 \rightarrow K^+/K^-X$

$\quad\hookrightarrow D^{*+}\pi^0$

(III) $\bar{B}^0_1 \longrightarrow D^{*+}\ell^-\bar{\nu}X$ and $B^0_2 \rightarrow$ anything

$\quad\hookrightarrow D^0\pi^+$

$\quad\quad\hookrightarrow K^+/K^-X$

(IV) $B^-_1 \longrightarrow D^{*0}_J\ell^-\bar{\nu}$ and $B^+_2 \rightarrow K^+/K^-X$

$\quad\hookrightarrow D^{*+}\pi^-$

(V) $B^-_1 \longrightarrow D^{*0}_J\ell^-\bar{\nu}$ and $B^+_2 \rightarrow$ anything

$\quad\hookrightarrow D^{*+}\pi^-$

$\quad\quad\hookrightarrow D^0\pi^0$

$\quad\quad\quad\hookrightarrow K^+/K^-X$

Care must be taken in determining the number of events with

$$\bar{B}^0_1 \rightarrow D^{*+}\ell^-\bar{\nu} \quad \text{and} \quad B^0_2 \rightarrow KX,$$

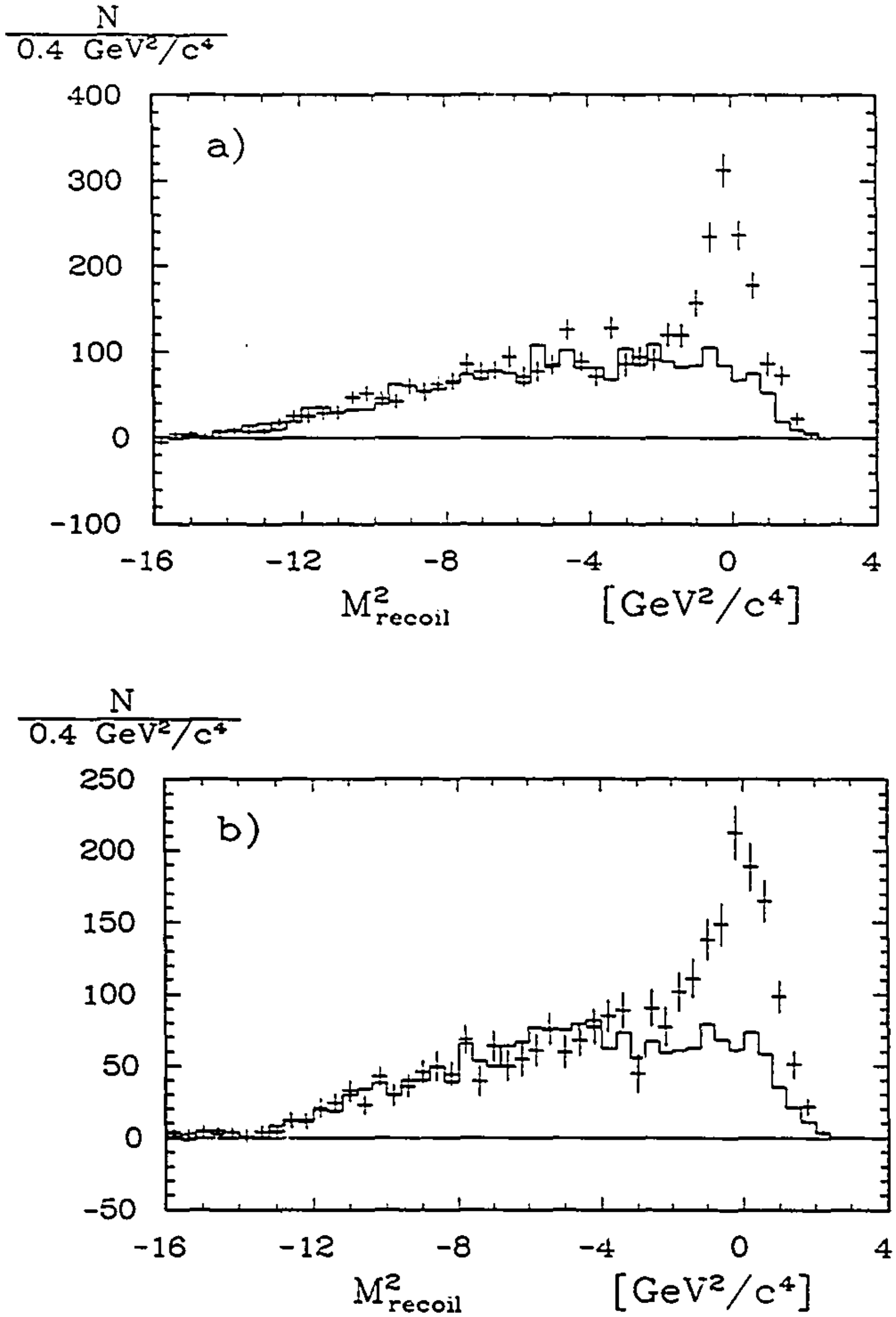

Figure 6.1: M^2_{recoil} spectra for $\pi^+ - \ell^-$ combinations a) accompanied with a K^-, and b) accompanied with a K^+. The expected background contribution estimated using $(\pi^+ - \ell^+)K^\pm$ combinations is also indicated.

Decay mode	a) Branching ratio [2]	b) Branching ratio [69]
$Br(D^0 \to K^- X)$	$(53 \pm 4)\%$	$(60.9 \pm 3.2 \pm 5.2)\%$
$Br(D^0 \to K^+ X)$	$(3.4^{+0.6}_{-0.4})\%$	$(2.8 \pm 0.9 \pm 0.4)\%$

Table 6.2: Measurements of $Br(D^0 \to KX)$.

because, as indicated in Table 5.3, the branching ratios for the decays $D^0 \to K^+/K^-\ X$ and $D^+ \to K^+/K^-\ X$ are different. The contribution to the D^{*+} yield from background (III) is:

$$\begin{aligned} & N(\bar{B}^0 \to \ell^- \bar{\nu} D^{*+}(D^{*+} \to \pi^+ D^0)(D^0 \to K^+ \text{ .OR. } K^- X)) \\ = \ & N_{D^{*+}_{fit}} \cdot (Br(D^0 \to K^+ X) \text{ .OR. } Br(D^0 \to K^- X) \cdot \eta_K, \end{aligned} \tag{6.10}$$

where $N_{D^{*+}_{fit}}$ is the number of D^{*+} 's resulting from the fit shown in Figure 3.7. The kaon efficiency for the cuts mentioned above, η_K, is estimated with Monte Carlo simulation to be $\eta_K = 0.365 \pm 0.001$, where the error is statistical. The contribution from backgrounds (III) and (V) to the $D^*_{(J)}$ yield can be estimated in a similar way. The current values for $Br(D^0 \to KX)$ are presented in Table 6.2 a) where the values taken from the PDG [2] are displayed and b) where the latest results from the MARK III Collaboration [69] values are quoted.

From Table 6.2 it is clear that the number of events with $(\pi^+ - \ell^-)K^-$ coming from the processes (III) and (V), as calculated using equation 6.10, will produce a large systematic uncertainty since this number strongly depends on the value assumed for $Br(D^0 \to KX)$. Contribution from events arising from processes (III) and (V) cannot be estimated reliably. To suppress these events, a cut on the angle between the π and the selected K is applied. For "$(\pi^+ - \ell^-)K$" combinations where both the pion and the kaon are daughter particles of the same D^{*+} meson, the angle $\theta(\pi - K)$ has a pronounced peak at $cos\theta \sim 1$, as shown in Figure 6.2; while in the case where π and K are daughters of different B mesons this angle is flat as expected. Monte Carlo studies show that only about 30% of the kaons arising from processes (III) and (V) which contribute to the "mixed" event signal lie in the interval $cos\theta(\pi - K) < 0.5$. Therefore requiring events with $cos\theta(\pi, K) < 0.5$ results in a significant reduction of this background.

The recoil mass spectra obtained when the requirement $cos\theta(\pi, K) < 0.5$ is made are shown in Figure 6.4.

Using Monte Carlo simulation, the shape of the uncorrelated background for $(\pi^+ - \ell^-)$ accompanied by a K^-/K^+ was compared with the recoil mass distribution obtained for wrong-charge combinations $(\pi^+ - \ell^+)K^-/K^+$. By this means it was found that $(\pi^+ - \ell^+)K^-$ and $(\pi^+ - \ell^+)K^+$ combinaticns provide a good description of the shape of the uncorrelated background for the $(\pi^+ - \ell^-)K^-$ and $(\pi^+ - \ell^-)K^+$ samples respectively, as also shown in Figure 6.3.

To fit the signal observed in the recoil mass spectra of Figure 6.4 one needs to re-consider equations 6.7 and 6.8, keeping in mind that even though background arising from sources (III) and (V) is significantly reduced, the relative contribution of this background to the D^{*+} and $D^*_{(J)}$ cannot be neglected. Assuming $Br(B^+ \rightarrow K^-) = Br(B^0 \rightarrow K^-)$ and noting that the contribution from background sources (III) and (V) depends on the sum

$$Br(B^0 \rightarrow D^{*-}\ell^+\nu X) + Br(B^+ \rightarrow D^{*-}\ell^+\nu X),$$

$N((D^{*-}\ell^+)K^+)$ can be obtained by fitting the recoil mass spectrum with a combination of D^{*+} and $D^*_{(J)}$ channels where the relative contributions of D^*_J and D^{*+} to the spectra are fixed from the one lepton case (Section 3.4).

For $N((D^{*-}\ell^+)K^-)$ however, one must account for the fact that $Br(B^+ \rightarrow K^+) \neq Br(B^0 \rightarrow K^+)$. The contribution from the term which depends on $Br(B^+ \rightarrow K^+)$ can be estimated, given that it does not depend on the mixing parameter, from

$$N[(B_1^+ \rightarrow D^{*-}\ell^+\nu X)(B_2^- \rightarrow K^-X)] = 2/3 \cdot N_{D^*_{(J)_{8t}}} \cdot Br(B^- \rightarrow K^-X) \cdot \eta_K,$$

where $N_{D^*_{(J)_{8t}}}$ is the number of $N_{D^*_{(J)}}$ resulting from the fit shown in Figure 3.7 for $\bar{B}^0 \rightarrow D^{*+}\ell^-\bar{\nu}$. Multiplying by an additional factor of 3/4 to account for the angular

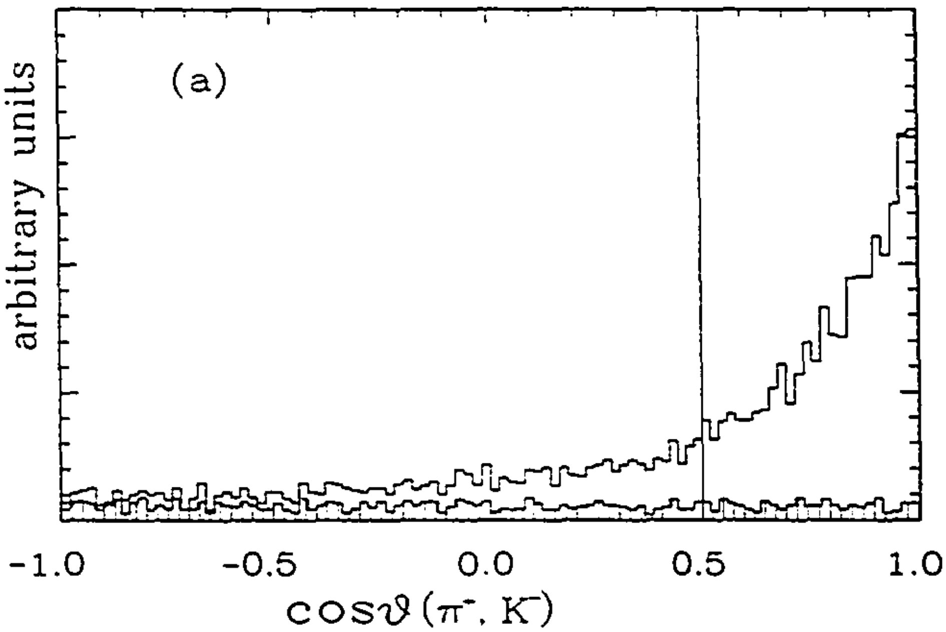

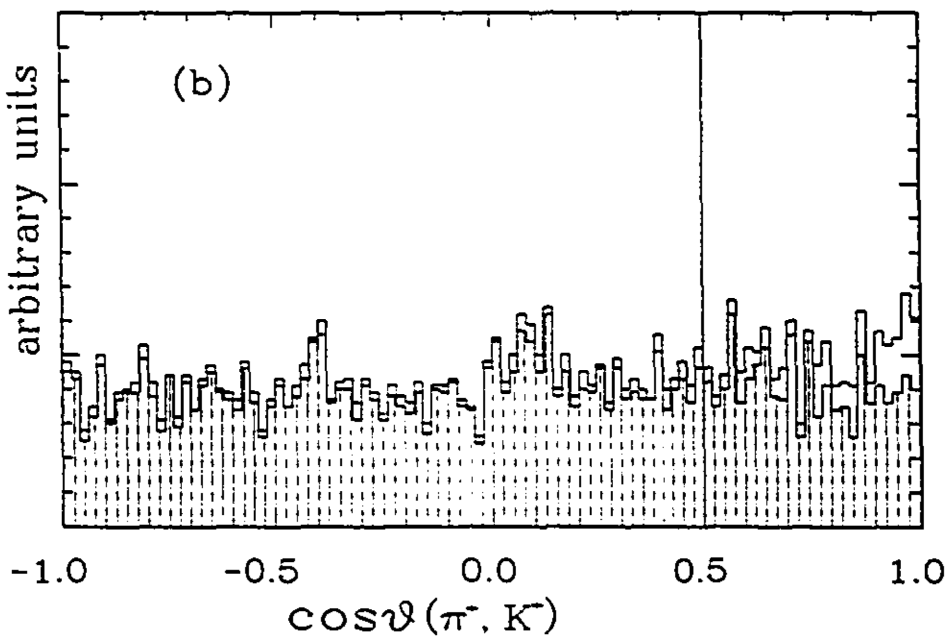

Figure 6.2: For (a) $(\pi^+ - \ell^-)K^-$ and for (b) $(\pi^+ - \ell^-)K^+$ combinations, the angle $\theta(\pi, K)$ is plotted for Monte Carlo generated events taking all π,K combinations (histogram), and taking only those π,K combinations for which the two particles are not daughters of the same D^{*+} meson (hatched histogram).

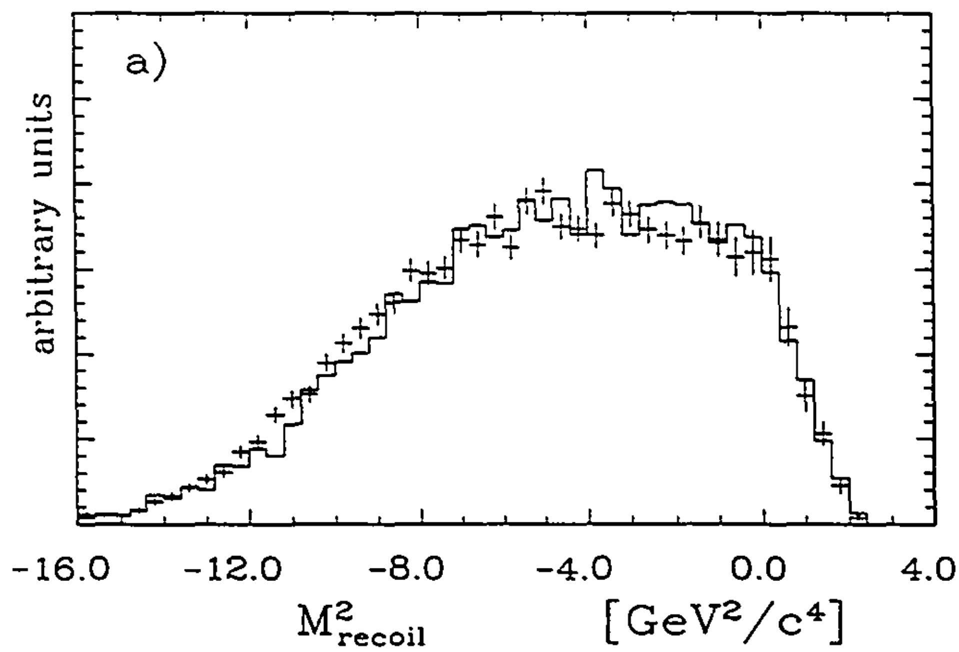

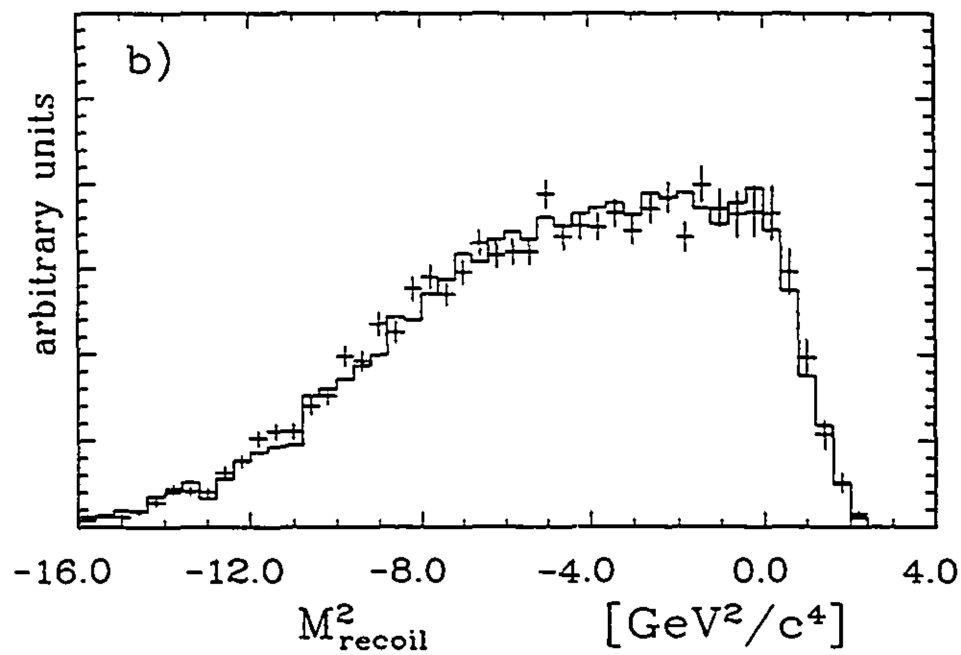

Figure 6.3: M^2_{recoil} spectra for uncorrelated "right-sign" $(\ell^\pm - \pi^\mp)$ combinations accompanied by $K^\pm$ (points with error bars) and normalized "wrong-sign" $(\ell^\pm - \pi^\pm)$ combinations also accompanied by a $K^\pm$ (histogram), both obtained from Monte Carlo simulation. a) and b) correspond to the cases $(\ell^+ - \pi^-)K^+$ and $(\ell^+ - \pi^-)K^-$, respectively.

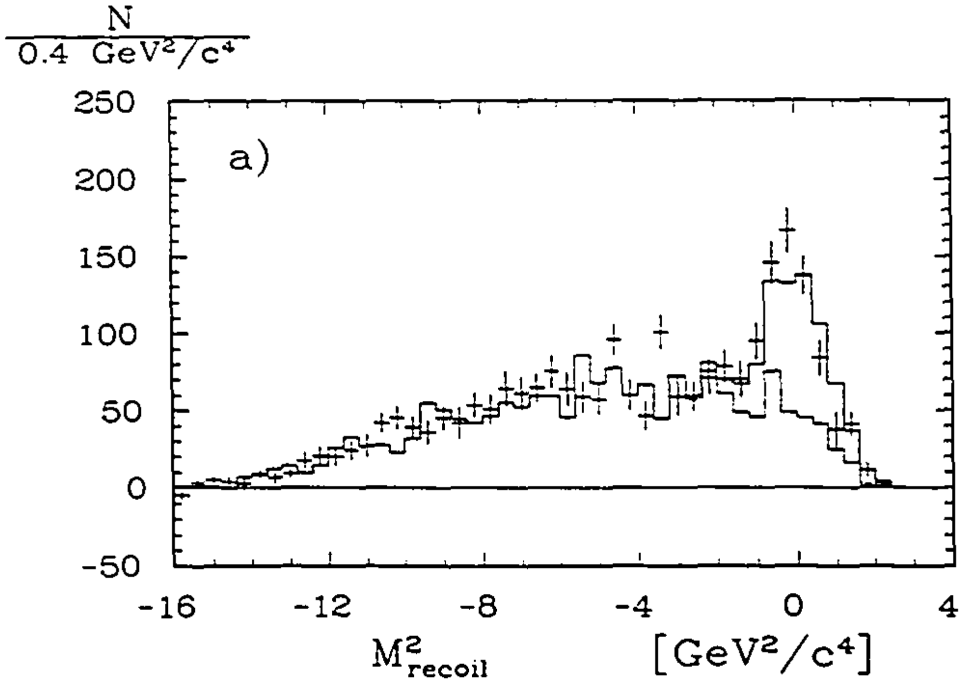

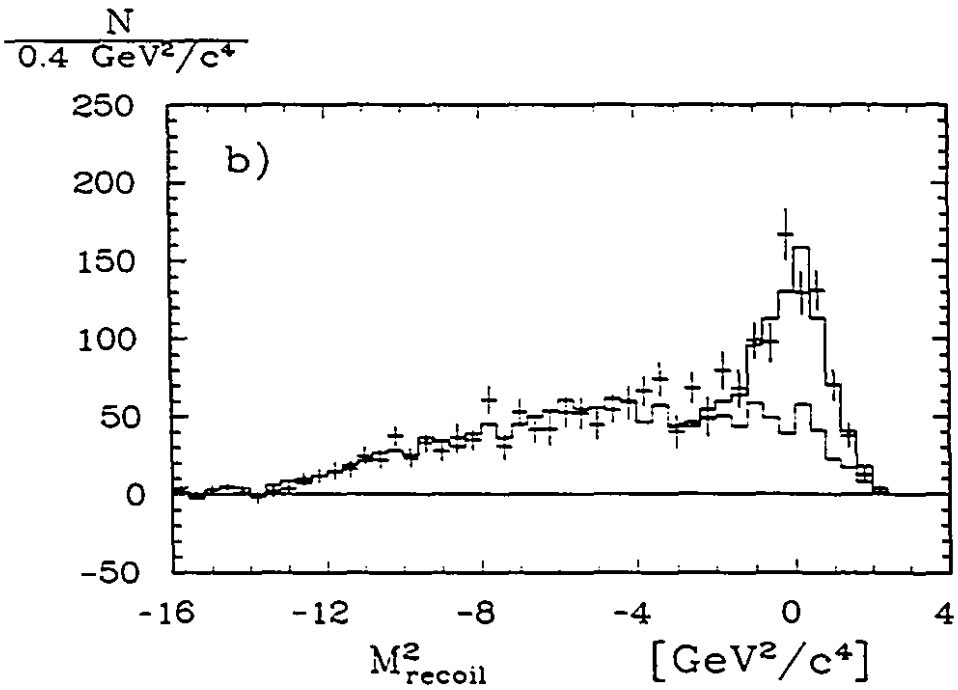

Figure 6.4: M^2_{recoil} spectra for $\pi^+ - \ell^-$ combinations a) accompanied by a K^-, and b) accompanied by a K^+. The expected background contribution estimated using$(\pi^+ - \ell^+)K$ combinations is also indicated.

cut applied, this contribution is found to be 58 ± 13 events. The normalization of the M^2_{recoil} spectrum for the $D^*_{(J)}$ channel is then fixed at this value in the fitting algorithm. The background from sources (III) and (V) is here very small, as it depends on $Br(D^0 \to K^+X)$, so its relative contribution to the D^{*+} and $D^*_{(J)}$ channels need not be taken into account when constructing the fitting algorithm. The recoil mass spectrum for $(D^{*-}\ell^+)K^-$ combinations is therefore fit with the estimated $Br(B^+ \to K^+)$ contribution and the M^2_{recoil} spectrum for the D^{*+} and $D^*_{(J)_{B^0}}$ channels with the relative contributions of $D^*_{J_{B^0}}$ and D^{*+} fixed from the one lepton case.

The fit yielded for $\bar{B}^0_1 \to D^{*+}\ell^-\bar{\nu}$:

$$\begin{aligned} N\left((\ell^\pm - \pi^\mp)\ K^\pm\right) &= 380 \pm 31 \\ N\left((\ell^\pm - \pi^\mp)\ K^\mp\right) &= 412 \pm 37. \end{aligned} \tag{6.11}$$

The numbers quoted here are valid only for the D^{*+} channel. To estimate the number of pions which are misidentified as kaons, the recoil mass spectrum for $(\ell^\pm - \pi^\mp)$ combinations accompanied by a pion was used for different intervals of the π momentum. The numbers resulting from the fit are then multiplied with the fake rate for each momentum interval separately and the results summed to give the fake kaon contribution, which is found to be:

$$\begin{aligned} N\left((\ell^\pm - \pi^\mp)\ \text{“}K\text{”}^\pm\right) &= 3.7 \pm 0.3 \\ N\left((\ell^\pm - \pi^\mp)\ \text{“}K\text{”}^\mp\right) &= 3.0 \pm 0.3. \end{aligned}$$

The electron fakes $(h^+\pi^-)K^\pm$ were also studied by taking right and wrong-sign $(h-\pi)$ combinations, where the hadron momentum was required to lie in the interval $1.4 \leq p_h \leq 2.5\ GeV/c$, along with an additional kaon which has to fulfill the tagging kaon requirements already mentioned. The M^2_{recoil} distributions for the right and wrong-sign $(h - \pi)K$ cases were found to be the same, as expected, implying that these cases are already accounted for in the uncorrelated background.

After subtraction of the fake kaon contribution, the number of $((\ell^+ - \pi^-)\ K^\pm)$ is:

$$\begin{aligned} N\left((\ell^\pm - \pi^\mp)\ K^\pm\right) &= 376 \pm 31 \\ N\left((\ell^\pm - \pi^\mp)\ K^\mp\right) &= 409 \pm 37. \end{aligned} \tag{6.12}$$

These results, however, still contain background due to processes (III) and (V), i.e. events where the π and the K are daughters of the same D^* meson. Monte Carlo shows that for the samples $((\ell^\pm - \pi^\mp)\ K^\pm)$ and $((\ell^\pm - \pi^\mp)\ K^\mp)$, 32% and 49% of the events respectively still contain both a π and K which originate from the same D^* meson, despite the angle requirement $cos\theta(\pi, K) < 0.5$. The contribution from these events to the signal has to be estimated and then removed. Using equation 6.10 with $\eta_K = 0.365 \pm 0.001$ and $N_{D^{*+}_{\rm fit}} = 2705 \pm 161.5$, one finds that

$$
\begin{aligned}
&N(\bar{B}^0 \to \ell^- \bar{\nu} D^{*+}(D^{*+} \to \pi^+ D^0)(D^0 \to K^+ X)) \cdot 0.32 \\
&\qquad = (601 \pm 36) \cdot 0.32 = 192 \pm 12
\end{aligned}
$$

background events from the decay process (III) contribute to N $((\ell^\pm - \pi^\mp)\ K^\pm)$ and

$$
\begin{aligned}
&N(\bar{B}^0 \to \ell^- \bar{\nu} D^{*+}(D^{*+} \to \pi^+ D^0)(D^0 \to K^- X)) \cdot 0.49 \\
&\qquad = (28 \pm 2) \cdot 0.49 = 14 \pm 1
\end{aligned}
$$

background events from the decay process (III) contribute to N $((\ell^\pm - \pi^\mp)\ K^\mp)$. Here, MARK III [69] values are used for the $Br(D^0 \to K^+/K^- X)$. After subtracting the estimated background contribution, the yields for $\bar{B}^0_1 \to D^{*+}\ell^-\bar{\nu}$ become:

$$
\begin{aligned}
N\ ((\ell^\pm - \pi^\mp)\ K^\pm) &= 184 \pm 33 \\
N\ ((\ell^\pm - \pi^\mp)\ K^\mp) &= 395 \pm 37
\end{aligned}
\tag{6.13}
$$

giving the ratio

$$
\frac{N((\ell^+ - \pi^-)\ K^+)}{N((\ell^+ - \pi^-)\ K^-)} = 0.466 \pm 0.094 \tag{6.14}
$$

which in turn, using equation 6.9, transforms to the following value for χ:

$$
\chi = 0.188 \pm 0.075. \tag{6.15}
$$

Using the values reported in [2] for the $Br(D^0 \to K^\pm X)$ the value obtained for χ becomes:

$$
\chi = 0.238 \pm 0.071. \tag{6.16}
$$

As a consistency check the $Br(B^0 \to K^\pm X)$ can be estimated:

$$Br(B^0 \to K^\pm X) = \frac{N((\ell^+ - \pi^-)\ K^\pm) \cdot (4/3)}{N(\ell^+ - \pi^-) \cdot \eta_K}, \tag{6.17}$$

where the factor 4/3 is used to account for the angular cut applied and where $N(\ell^+ - \pi^-) = N_{D^{*+}_{st}}$. Substituting $N((\ell^+ - \pi^-)\ K^\pm) = 579 \pm 50$ into the above equation the value obtained for $Br(B^0 \to K^\pm X)$ is

$$Br(B^0 \to K^\pm X) = (78.2 \pm 8.2)\%. \tag{6.18}$$

6.3.1 Systematic errors

The main contribution to the systematic error arises from the branching ratios for the processes $(B \to K^+X)$ and $(B \to K^-X)$ which are taken from Monte Carlo. Since kaons mostly originate from the decay of D mesons, the branching ratios

$$Br(B \to D^\pm X) \cdot [Br(D^+ \to K^+X)\ .\mathrm{OR.}\ Br(D^+ \to K^-X)]$$

and

$$Br(B \to D^0/\bar{D}^0 X) \cdot [Br(D^0 \to K^+X)\ .\mathrm{OR.}\ Br(D^0 \to K^-X)]$$

obtained from Monte Carlo were compared with the values reported in [2] and found to be in good agreement. The same holds for the $B \to K^\pm X$ branching ratio. In order to account for the lack of knowledge of the separate branching ratios, i.e. $Br(B^0 \to K^+X)$, $Br(B^0 \to K^-X)$, $Br(B^+ \to K^+X)$, and $Br(B^+ \to K^-X)$, a large error was assigned to these values.

For the systematic error:

- the influence of a change on the values used for the branching ratio for the process $(B^0, B^+ \to K^+X)$ and $(B^0, B^+ \to K^-X)$ was studied. A change of 20% on these branching ratios was made which resulted in a systematic error of 4.9%.

source	systematic error
branching ratio for the process	
$(B^0, B^+ \rightarrow K^+ .\mathrm{OR}.K^- X)$	4.9%
$\frac{D^*_{(J)}}{D^*}$ ratio	2.2%
$cos\theta(\pi, K)$ cut	3.0%
background estimation	
and fitting procedure	3.3%
total	6.9%

Table 6.3: Systematic errors for the determination of the mixing parameter χ.

- the $\frac{D^*_{(J)}}{D^*}$ ratio used in the fitting procedure was changed to 22.0% which is the value reported in [58] corresponding to $p_\ell \geq 1.4\ GeV/c$ for the momentum of the lepton that accompanies the D^* in the $B \rightarrow D^*_{(J)}\ell\nu$ decay mode. This resulted in a contribution of 2.2% to the systematic error.

- the dependence of the result on the angular cut applied was checked. For this purpose, this cut was changed to $cos\theta(\pi, K) < 0.3$ and to $cos\theta(\pi, K) < 0.7$ and the systematic error arising from this source found to be 3.0%.

- the variation of the result due to the background estimation and the fitting procedure was studied. This source contributes an additional 3.3% to the systematic error.

The systematic errors are summarized in Table 6.3.

The value obtained for the mixing parameter χ is therefore

$$\chi \ = \ 0.188 \pm 0.075 \pm 0.069 \pm 0.050 \tag{6.19}$$

where the last error accounts for the uncertainty on the branching ratio for the processes $D^0 \rightarrow K^\pm X$.

Chapter 7

Discussion of the results

In this section, the measurement of the mixing parameter χ_d is further used to extract information on the CKM matrix element V_{td} and on the mixing of the B_s system. At the end, an overview of the experimental results described in this work is presented.

7.1 Implications of the measurement of χ_d

The measurements of χ_d obtained by tagging one of the B^0 mesons in the decay $\bar{B}^0 \to D^{*+}\ell^-\bar{\nu}$ are averaged according to [77]. The resulting value for χ_d is:

$$\chi_d = 0.165 \pm 0.057.$$

The measurement performed by investigating $D^{*+}K^{\pm}$ correlations is not considered because of the small statistical significance of the result.

Using the relation

$$\chi_d = \frac{1}{2}\frac{x_d^2}{1+x_d^2},$$

the value extracted for the mixing parameter χ_d can be converted to x_d

$$x_d^2 = \frac{2\chi_d}{1-2\chi_d}.$$

Inserting $\chi_d = 0.165 \pm 0.057$ into the above equation, the mixing x_d is determined

$$x_d = 0.703 \pm 0.180 \tag{7.1}$$

where the error quoted is found by adding the statistical and systematic errors in quadrature. Use of the mixing result 7.1 can further constrain the parameters of the quark mixing matrix V_{CKM} (see Section 1.1.1) involving the top quark. As shown in Section 1.5, calculation of the $B_d^0 - \bar{B}_d^0$ box diagram gives

$$x_d = \frac{\Delta M}{\Gamma} = \frac{G_F^2}{6\pi^2}\, m_{B_d}\, \tau_{B_d}\, (B_d f_{B_d}^2) |V_{tb}^* V_{td}|^2\, m_t^2 F(\frac{m_t^2}{M_W^2})\, \eta_{QCD} \tag{7.2}$$

This formula has been used in the past to provide limits on the *top* quark mass. However, an indirect prediction for m_t now exists, based on SM fits of the electroweak parameters, has been made using the LEP data [82] and recently the top quark mass has been directly determined by the CDF Collaboration, so that an attempt can be made to extract the CKM matrix element V_{td} instead. For this purpose, the following values will be used

- for the B_d^0 meson lifetime $\tau_{B_d} = 1.5 \pm 0.11 ps$ [2]
- for the mass of the B_d^0 meson $m_{B_d} = 5279.0 \pm 2.0$ MeV [2]
- for the top quark mass $m_t = 174 \pm 17 GeV$ from the CDF Collaboration [76]
- for the QCD correction $\eta_{QCD} = 0.55$ from ref. [78], where this correction is analysed including the effects of a heavy t-quark.
- for the "bag" parameter and the decay constant B_d and f_{B_d} respectively the product $B_d \cdot f_{B_d}^2 = (1.0 \pm 0.2) \cdot (180 \pm 50\ MeV)^2$ is taken from [70]
- and $V_{tb} \simeq 1$ from unitarity.

Equation 7.2 then provides the matrix element V_{td}

$$V_{td} = (0.93 \pm 0.31) \cdot 10^{-2}, \tag{7.3}$$

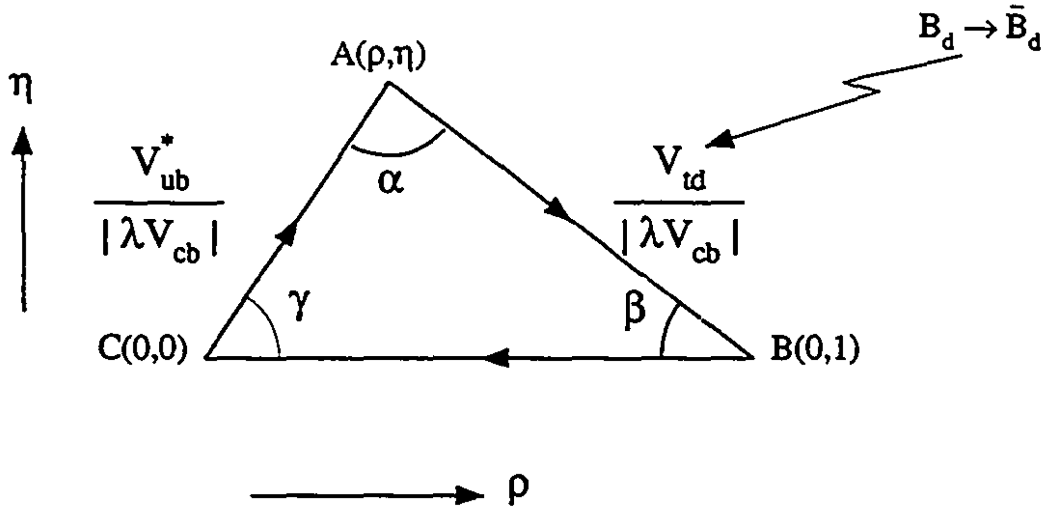

Figure 7.1: The unitarity triangle. ρ, η and λ are defined in the Wolfenstein parametrization (equation 1.8) of the CKM matrix.

where the contribution of the different sources to the error is given in the following equation:

$$V_{td} = (0.93 \pm 0.12(x_d) \pm 0.11(m_t) \pm 0.26(f_B) \pm 0.034(\tau_B)) \cdot 10^{-2}$$

The CKM matrix elements obey unitarity constraints, according to which any pair of rows (columns) of the matrix are orthogonal. Hence, the following relation is obtained:

$$V_{ud}V_{ub}^* + V_{cd}V_{cb}^* + V_{td}V_{tb}^* = 0. \tag{7.4}$$

Using the form of the CKM matrix in equation 1.7, the above relation can be written as:

$$\frac{V_{ub}^*}{\lambda V_{cb}} + \frac{V_{td}}{\lambda V_{cb}} = 1, \tag{7.5}$$

which is a triangle relation in the complex plane. This so-called "unitarity triangle" is illustrated in Figure 7.1 and demonstrates the allowed region in the $\rho - \eta$ space.

Using equation 7.5 one can obtain limits for the CKM matrix element V_{td} which in turn can be used to give an experimental value for the product $B_d \cdot f_{B_d}^2$. For this purpose, the CKM matrix elements V_{ub}^* and V_{td} are re-written as:

$$V_{ub}^* = A\lambda^3(\rho - i\eta) = A\lambda^3 re^{i\delta} \tag{7.6}$$

and

$$V_{td} = A\lambda^3(1 - \rho - i\eta) = A\lambda^3(1 - re^{i\delta}) \tag{7.7}$$

with r, δ defined from

$$r = \sqrt{(\rho^2 + \eta^2)} \text{ and } \delta = cos^{-1}(\frac{\rho}{\sqrt{(\rho^2 + \eta^2)}}).$$

Using this parametrization, equation 7.5 transforms to:

$$|\frac{V_{td}}{V_{cb}}|^2 = \lambda^2 \cdot (1 + r^2 - 2rcos\delta),$$

or equivalently

$$|V_{td}| = |V_{cb}| \cdot \lambda \cdot (1 + r^2 - 2rcos\delta)^{1/2}. \tag{7.8}$$

Inserting $|V_{cb}| = 0.040 \pm 0.005$ [2], $\lambda = 0.2205 \pm 0.001$ [2], $r = \sqrt{(\rho^2 + \eta^2)} = 0.36 \pm 0.14$ from [70], the allowed region for V_{td} following from the unitarity of the CKM matrix is obtained.

$$0.004 \leq V_{td} \leq 0.015 \tag{7.9}$$

Putting this value for V_{td} in equation 7.2 one gets

$$0.0125\ GeV^2 \leq B_d \cdot f_{B_d}^2 \leq 0.175\ GeV^2. \tag{7.10}$$

A summary of the various measurements of $B^0\bar{B}^0$ mixing, obtained from machines operating at the $\Upsilon(4S)$ resonance as well as at higher energies, is presented in Figure 7.2.

At energies higher than the $\Upsilon(4S)$ mass, a mixture of B_d and B_s mesons is present with production fractions f_d and f_s respectively. The mixing probability $\bar{\chi}$

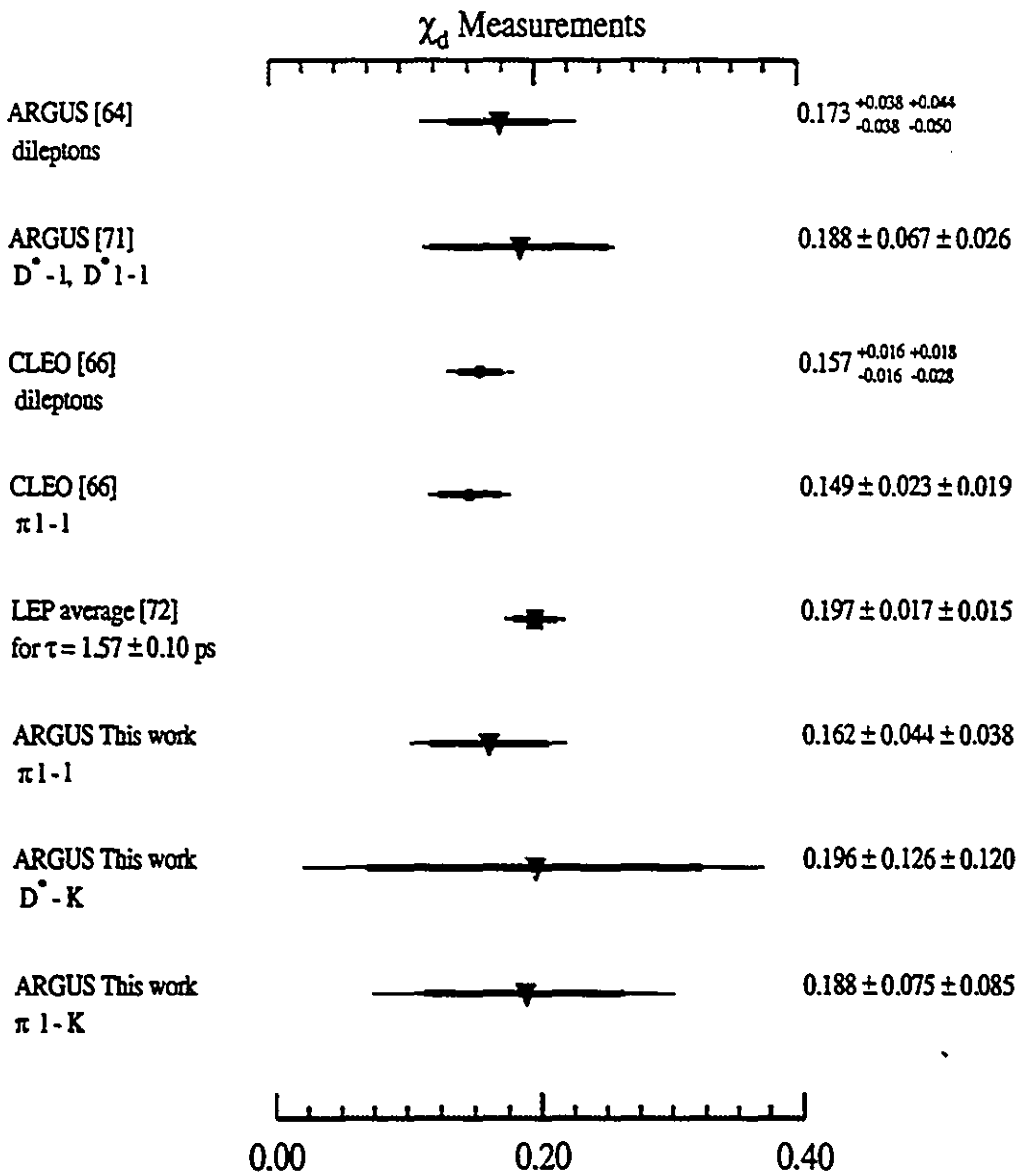

Figure 7.2: Comparison of the values obtained for χ_d. The method used for the determination of the mixing parameter is also indicated.

is in this case a combination of the mixing probabilities χ_d and χ_s for B_d^0 and B_s^0, respectively.

$$\bar{\chi} = f_d\chi_d + f_s\chi_s$$

LEP experiments provide information on χ_d by measuring the $B_d^0 \longleftrightarrow \bar{B}_d^0$ oscillation frequency Δm_d and using the B_d^0 lifetime $\tau_{B_d^0}$ to extract $x_d = \frac{\Delta m_d}{\Gamma}$.

Finally, from the study of mixing in the $B_d^0 - \bar{B}_d^0$ system, one can extract information on mixing in the $B_s^0 - \bar{B}_s^0$ system. The mixing parameter χ_d as determined in this work can be combined with the measurement of $\bar{\chi}$ to provide an estimate of the mixing in the B_s system, χ_s. For this purpose, the results of the LEP and the $p\bar{p}$ experiments will be incorporated as shown in Figure 7.3. Using for the production fractions f_d and f_s the values $f_d = 0.40$ and $f_s = 0.12$ from [72], and taking the average from the LEP and $p\bar{p}$ experiments $\bar{\chi} = 0.122 \pm 0.008$ [72], the mixing parameter χ_s is estimated to be:

$$\chi_s = 0.467 \pm 0.200, \tag{7.11}$$

which is translated to the following limit:

$$\chi_s > 0.14 \quad 90\% C.L. \tag{7.12}$$

A prediction for the mixing parameter x_s is obtained from the $B_s^0 - \bar{B}_s^0$ box diagram and is given by a formula analogous to that for $B_d^0 - \bar{B}_d^0$ mixing

$$x_s = \frac{\Delta M_s}{\Gamma} \approx \frac{G_F^2}{6\pi^2}\, m_{B_s}\, \tau_{B_s}\, (B_s f_{B_s}^2) |V_{ts}^* V_{tb}|^2\, m_t^2 F(\frac{m_t^2}{M_W^2})\, \eta_{QCD}.$$

Using the fact that $|V_{ts}| = |V_{cb}|$, as demonstrated in equation 1.8, the ratio $\frac{x_s}{x_d}$ is given by:

$$\frac{x_s}{x_d} = \frac{\eta_{B_s}\, m_{B_s}\, \tau_{B_s}(B_{B_s}\, f_{B_s}^2)}{\eta_{B_d}\, m_{B_d}\, \tau_{B_d}(B_{B_d}\, f_{B_d}^2)} \cdot |\frac{V_{ts}}{V_{td}}|^2,$$

where for the mass and lifetime of the B_s meson the values $m_{B_s} = 5368.0 \pm 3.7$ MeV and $\tau_{B_s} = 1.54^{+0.14}_{-0.13} \pm 0.05$ ps will be used [2]. The QCD correction factors η_{B_s} and

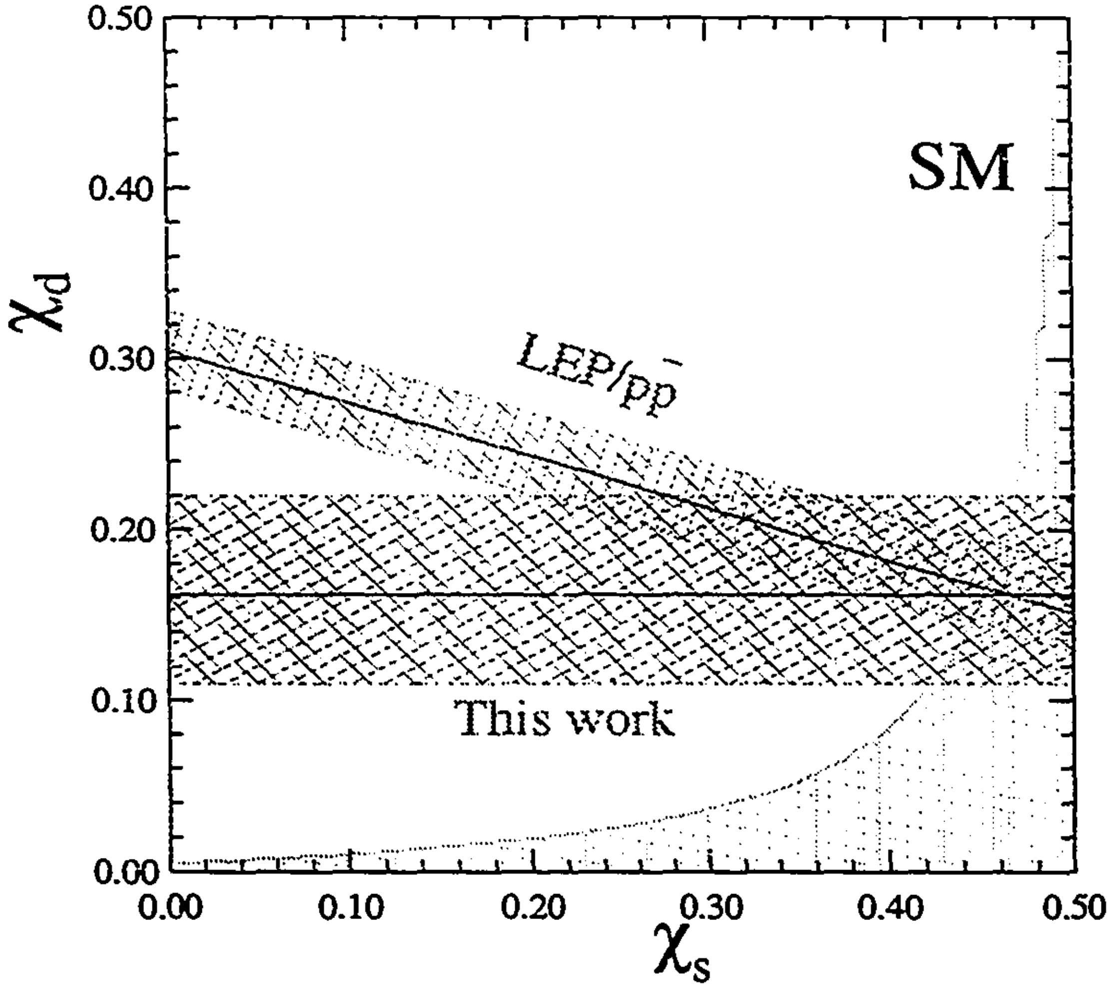

Figure 7.3: Strength of the $B_d^0\bar{B}_d^0$ versus the $B_s^0\bar{B}_s^0$ oscillation. The result obtained in this work is incorporated with the average from the LEP and $p\bar{p}$ experiments. Also, the curve obtained from the unitarity of the CKM matrix is shown (SM curve).

η_{B_d} are expected to be equal. Using for the ratio $\frac{B_{B_s} f_{B_s}^2}{B_{B_d} f_{B_d}^2}$ the value $\frac{B_{B_s} f_{B_s}^2}{B_{B_d} f_{B_d}^2} = (1.16)^2$ as taken from [70], and substituting the value found for V_{td} from equation 7.3, it follows that:

$$\frac{x_s}{x_d} \approx 26.0 \pm 17.3 \tag{7.13}$$

In the above equation only the error on the matrix element $|V_{td}|$ is considered, since this error is the dominant one. Substituting the value of x_d from equation 7.1, equation 7.13 in turn gives:

$$x_s = 18.3 \pm 13.7.$$

7.2 Kaon tagging: advantages and disadvantages

Kaons were used for tagging the flavour content of the parent B meson for the first time in the work presented in this thesis. This tagging technique was applied in the study of $B^0\bar{B}^0$ mixing. A number of advantages and disadvantages can be noted in comparison with the lepton tagging technique. The main advantage of kaon tagging is the higher statistics provided. While the rate for $b \rightarrow l \approx 10\%$, it is expected that $b \rightarrow c \rightarrow s \approx 55\%$. The main drawback is related to the fact that presently the experimental information on kaon rates is very limited. In both cases the main background source consists of wrong tags, that is cascade leptons or kaons originating from the decay of the W meson for the case of electron and kaon tagging respectively. On the other hand, the lepton spectra from B decays have been studied extensively, thus providing a relatively accurate estimate of the secondary lepton component. However, this is not true for kaons coming from B decays. The s and $\bar{s}$ production rates from b decays are poorly known, thereby adding an important systematic uncertainty to results extracted using the kaon tagging technique. However, the last drawback could be overcome in the near future, since the data collected by the CLEO Collaboration provides a large number of fully reconstructed B mesons which in turn makes possible inclusive measurements of the type $\bar{B} \rightarrow K^+X$ and

$\bar{B} \to K^- X$. The argument concerning the uncertainty of the wrong-tag fraction is also applicable to the use of the D^{*+} charge to tag the B meson flavour content, as in Chapter 5, since also in this case the background mainly arises from "wrongly" charged D^{*+} candidates.

To perform the measurements necessary to pin down the parameters of the CKM matrix, a number of experiments are in preparation. Flavour tagging will therefore be extensively used in the future. In this work, several tagging techniques are used. Kaon and D^{*+} tagging are studied and both these techniques seem promising. Since mistagging rate is an important limiting factor in future measurements, it is essential to acquire better knowledge of the rates $\bar{B} \to K^- X$, $\bar{B} \to K^+ X$, as well as $\bar{B} \to D^{*+} X$, $\bar{B} \to D^{*-} X$. Another drawback of the kaon tagging technique comes from the fact that the ratio $\frac{\text{"wrong" tags}}{\text{"right" tags}}$ is much larger for kaons than for leptons (for momentum regions where the $c \to s$ component contribution is minor). Future experiments will be able to distinguish the daughter particles of each B meson making it possible to avoid angular cuts which need to be used for the spherical distribution of $B\bar{B}$ events at the $\Upsilon(4S)$.

7.3 Summary

To summarize the results presented in this thesis, the branching ratios for the following processes were measured:

- $Br(\bar{B}^0 \to D^{*+} \ell^- \bar{\nu}) = (4.4 \pm 0.3(stat)\ \pm 0.3(syst)\ \pm 0.3(model))\%$;
- $Br(\bar{B}^0 \to D^{*+}_{(J)}\ \ell^- \bar{\nu}) = (2.5 \pm 0.6(stat)\ \pm 0.5(syst))\%$;
- $Br(\bar{B}^0 \to X\ \ell^- \bar{\nu})\ =\ (9.3 \pm 1.1(stat)\ \pm 1.5(syst))\%$;
- $Br(\bar{B} \to D^{*+}\ X) = (19.6 \pm 1.9)\%$;
- $Br(B^0 \to K^{\pm} X)\ =\ (78.2 \pm 8.2(stat))\%$.

The $B_d^0 \longleftrightarrow \bar{B}_d^0$ mixing parameter was determined using three different methods:

- using $(\pi\ell)\ \ell$ combinations the value

$$\chi_d = 0.162 \pm 0.044(stat)\ \pm 0.038(syst)$$

was obtained;

- using $D^{*+}K^{\pm}$ correlations the following value for χ_d was extracted:

$$\chi_d = 0.196 \pm 0.126(stat)\ \pm 0.120(syst);$$

- using $(\pi\ell)\ K$ combinations χ_d was found to be:

$$\chi_d = 0.188 \pm 0.075(stat)\ \pm 0.069(syst)\ \pm 0.050(Br(D^0 \to K)).$$

These last two measurements were obtained with a technique which has been used for the first time. The B meson flavour is *tagged* using the charge of the daughter kaon. Finally, from the determination of the mixing parameter χ_d, the following quantities are found:

- $x_d = 0.703 \pm 0.180$;
- $V_{td} = (0.93 \pm 0.31) \cdot 10^{-2}$,
  from unitarity of the CKM matrix one expects $0.004 \leq V_{td} \leq 0.015$;
- $0.0125\ GeV^2 \leq B_d \cdot f_{B_d}^2 \leq 0.175\ GeV^2$;
- $\chi_s = 0.467 \pm 0.200$,
  $\chi_s > 0.14 \quad 90\% C.L.$;
- $x_s = 18.3 \pm 13.7$.

Contributions to the ARGUS Experiment

During my stay in Hamburg I, like all members of the ARGUS collaboration, participated in data taking periods during which I ran shifts regularly. This requires monitoring the detector performance and the quality of the data taken.

In the beginning of my stay at DESY, I had the responsibility for the offline calibration of the ARGUS main drift chamber. In addition, I participated in the software development of the ARGUS microvertex chamber (μVDC). This large stereo angle drift chamber was designed to resolve secondary vertices from the decays of short particles and replaced the ARGUS vertex drift chamber in 1990. In particular, I was responsible for the calibration of the μVDC in order to extract the optimal resolution of the chamber. The achieved resolution is better than 40 microns.

I initially performed studies on non-$B\bar{B}$ production on the $\Upsilon(4S)$ resonance motivated by the observation of J/Ψ production above the allowed kinematical limit for J/Ψ coming from B-meson decays. These studies included the channels $\Upsilon(4S) \rightarrow J/\Psi + X$ and $\Upsilon(4S) \rightarrow h_b + \eta$, the latter being motivated by theory. My search for these type of events resulted in the best existing upper limit.

My further contributions to the physics analysis are described in this thesis. The results presented in Chapters 3,4 have been presented [79], [80] and published [81]. Finally, the analyses presented in Chapters 6,7 are currently being prepared for publication.

The ARGUS Collaboration

H. Albrecht, T. Hamacher, R. P. Hofmann, T. Kirchhoff, R. Mankel[1], A. Nau, S. Nowak[1], D. Reßing, H. Schröder, H. D. Schulz, M. Walter[1], R. Wurth
DESY, Hamburg, Germany

C. Hast, H. Kapitza, H. Kolanoski, A. Kosche, A. Lange, A. Lindner, M. Schieber, T. Siegmund, B. Spaan, H. Thurn, D. Töpfer, D. Wegener
Institut für Physik[2], Universität Dortmund, Germany

P. Eckstein, C. Frankl, J. Graf, M. Schmidtler, M. Schramm, K. R. Schubert, R. Schwierz, R. Waldi
Institut für Kern- und Teilchenphysik[3], Technische Universität Dresden, Germany

K. Reim, H. Wegener
Physikalisches Institut[4], Universität Erlangen-Nürnberg, Germany

R. Eckmann, H. Kuipers, O. Mai, R. Mundt, T. Oest, R. Reiner, W. Schmidt-Parzefall
II. Institut für Experimentalphysik, Universität Hamburg, Germany

J. Stiewe, S. Werner
Institut für Hochenergiephysik[5], Universität Heidelberg, Germany

K. Ehret, W. Hofmann, A. Hüpper, K. T. Knöpfle, J. Spengler
Max-Planck-Institut für Kernphysik, Heidelberg, Germany

P. Krieger[6], D. B. MacFarlane[7], J. D. Prentice[6], P. R. B. Saull[7], K. Tzamariudaki[7], R. G. Van de Water[6], T.-S. Yoon[6]
Institute of Particle Physics[8], Canada

[1] DESY, IfH Zeuthen

[2] Supported by the German Bundesministerium für Forschung und Technologie, under contract number 054DO51P.

[3] Supported by the German Bundesministerium für Forschung und Technologie, under contract number 056DD11P.

[4] Supported by the German Bundesministerium für Forschung und Technologie, under contract number 054ER12P.

[5] Supported by the German Bundesministerium für Forschung und Technologie, under contract number 055HD21P.

[6] University of Toronto, Toronto, Ontario, Canada.

[7] McGill University, Montreal, Quebec, Canada.

[8] Supported by the Natural Sciences and Engineering Research Council, Canada.

M. Schneider, S. Weseler
Institut für Experimentelle Kernphysik[9], *Universität Karlsruhe, Germany*

G. Kernel, P. Križan, E. Križnič, T. Podobnik, T. Živko
Institut J. Stefan and Oddelek za fiziko[10], *Univerza v Ljubljani, Ljubljana, Slovenia*

V. Balagura, S. Barsuk, I. Belyaev, R. Chistov, M. Danilov, L. Gershtein,
Yu. Gershtein, A. Golutvin, I. Korolko, G. Kostina, D. Litvintsev,
P. Pakhlov, S. Semenov, A. Snizhko, I. Tichomirov, Yu. Zaitsev
Institute of Theoretical and Experimental Physics, Moscow, Russia

[9] Supported by the German Bundesministerium für Forschung und Technologie, under contract number 055KA11P.

[10] Supported by the Ministry of Science and Technology of the Republic of Slovenia and the Internationales Büro KfA, Jülich.

Bibliography

[1] S.L.Glashow, Nucl.Phys.**22** (1961) 579;
S.Weinberg,Phys.Rev.Lett **19** (1967) 1264;
A.Salam,Proc. of the 8th Nobel Symp., Lerum, Sweden (1968).

[2] Particle Data Group:
Review of Particle Properties, Phys.Rev. **D45** (1992) 1;
Review of Particle Properties, Phys.Rev. **D50** (1994) 1. (used in Chapters 5,6,7.)

[3] L.Wolfenstein, Phys.Rev.Lett. **51** (1983) 1945.

[4] B.Weinstein,L.Wolfenstein, Rev.Mod.Phys. **65** (1993) 1113.

[5] S.W.Herb *et al.*, Phys.Rev.Lett. **39** (1977) 252.

[6] Ch.Berger *et al.* (PLUTO), Phys.Lett. **76B** (1978) 243;
C.W.Darden *et al.* (DASP II), Phys.Lett. **76B** (1978) 246;
C.W.Darden *et al.* (DASP II), Phys.Lett. **78B** (1979) 364.

[7] B.Gittelman and S.Stone, "B Meson Decays", CLNS 87/81 (1987).

[8] D.Andrews *et al.*, CLEO Collaboration, Phys.Rev.Lett. **44** (1980), 1108;
T.Böhringer *et al.*, CUSB Collaboration, Phys.Rev.Lett. **44** (1980), 1111.

[9] R.Poling *et al.* CLEO Collaboration, Proceedings of the XXIII International Conference on High Energy Physics, Berkeley (1986).

[10] J.Alexander *et al.* CLEO Collaboration, Phys.Rev.Lett. **64** (1990) 2226.

[11] H.Schröder *et al.* ARGUS Collaboration, Proceedings of the XXV International Conference on High Energy Physics, Singapore (1990).

[12] J.Alexander *et al.* CLEO Collaboration, Phys.Rev.Lett. **64** (1990) 2226.

[13] D.Perticone *et al.* CLEO Collaboration, Proceedings of the 4^{th} International Symposium on Heavy Flavour Physics, Orsay (1991).

[14] H.Albrecht *et al.* ARGUS Collaboration, Z.Phys. **C48** (1990) 543;
H.Albrecht *et al.* ARGUS Collaboration, Z.Phys. **C54** (1992) 1.

[15] C.Bebek *et al.* CLEO Collaboration, Phys.Rev. **D36** (1987) 1289;
D.Bortoletto *et al.* CLEO Collaboration, Phys.Rev. **D45** (1992) 21.

[16] G.Altarelli *et al.*, Nucl.Phys. **B187** (1981) 461.

[17] R.Ammar *et al.* CLEO Collaboration, Phys.Rev.Lett. **71** (1993) 674.

[18] G.Altarelli, N.Cabibbo, G.Corbo, L.Maiani and G.Martinelli, Nucl.Phys. **B208** (1982) 365.

[19] M.Wirbel, B.Stech and M.Bauer, Z.Phys. **C29** (1985) 637.

[20] N.Isgur, D.Scora, B.Grinstein and M.Wise, Phys.Rev. **D39** (1989) 799.

[21] R.Rückl, Habilitationsschrift, Universität München (1983), unpublished.

[22] M.Paulini(ARGUS), Ph.D. Thesis, Universität Erlangen-Nürnberg (1993).

[23] E.Leader, Lectures presented at the LAFEX International School on High Energy Physics, February 1993.

[24] H.Y.Cheng, Phys.Rev. **D26** (1982) 143.

[25] A.J.Buras, W.Slominski and H.Steger, Nucl.Phys. **B245** (1984), 369.

[26] T.Inami and C.S.Lim, Prog.Theor.Phys. **65** (1981), 297.

[27] K.Hagiwara, KEK preprint 87-47, KEK-TH-170, June 1987.

[28] H.Albrecht *et al.*, "ARGUS : A Universal Detector at DORIS II ", Nucl.Instr. and Methods **A275** (1989) 1.

[29] M.Danilov *et al.*, "The ARGUS Drift Chamber", Nucl.Instr. and Methods **217** (1983) 153.

[30] M.Danilov *et al.*, Nucl.Instr. and Methods **A274** (1989) 189.

[31] K.W.Edwards *et al.*, Nucl.Instr. and Methods **A252** (1986) 384,
J.C.Yun, M.Sc.Thesis, Carleton University, Ottawa, 1984.

[32] E.Michel *et al.*, "The ARGUS Microvertex Drift Chamber", Nucl.Instr. and Methods **A283** (1989) 544.

[33] R.Heller *et al.*, "The ARGUS Time-of-Flight System", Nucl.Instr. and Methods **A235** (1985) 26.

[34] A.Drescher *et al.*, Nucl.Instr. and Methods **205** (1983) 125;
A.Drescher *et al.*, Nucl.Instr. and Methods **216** (1983) 35;
A.Drescher *et al.*, Nucl.Instr. and Methods **A237** (1985) 464;
A.Drescher *et al.*, Nucl.Instr. and Methods **A249** (1986) 277.

[35] A.Arefiev *et al.*, DESY 83-025;
A.Arefiev *et al.*, Instr.Exp.Tech. **29** (1986) 333.

[36] H.D.Schulz and H.J.Stuckenberg, "A trigger processor for ARGUS", Proc.Topical Conference on the Application of Microprocessors in High Energy Physics Experiments, CERN, Geneva (1981) CERN 81-07.

[37] R.Waldi, "MOPEK short documentation", DESY, August 1989, Unpublished;
T.Ruf, "Description of a B-Meson decay generator program", Universität Karlsruhe, IEKP-KA/89-8 (1989).

[38] B. Andersson, G. Gustafson, G. Ingelman, T. Sjostrand, Phys. Rep. 97 (1983) 31;
T. Sjostrand, M. Bengtsson, Computer Phys. Comm. 43 (1987) 367

[39] T.Sjöstrand, LU-TP 85-10 (1985), Lund.

[40] H. Gennow, "SIMARG: A Program to simulate the ARGUS Detector", DESY F15-85-02 (1985).

[41] B.Brun, R.Hagelberg, M.Hansroul and J.C.Lassalle, "GEANT: Simulation Program for Particle Physics Experiments", CERN-DD/78/2.

[42] R.L.Ford and W.R.Nelson, "The EGS Code System", Version 3, SLAC-210, UC-32 (1978).

[43] H.Fesefeldt, RWTH Aachen Report PITHA 85-02 (1985).

[44] H.Albrecht,"ARGUS Kinematical Analysis Language (KAL)", DESY,March 1985, Unpublished.

[45] N.Isgur, D.Scora, B.Grinstein and M.B.Wise, Phys. Rev. **D39** (1989) 799.

[46] A.Nau (ARGUS), Ph.D. Thesis, Universität Hamburg (1993) DESY 93-005.

[47] J.C.Gabriel, ARGUS software note 50, Unpublished

[48] M.Wirbel, B.Stech and M.Bauer, Z.Phys. **C42** (1989) 671.

[49] J.G.Körner and G.A.Schuler, Z.Phys. **C38** (1988) 511.

[50] H.Albrecht *et al.* ARGUS Collaboration, Phys.Lett. **B197** (1987) 218.

[51] A.Nippe (ARGUS), Ph.D. Thesis, Universität Hamburg (1990) DESY F15-90-05;
H.Albrecht *et al.* ARGUS Collaboration, Phys.Lett. **B255** (1991) 634.

[52] H.Albrecht *et al.* ARGUS Collaboration, Z.Physik **C54** (1992) 1.

[53] D.Bortoletto *et al.* CLEO Collaboration, Phys.Rev.Lett. **64** (1990) 2117.

[54] D.Acosta *et al.* CLEO Collaboration, CLNS-93-1238 August 1993. 31pp.

[55] F.Butler *et al.* CLEO Collaboration, Phys.Rev.Lett. **69** (1992) 2041.

[56] H.Albrecht *et al.* ARGUS Collaboration, Z.Physik **C52** (1991) 353.

[57] D.Bortoletto *et al.* CLEO Collaboration, Phys.Rev. **D45** (1992) 21.

[58] H.Albrecht *et al.*, ARGUS Collaboration, preprint DESY 92-146 (1992); K.Reim (ARGUS), Ph.D. Thesis, Universität Erlangen-Nürnberg (in preparation).

[59] H.Albrecht *et al.*, ARGUS Collaboration, Phys.Lett. **B197** (1987) 452.

[60] R.Fulton *et al.* CLEO Collaboration, Phys.Rev. **D43** (1991) 651.

[61] H.Albrecht *et al.*, ARGUS Collaboration, Phys.Lett. **B246** (1990) 278.

[62] J.G.Körner and G.A.Schuler, Z.Phys. **C46** (1990) 93.

[63] H.Albrecht *et al.*, ARGUS Collaboration, Phys.Lett. **B192** (1987) 245.

[64] H.Albrecht *et al.*, ARGUS Collaboration, Z.Phys. **C55** (1992) 357.

[65] M.Artuso *et al.* CLEO Collaboration, Phys.Rev.Lett. **62** (1989) 2233.

[66] J.Bartelt *et al.* CLEO Collaboration, Phys.Rev.Lett. **71** (1993) 1680.

[67] H.Albrecht *et al.*, ARGUS Collaboration, Phys.Lett. **B249** (1990) 359.

[68] S.Henderson *et al.* CLEO Collaboration, Phys.Rev. **D45** (1992) 2212.

[69] D.Coffman *et al.*, MARK III Collaboration, Phys.Lett. **B263** (1991) 135.

[70] A.Ali and D.London, CERN-TH 7398/94, August 1994.

[71] M.Schäfer, (ARGUS), Ph.D. Thesis, Universität Hamburg (1991) DESY F15-91-02.

[72] R.Forty, ALEPH Collaboration, Presented at the $27th$ International Conference on High Energy Physics, Glasgow, July 1994.

[73] H.Albrecht *et al.*, ARGUS Collaboration, Z.Phys. **C58** (1993) 191.

[74] S.L.Glashow, J.Iliopoulos and L.Maiani, Phys.Rev.**D 2** (1970) 1285.

[75] T.Oest, (ARGUS), Ph.D. Thesis, Universität Hamburg (1993) DESY F15-93-01.

[76] F.Abe *et al.*, CDF Collaboration, Phys.Rev. **D50** (1994) 2966.

[77] L.Lyons, D. Gibaut and P.Clifford, Nucl.Instr. and Methods **A270** (1988) 110.

[78] A.J.Buras, M.Jamin and P.H.Weisz, Nucl.Phys. **B347** (1990) 491.

[79] H.Kapitza, (ARGUS), Proceedings of the International Europhysics Conference on High Energy Physics, Marseille, France, 1993.

[80] M.Danilov, Summary talk, presented at the 1993 European Physical Society Conference, Marseille, France, 1993.

[81] H.Albrecht *et al.*, ARGUS Collaboration, Phys.Lett. **B324** (1994) 249.

[82] The LEP Collaborations, CERN 94-187.